Order Number 9304752

Nonresonant photon dressing in spin one quadrupolar systems

Zhuang, Yi-Li, Ph.D.

City University of New York, 1992

U·M·I

300 N. Zeeb Rd.
Ann Arbor, MI 48106

NONRESONANT PHOTON DRESSING IN SPIN ONE QUADRUPOLAR SYSTEMS

by

Yi-Li Zhuang

A dissertation submitted to the Graduate Faculty in Physics in partial fulfillment of the requirements for the degree of Doctor of Philosophy, The City University of New York.

1992

This manuscript has been read and accepted for the Graduate Faculty in Physics in satisfaction of the dissertation requirement for the degree of Doctor of Philosophy.

17 July 1992 — Date
Chair of Examining Committee: Professor Robert A. Marino

20 July 1992 — Date
Executive Officer: Professor Joseph Krieger

Professor Ying Chen

Professor Steve G. Greenbaum

Doctor Frank Owens

Professor Fredrick W. Smith

Supervisory Committee

The City University of New York

ABSTRACT

NONRESONANT PHOTON DRESSING IN SPIN ONE QUADRUPOLAR SYSTEMS

by

Yi-Li Zhuang

Advisor: **Professor Robert A. Marino**

The main part of this thesis is a study of the effects of nonresonant photon dressing on spin 1 pure quadrupolar system with symmetric EFG. Energy levels of spin 1 nuclei dressed by linearly or circularly polarized photons were theoretically derived and numerically analyzed. In both cases, the degeneracy of m_ζ equals ± 1 states is not lifted, so only one line can be excited and it is shifted up in frequency. The energy levels are found to depend on the angle θ between the principal EFG ζ axis and the dressing field. Since most NQR samples are polycrystalline, a general formula for powder patterns due to photon dressing was derived and numerical examples were plotted for the case of linearly polarized photons, spin 1 and $\frac{3}{2}$, and circularly polarized photons, spin 1. In all of these cases, NQR lines are broadened, and have a peak located at $\theta = 90^o$.

Energy levels of photon dressed protons in zero static field are analyzed for the purpose of discussing ^{14}N spin-echo time. Protons are shown to reorient between $\pm\frac{1}{2}$ states rapidly , so that their local field tends to average out.

Powdered crystalline samples Trimethylamine (TMA), Triethylenediamine (TED), and Hexanethylenetetramine (HMT) all with symmetric EFG were experimentally investigated by ^{14}N NQR. For circularly polarized dressing of 25 G peak, no NQR frequency shift was observed; a monotonic line narrowing was observed in TMA and TED,

but not HMT; fine structure details of TED and HMT were revealed as a result of the line narrowing, but the cause of the fine structure was not determined. Experimental results are in good agreement with theory.

A minor portion of this thesis is to study the effects of annealing and hydrogenation on short-range order in amorphous III-V compounds through NMR linewidth. $\alpha - GaP$, $\alpha - GaAs$, and $\alpha - GaAs : H$ grown on single crystal alkali halide substrates by rf-sputtering have been studied. The results were compared with that of previous measurements on $\alpha - GaP$ and $\alpha - GaAS$ grown on different substrates at different temperature. The study showed that sample microstructure is directly influenced by sample preparation conditions, however, the presence of 10% hydrogen in the sample did not influence the NMR linewidth at room temperature nor the annealing behaviour.

Acknowledgements

I would like to express my deep and special appreciation to Professor Robert A. Marino, not only for the broad background and excellent guidance he has given me as my thesis advisor, but also for his friendship and understanding. His encouragement has been an important factor in the completion of this thesis. Professor Steve Greenbaum is greatly acknowledged for providing me the opportunity to access NMR instrumentation and for many valuable discussions.

Mr. Richard Krumm reserves my gratitude for his help in building the field dressing apparatus.

Professor Mark Hillery is specially thanked for examining the derivation of the theoretical part of this thesis.

I would like to thank the thesis committee members, Professor Ying-Chih Chen, Doctor Frank Owens, and Professor Fredrick W. Smith for their friendly participation and reading of this manuscript.

I would also like to thank Dr. Yiusun Pak for his help in NMR techniques and various other aspects, and Dr. Shizhe Li for help in sample-coil making. I am very grateful to Mr. Jayakody for his friendship and help in last two years of my study.

Last but no least, my husband, Dr. Zhen-Guo Zhu, has provided a great deal of help and encouragement. I also thank him for typing this manuscript.

This work was financially supported by PSC-CUNY Research Award Program.

Dedication

I would like to dedicate this thesis to my parents. They hardly bear to be separated from me to support my study.

Table of Contents

List of Tables

List of Figures

Chapter 1

Introduction

The main object of this thesis is to study the effects of nonresonant photon dressing on spin $I = 1$ pure quadrupolar system. C. Cohen-Tannondji and S. Haroche [1, 2, 3, 4] introduced a novel concept of <<dressed>> atoms which studies the physical properties of atoms interacting with a nonresonant radiofrequency magnetic field. This fully quantum-mechanical interpretation describes the rf (radiofrequency) field as photons and treats the "atom plus the rf field and their interaction" as a whole system, and call this system, by analogy with quantum electrodynamics vocabulary, the atom <<dressed>> by radiofrequency photons. The dressed atom theory explains very well previously discovered phenomena such as multiple quantum transitions [5, 6, 7, 8], Haroche's resonances [9], resonance of Geneux, Alexandrov, Polonsky [10, 11, 12], Autler-Townes effect [13], and so on. The classical theory which describes the rf field in a classical way actually also explains these phenomena, but the dressed atom point of view gives a simpler and more obvious physical interpretation starting from the energy level diagrams and allows one to understand and determine the main features of all magnetic resonant lines in terms of elementary processes involving rf photons absorption or emission. The dressed atom theory also predicts and calculates some new physical effects such as the atomic Landé g-factor being modified by the zero*th* order Bessel function when the atom is coupled with a linearly polarized rf field perpendicular to the static field, or as the Zeeman degeneracy of anatomic level in a zero static field being removed when coupled to a rotating rf field. The modification of the Landé factor is the root of many interesting effects of rf photon dressing, such as modification of the Zeeman effect, like Zeeman hyperfine spectra, NMR lines, etc.;

modification of magnetic depolarization curves, the well known Hanle effect [14]; and modification of magnetic relaxation of dressed atoms which could possibly change the resonant lineshape and linewidth appreciably.

The modification of Landé g-factor was demonstrated on optically pumped ^{199}Hg vapor through the observation of change in the width of the Hanle signal [15, 3]. Essentially the same theoretical result of Landé factor modification was derived semiclassically by Pegg and Series [16], classically and quantum mechanically by Yabuzaki et. al [17], and demonstrated by Tsukada et. al. [18] with a strong rf field.

Yabuzaki et al. [19] examined the effects of photon dressing by nonresonant oscillating field with arbitrary strength and direction. Dourneuf et al. [20] extended the treatment in Ref. 2 for a circularly polarized photon and demonstrated that the rotating field is equivalent to a fictitious static magnetic field along the rotating axis. The experiments concerning the effect of photon dressing were performed mostly on optically pumped vapors [21, 22, 23, 24]. The experiments in liquids and solid were also performed in conjunction with magnetic resonances. The modification of Zeeman energies of nuclei due to nonresonant oscillating field and related effects were investigated on NMR in the rotating reference frame to achieve the specific condition required for Landé factor modification [25, 26, 27].

Ito and Hashi reported [28] the first experimental observation of photon-dressed NQR effects in 1978, and in subsequent work [29, 30, 31]. They observed a shift and a splitting of the ^{23}Na NQR line in sodium chlorate and an increase in the ^{35}Cl spin echo time in sodium chlorate and in p-dichlorobenzene. They also worked out the theory for a dressed quadrupolar system with spin $I = \frac{3}{2}$.

Based on the above introduction of the literature of photon dressing, the object of this thesis was raised. A theory for spin $I = 1$ quadrupolar system with symmetric EFG interacting with nonresonant oscillating or rotating field is given. Since most NQR samples are in the powdered crystal form, energy diagrams are given for various relative orientations between the principal EFG axes and the rf field. A theoretical study of

NQR powder patterns due to photon dressing is also done. Energy levels of photon dressed protons ($I = \frac{1}{2}$) in zero static field are analyzed for the purpose of discussing ^{14}N spin-echo time. Some experimental data are taken on ^{14}N compounds with axial symmetry EFG in the presence of circularly polarized dressing field. Experimental results are in good agreement with theory.

A minor portion of this thesis is devoted to the study of effects of annealing and hydrogenation on short-range order in amorphous III-V compounds by nuclear magnetic resonance methods. Amorphous samples of $\alpha - GaP$, $\alpha - GaAs$, and $\alpha - GaAs : H$ grown on single crystal alkali halide substrates by rf-sputtering have been studied. The NMR lines measured through spin-echo method showed to be 2nd order quadrupole broadened. The effects of annealing are learned through the change of linewidths and the results were compared with that of previous measurements on $\alpha - GaAs$ grown on different substrates at different temperature. The study showed that sample microstructure is directly influenced by sample preparation techniques and conditions, however, the presence of 10% hydrogen in the sample did not influence the microstructure at room temperature nor the annealing behaviour in our experiment.

The Structure of this thesis is as follows. Chapter Two is background theory of NMR and NQR. Chapter Three describes the dressed atom theory for the magnetic resonance case. The theory of dressed quadrupolar system with spin $I = 1$ and its NQR powder pattern are given in Chapter Four and Five. Chapter Six discusses the energy diagram of a dressed proton for the purpose of studying ^{14}N spin-echo time. The experimental study of photon dressed NQR is in Chapter Seven and the $III - V$ amorphous semiconductor work is located in the last chapter.

Chapter 2

NMR and NQR Interaction and Spectroscopy

2.1 NMR Phenomenon

A magnetic system with total angular momentum, $\vec{J}$, has a magnetic moment, $\vec{\mu}$, colinear with $\vec{J}$ given by,

$$\vec{\mu} = \gamma \vec{J} = \gamma \hbar \vec{I} \tag{2.1}$$

where γ is the gyromagnetic ration, $\hbar$ is Plank's constant, h, divided by 2π, and $\vec{J} = \hbar \vec{I}$, with $\vec{I}$ the angular momentum operator. For atomic nuclei, I is just the nuclear spin.

The eigenvalues of any component of $\vec{I}$, for example, I_z, form a set of discrete values, described by a magnetic quantum number m. m can take $2I + 1$ values, ranging from $-I$ to $+I$ in integer steps.

With the application of a static magnetic field $\vec{H}_o$ to a nuclear spin system, the interaction hamiltonian of the nuclear magnetic moment with the external field is,

$$\mathcal{H} = -\vec{\mu} \bullet \vec{H}_o \tag{2.2}$$

If the field $\vec{H}_o$ is uniform and taken to be applied along the z axis then the resulting energy eigenvalues are

$$E = -\mu_z H_o = -\gamma \hbar \vec{H}_o m, \tag{2.3}$$

with m the magnetic quantum number. The application of magnetic field $\vec{H}_o$ splits the nuclear energy level into $2I + 1$ sublevels, this effect is called the Zeeman effect. The separation between adjacent Zeeman levels is

$$\Delta E = \gamma \hbar H_o = \hbar \omega_o \tag{2.4}$$

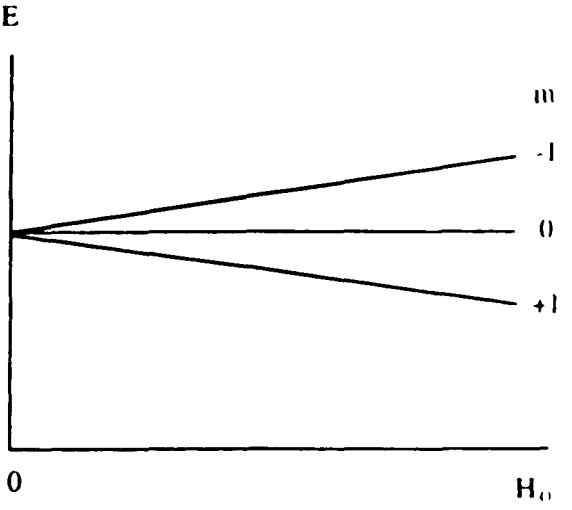

Figure 2.1: Zeeman energy levels for spin 1 nucleus and γ is positive.

where $\omega_o = \gamma H_o$ is called the Larmor frequency. The Zeeman energy levels for a spin $I = 1$ nuclei are displayed in Fig. 2.1 for the case where γ is positive.

If the nuclear spins are in equilibrium then the population of each energy level will be proportional to the Boltzman factor, $e^{-E/kT}$, where k is Boltzman's constant and T is the temperature of the spin system. Note that at $T = 0$, all of the spins will be in the lowest energy and at $T = \infty$ all of the energy levels will be equally populated. If an oscillating magnetic field $\vec{H}_1$ (in the radio frequency range) is applied perpendicular to $\vec{H}_o$ and if the angular frequency ω satisfies the Bohr resonance condition,

$$\hbar\omega = \Delta E \tag{2.5}$$

by interaction of the magnetic moment with the rf field, using time dependent perturbation, it is possible to induce transitions between the adjacent energy levels. $\vec{H}_1$ is customarily called the probing field which is used to explore the energy levels of the system. Note that the Zeeman energy levels are $2I + 1$ fold nondegenerate, but the transition frequencies between different levels are uniform. The above described phenomenon is called nuclear magnetic resonance, NMR.

The effect of the applied radiation will be to equalize the spin population, thus raising the spin temperature. This results from a net absorption of energy and the spins jump from low energy levels to higher levels. NMR is detected by either observing this energy absorption or by observing the spin system as it evolves after the applied radiation stops and the spins begin their return to their equilibrium temperature. Continuous Wave spectrometers detect the NMR by the former method, while Pulsed spectrometers detect it by the latter.

2.2 Pulsed NMR Spectrometer

2.2.1 Signal Detection

Now, let's discuss in a little more detail the detection of NMR by pulsed techniques.

The total or macroscopic magnetization of the sample is the sum of all individual magnetizations, $\vec{\mu}_k$,

$$\vec{M} = \sum_k \vec{\mu}_k \tag{2.6}$$

In the presence of static magnetic field $\vec{H}_o$, the net macroscopic magnetization $\vec{M}_o$ is parallel to $\vec{H}_o$ given by,

$$\vec{M}_o = \chi_o \vec{H}_o \tag{2.7}$$

where χ_o is the static magnetic susceptibility. The equation of motion of $\vec{M}$ in the applied field $\vec{H}_o$ is

$$\frac{d\vec{M}}{dt} = \vec{M} \times \gamma \vec{H}_o \tag{2.8}$$

which tells us that $\vec{M}$ will precess about the applied field $\vec{H}_o$ with an angular velocity $\vec{\Omega} = -\gamma \vec{H}_o$. If originally $\vec{M}$ and $\vec{H}_o$ make an angle θ, then $\vec{M}$ precesses about $\vec{H}_o$ will generate a cone about $\vec{H}_o$ with angle θ. In experiments, we place the sample inside a coil, which has inductance L, with its axis along the x axis. The probing field $\vec{H}_1$ is created by applying an AC voltage to the coil. This AC current creates an oscillating magnetic field $H_{x_0} \cos \omega t$ inside the coil. The total field applied to the sample is then,

$$H_T = H_o \hat{z} + H_{x_o} \cos \omega t \hat{x}. \tag{2.9}$$

Where $\hat{x}$, $\hat{y}$, and $\hat{z}$ are the unit vectors of the xyz laboratory coordinate system. Resolving $H_x(t)$ into two components counterrotating about the z axis, we obtain

$$\begin{aligned} H_x(t)\hat{x} &= \vec{H}_+ + \vec{H}_-, \\ \vec{H}_\pm &= H_1(\cos\omega t\hat{x} \pm \sin\omega t\hat{y}), \end{aligned} \tag{2.10}$$

where $2H_1 = H_{x_o}$. $\vec{H}_\pm$ rotate either in the same sense or the opposite sense as the precession of $\vec{M}$. It can be shown that, for near resonance, only the one rotating in the same sense as $\vec{M}$ has significant effect [32]. So we must take $\vec{H}_-$ as $\vec{H}_1$ which rotate around z axis with angular frequency $\vec{\omega} = -\omega\vec{k}$. Then,

$$\frac{d\vec{M}}{dt} = \vec{M} \times \gamma \left[\vec{H}_o + \vec{H}_1(t)\right], \tag{2.11}$$

Now, introduce a frame of reference $\hat{x}'\hat{y}'\hat{z}'$, rotating at frequency $\vec{\omega}$, the same as $H_1(t)$ about the z axis, and take the z' axis to coincide with z. In the rotating frame, $\vec{H}_1$ is static along the $\hat{x}'$ axis, then the equation of motion for $\vec{M}$ in the rotating frame is [33],

$$\begin{aligned} \frac{\partial\vec{M}}{\partial t} &= \vec{M} \times \gamma \left[(H_o - \frac{\omega}{\gamma})\hat{z}' + H_1\hat{x}'\right] \\ &= \vec{M} \times \gamma\vec{H}_{eff}, \end{aligned} \tag{2.12}$$

where

$$\vec{H}_{eff} = (H_0 - \frac{\omega}{\gamma})\hat{z}' + H_1\hat{x}', \tag{2.13}$$

and $\frac{\partial\vec{M}}{\partial t}$ represents the derivative in the rotating frame. We can see that $\vec{M}$ will precess about $\vec{H}_{eff}$ as depicted in Fig. 2.2. At the resonance condition, i.e. when $\omega = \omega_o = \gamma H_o$, the above equation become $\vec{H}_{eff} = H_1\hat{x}'$, and $\vec{M}$ will precess about x' axis with frequency γH_1. If the rf field H_1 is turned on only for a time interval t_P, this precession at frequency γH_1 will result in a rotation of $\vec{M}$ away from the z direction by $\gamma H_1 t_P$ radians. This expression is called the "flip angle" of the rf pulse. When the pulse width is adjusted so that $\gamma H_1 t_P = \pi/2$, we have a so called $\pi/2$ pulse. Then, $\vec{M}$ at equilibrium along z axis will rotate $\pi/2$ degree and align up along the $\hat{y}'$ axis. At the

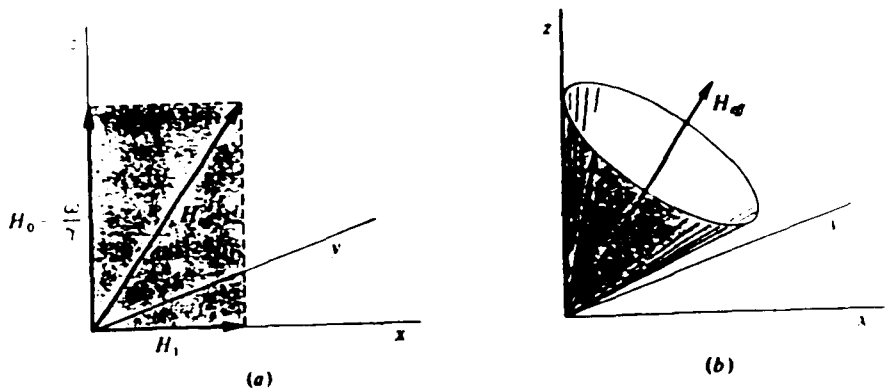

Figure 2.2: Magnetization $\vec{M}$ precess about $\vec{H}_{eff}$. (a) Effective field. (b) Motion of magnetization $\vec{M}$ in the rotating coordinate system.

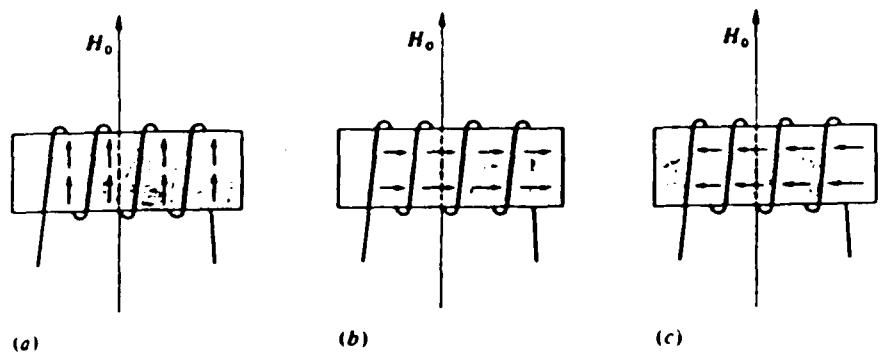

Figure 2.3: Detection of Pulsed NMR. (a) Coil containing sample. In thermal equilibrium an excess moments is parallel to H_0. (b) and (c) Following a $\frac{\pi}{2}$ pulse, the excess moments precess perpendicular to H_o and generate a rf voltage in the coil.

time the pulse is turned off, $\vec{M}$ along the $\hat{y}'$ axis will precess about $\hat{z}$ axis at the Larmor frequency ω_o and thus induce a voltage in the coil. The NMR signal is thus detected. This situation is sketched in Fig. 2.3.

Since each nucleus has a unique value of γ, it is possible to observe NMR for only one particular nucleus within a multi nuclear sample. Also it can be seen from Eq. 2.4 that the energy difference ΔE is proportional to the applied field H_o. Since the signals detected are typically in the range of a microvolt or less it is desirable to use as high a field as possible in order for the signal to be detected over the natural thermal noise

which is also detected along with the NMR signal.

2.2.2 Free Induction Decay and It's Fourier Transformation

Since after the $\frac{\pi}{2}$ pulse the magnetization $\vec{M}$ is precessing in the $x' - y'$ plane freely without the radiation $\vec{H}_1$ and it will decay in time, the above described signal is called a free induction decay (FID). The decay of magnetization in $x' - y'$ plane is due to two mechanisms. The distribution of resonant frequencies of individual spins causes some spins to precess faster than the others so that $\vec{M}$ will precess out of phase. On the other hand, $\vec{M}$ also tends to regrow along the $z' = z$ direction because thermal equilibrium is being re-established. The distribution of resonant frequencies is due to field inhomogeneity and interactions of the spin with its surroundings. These will be discussed in section 2.3. The time domain signal FID includes all of the information of the spin system, it's mathematical Fourier transformation (FT) is the resonant line shape in the frequency domain. If FID envelope is decaying exponentially at the rate $\exp(-t/T_2^*)$, where T_2^* is the decay constant, then its FT is a single Lorentsian line with a full width at half maximum (FWHM) of $2/T_2^*$. If one performs NMR by CW methods, the absorption mode signal one gets in the absence of modulation effects is just the frequency domain lineshape, and its FT gives the time domain FID. CW and pulsed NMR are connected by FT.

By absorbing energy from the rf field, the spin system establishes transverse magnetization $M_x(t)$ and generates an NMR signal. The response of M_x to the rf field $\vec{H}_x(t)$ is [33],

$$M_x(t) = [\chi'(\omega)\cos\omega t + \chi''(\omega)\sin\omega t]H_{x_o} \tag{2.14}$$

where $\chi'(\omega)$ and $\chi''(\omega)$ are defined as the real and imaginary parts of the complex magnetic susceptibility,

$$\chi(\omega) = \chi'(\omega) - i\chi''(\omega) \tag{2.15}$$

and $\chi'(\omega)H_{x_o}$ and $\chi''(\omega)H_{x_o}$ are just the components of $M_{x'}$ and $M_{y'}$ in the rotating frame. Only when the frequency of $\vec{H}_1$ matches the resonance condition will $\chi(\omega)$ have

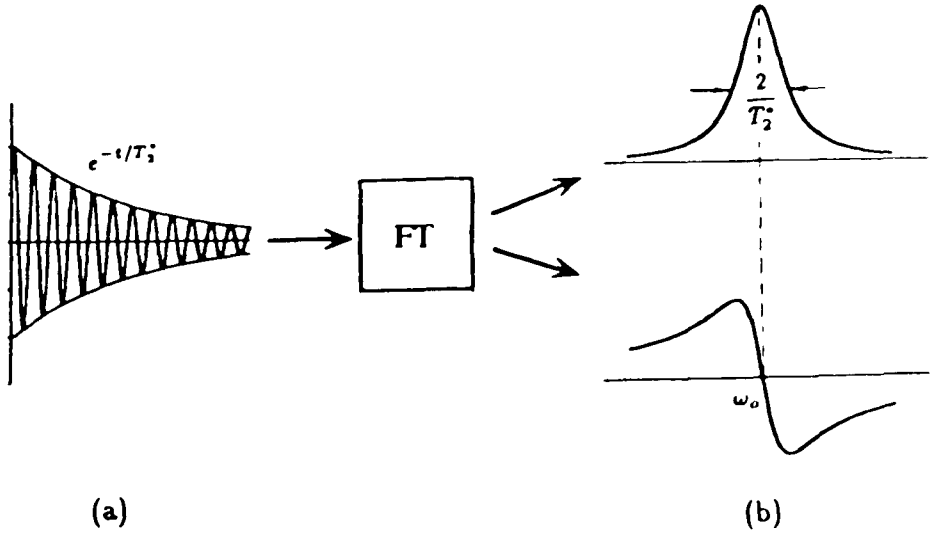

Figure 2.4: Relation between FID and the spectrum. (a) Time domain FID obtained from pulsed NMR. By Fourier transforming FID, (b) Frequency domain lineshape which can be obtained through CW NMR. The top trace is the absorption mode spectrum and the bottom is dispersion.

a significant magnitude, $\chi''(\omega)$ is proportional to the absorption signal, and $\chi'(\omega)$ is proportional to the dispersion signal.

Because both absorption and dispersion signals contain informations of the spin system, it is desirable to collect both of them. In phase sensitive quadrature detection, these two signals are collected simultaneously by comparing the detected signal to two reference frequencies exactly 90° out of phase with each other. Consider these two signals as real and imaginary parts of a complex FID, the Fourier transform of the complex FID yields both the absorption and dispersion signals as its real and imaginary parts one can get in CW NMR. The relation between the FID and its spectrum is shown in Fig. 2.4.

The advantages of quadrature detection (QD) is described in detail by Fukushima and Roeder [34]. Part of the III-V semiconductor NMR study used QDFT while part of the NQR study used single channel FT in this thesis.

2.2.3 Spin Echoes

Any pulse spectrometer has a "dead time" which is the time interval immediately after a pulse during which the signal can not be detected. Dead times of about 10 μsec are the best that can be done with today's technology at frequencies of interest to this thesis, 2-3 MHz. To acquire full information from FID, it is very important for the NMR spectrometer to recover from the pulse as quickly as possible so that none of the signal will be lost. For broad line, the FID decay constant T_2^* is small and FIDs decay fast: the dead time problem could prevent detection of the FID signal.

The spin-echo method is a useful way to overcome this dead time problem. The formation of an echo is sketched in Fig. 2.5 in the rotating frame. A 90° pulse applied along the x' axis rotates $\vec{M}$ from its equilibrium z axis to the y' axis. Then, after a time τ, a 180° pulse is applied along y' axis. The effect of the 180° pulse is to flip all of the spins 180° but the direction of their precession in the $x' - y'$ plane remain the same. Thus at time 2τ, the dephasing of the spins will be recovered and the spins will refocus along y' axis, and an echo, which consists of two FIDs back to back, is formed with its center located at 2τ. This pulse sequence can be expressed as $90^\circ_{x'} - \tau - 180^\circ_{y'}$ to indicate the pulse durations and directions. It must be mentioned here that the echo method can only refocus the dephasing caused by inhomogeneous mechanisms where the spin precession with respect to the Larmor precess is not flipped with the spin, while for homogeneous mechanism such as spin-spin interaction, the precession direction is flipped together with the spin, so that its dephasing can not be recovered. So, to observe an echo with maximum intensity, the spin system must possess a large amount of inhomogeneous broadening and the thermal process that results in spins realigning in the z direction must not be too important. For a broad line, one can trigger the receiver at time 2τ, so that a complete FID will be recorded without losing any information due to the dead time problem. This is just the method used in the III-V semiconductor NMR study of this thesis.

By using certain pulse sequences one can obtain a continuous set of spin echoes,

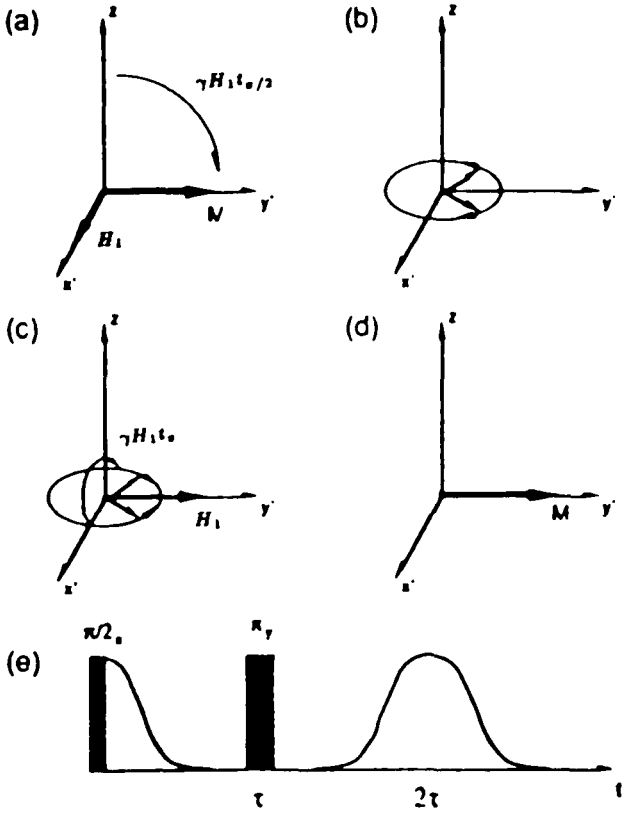

Figure 2.5: The formation of a spin echo in rotating frame. (a) At $t = 0$, a $\frac{\pi}{2}$ pulse along x' axis causing $\vec{M}$ to rotate away from z axis to align along y' axis. (b) After the pulse, the spins precess around z axis. Some spins precess faster and some slower than the rotating y' axis at Larmor frequency ω_o, causing the constituents of $\vec{M}$ to dephase. (c) At time τ, a π pulse causes all spins to flip by 180° around y' axis. Now the faster spins are behind and the slower ones are ahead of the y' axis. (d) At time 2τ, $\vec{M}$ is restored along y' axis. (e) The spin echo pulse sequence and detected signal.

an echo train. The echo amplitude envelope decay constant T_2 is determined by the homogeneous spin-spin interaction. The first pulse sequence for echo train was invented by Carr and Purcell [35] and can be expressed as $90^\circ_x - [\tau - 180^\circ_x - \tau]_n$, where n is integer, and the echoes are formed at $(2n + 2)\tau$.

2.2.4 Frequency Spectrum of the RF Pulse

Although the rf pulse is oscillating at a single frequency ν_t generated by the transmitter, its frequency spectrum is not monochromatic, because many different frequencies have to be combined in order to form the rising and falling edges of the rectangular pulse. The frequency spectrum of the pulse is the distribution of frequencies that can be excited by the pulse. The Fourier transform of a rectangular pulse with duration t_P is a *sinc* function,

$$sinc(xt_P) = \frac{\sin \pi x t_P}{\pi x t_P} \tag{2.16}$$

centered at frequency ν_t, where $x = \nu - \nu_t$ is the frequency difference with respect to the transmitter. The *sinc* function is sketched in Fig. 2.6; the first nodes are located at $\pm 1/t_P$. As a rule of thumb, to irradiate uniformly an NMR line of width $\Delta\nu$, the pulse duration t_P should be approximately equal to $\frac{2}{3\Delta\nu}$. For broad lines, t_P is required to be very small. However, to create a desired flip angle $\gamma H_1 t_P$, a very small t_P requires a very high rf power level, which may not always be available. As an alternative, one could irradiate a broad line part by part, and this is what was done in the III-V semiconductor study.

2.3 Interactions and Relaxations

2.3.1 Interactions in NMR

Besides the Zeeman interaction described in section 2.1, there are other ways in which the nuclear spin interacts with its environment. These interactions include the nuclear

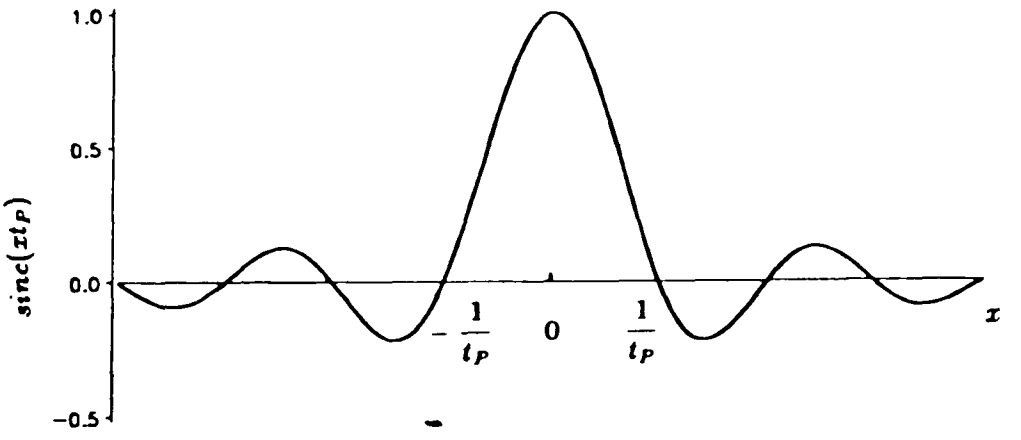

Figure 2.6: The spectrum of a rectangular pulse of width t_P.

electrical quadrupole interaction, which will be discussed in section 2.5; the dipole-dipole interaction between nuclear spins; the interaction of nuclear spins with the orbital electrons, the so called chemical shift; the indirect spin-spin J interaction; and the interaction caused by molecular motion. The last three interactions are not pronounced in solids NMR, expect possibly though their effect on relaxation times, and the dipole-dipole interaction is going to be discussed below.

Consider two spins, I and S. Let $\vec{r}_{IS}$ be the vector from spin I to S. The magnetic field $\vec{H}_{loc}$ at spin S due to I is then,

$$\vec{H}_{loc} = \frac{3(\vec{\mu}_I \bullet \vec{r}_{IS})\vec{r}_{IS}}{r_{IS}^5} - \frac{\vec{\mu}_I}{r_{IS}^3}, \tag{2.17}$$

the hamiltonian of S in the field of $\vec{H}_{loc}$ is,

$$\begin{aligned} \mathcal{H}_d &= -\vec{\mu}_S \bullet \vec{H}_{loc} \\ &= \frac{\vec{\mu}_S \bullet \vec{\mu}_I}{r_{IS}^3} - \frac{3(\vec{\mu}_I \bullet \vec{r}_{IS})(\vec{\mu}_S \bullet \vec{r}_{IS})}{r_{IS}^5}, \end{aligned} \tag{2.18}$$

where $\vec{\mu}_I$ and $\vec{\mu}_S$ are magnetic moments defined by Eq. 2.1. Since nuclear magnetic moments are of the order of 10^{-3} Bohr magnetons and the internuclear distance is of the order of Angströms, H_{loc} in a rigid lattice is in general of the order of a few gauss.

Compared to the static magnetic field H_o usually of the order of a few Tesla, the dipole-dipole interaction $\mathcal{H}_d$ is only a small perturbation. H_{loc} may either aid or oppose to the static field H_o, thus a spread in the resonance condition results. For distinctly close neighbours with a large gyromagnetic ratio γ, $\mathcal{H}_d$ is bigger and may cause splittings of NMR lines, while the contribution of $\mathcal{H}_d$ from the other neighbours is even smaller and results in a uniform broadening of the resonance lineshape. These are discussed in detail by Abragam [32].

2.3.2 Relaxation

As outlined in the brief description of the NMR phenomenon in section 2.1, the nuclear spins absorb energy from the rf field and jump from low energy levels to higher levels thus raising the spin temperature. After the rf pulse stops the spin system dissipates this energy through various kinds of mechanisms and tends to restore its equilibrium spin temperature. This process is called relaxation. Fig. 2.7 vividly depicts the pulsed NMR and relaxation process in the rotating reference frame [36].

The reestablishment of magnetization M_z along the z direction is through thermal processes which transfer "heat" back to the lattice bath. The rate of this energy transfer is measured by the spin-lattice relaxation time T_1. Usually the growth of M_z can be described by an exponential function,

$$M_z(t) = M_o \left[1 - e^{-t/T_1}\right]. \tag{2.19}$$

where M_o is the equilibrium net magnetization. T_1 is always greater than or equal to the spin-spin relaxation time T_2; in solids, usually, $T_1 \gg T_2$.

The dephasing of magnetization in the $x' - y'$ plane is often classified as either homogeneous or inhomogeneous. The inhomogeneous broadening mechanism in NMR is mainly due to the inhomogeneity of the static field H_o, while the homogeneous mechanism is mainly dipolar. The spin-spin relaxation time, or the spin-echo decay time T_2, is contributed only by the homogeneous mechanism. Thus, the FID decay constant T_2^*,

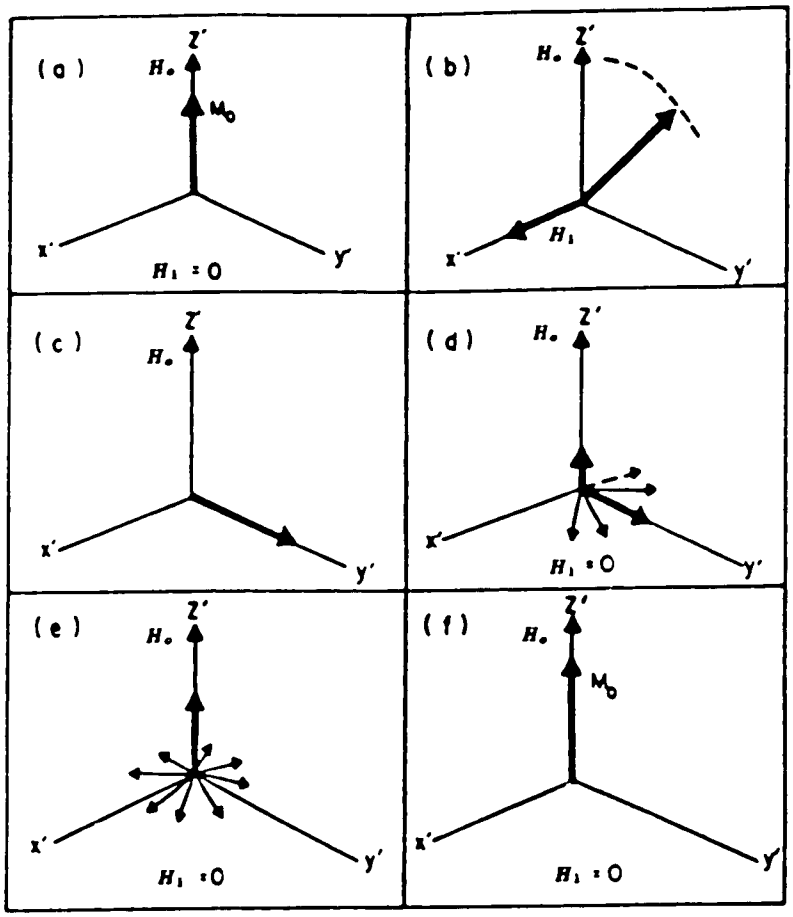

Figure 2.7: Rotating frame diagrams describing pulsed NMR and Relaxation phenomenon. (a) The net magnetization $\vec{M}_o$ is aligned along the magnetic field direction. (b) and (c) An 90° rf pulse H_1 is applied perpendicular to H_o to tip $\vec{M}_o$ by 90°. (d) and (e) After the pulse, the spins begin to relax in $x' - y'$ plane due to spin-spin (T_2) processes and inhomogeneity of field H_o, and in the z' direction due to spin-lattice (T_1) processes. (f) The equilibrium magnetization is reestablished along $\vec{H}_o$.

which is the inverse of the line width, is composed of three parts [34],

$$\frac{1}{T_2^*} = \frac{1}{2T_1} + \frac{1}{T_2} + \text{inhomogeneous broadening.} \tag{2.20}$$

Since in solids, $T_1 \gg T_2$, the above expression reduces to,

$$\frac{1}{T_2^*} = \frac{1}{T_2} + \text{inhomogeneous broadening.} \tag{2.21}$$

If a line is homogeneously broadened, then $T_2^* = T_2$, and one is not able to observe spin-echoes.

2.4 NQR Phenomenon

Nuclei with spin greater than 1/2 have not only a magnetic moment but also an electric quadrupole moment. The electrostatic interaction of the quadrupole moment with its environment is given by [37],

$$\mathcal{H} = \int \rho(\vec{x})V(\vec{x})d^3\vec{x}, \tag{2.22}$$

where $\rho(\vec{x})$ is the nuclear charge density, $V(\vec{x})$ is electrostatic potential arising from all the other charges surrounding the nucleus, and the integral is over the nuclear volume. Expanding the potential $V(\vec{x})$ into a power series about the nuclear center of charge, we have,

$$\mathcal{H} = \int d^3\vec{x}\rho(\vec{x}) \left\{ V_o + \sum_j \left(\frac{\partial V}{\partial x_j}\right)_o x_j + \frac{1}{2}\sum_{jk}\left(\frac{\partial^2 V}{\partial x_j \partial x_k}\right)_o x_j x_k + \ldots \right\} \tag{2.23}$$

where the summation over each subscript extends from 1 to 3. The subscript o indicates a quantity which is evaluated at the center of charge $x = 0$ and which can be taken outside the integral sign, so,

$$\mathcal{H} = Z_e V_o + \sum_j P_j \left(\frac{\partial V}{\partial x_j}\right)_o + \frac{1}{2}\sum_{jk} Q'_{jk}\left(\frac{\partial^2 V}{\partial x_j \partial x_k}\right)_o + \ldots, \tag{2.24}$$

where

$$\int d^3\vec{x}\rho(\vec{x}) = Ze = \text{nuclear charge}, \tag{2.25}$$

$$\int d^3\vec{x}\rho(\vec{x})x_j = P_j = \text{electric dipole moment vector}, \tag{2.26}$$

$$\int d^3\vec{x}\rho(\vec{x})x_j x_k = Q'_{jk} = \text{electric quadrupole moment tensor}. \tag{2.27}$$

The first term is of no interest to us, since it is independent of nuclear size, shape and orientation, hence will remain constant during nuclear reorientations. The second term, in fact all even terms, vanishes since the center of mass and center of charge coincide. So,

$$\mathcal{H} = \frac{1}{2}\sum_{jk} Q'_{jk}V_{jk} + \text{hexadecapole and higher terms}, \tag{2.28}$$

where $V_{jk} = (\frac{\partial^2 V}{\partial x_j \partial x_k})_o$ is the electric field gradient (EFG). We see that the nuclear electric quadrupole moment interacts with the EFG. Now, defining

$$Q_{jk} = 3Q'_{jk} - \delta_{jk}\sum_j Q'_{jj} \tag{2.29}$$

$$eQ \equiv \int \rho(\vec{x})(3z^2 - r^2)d^3\vec{x}, \tag{2.30}$$

then, all the quadrupole components can be expressed in terms of Q, the scalar quadrupole moment. It follows that, for spherical nuclear charge distribution, $Q = 0$.

It is always possible to choose so-called principal axes of the EFG tensor so that V_{jk} is diagonal. Label the principal axes XYZ such that

$$|V_{ZZ}| \geq |V_{YY}| \geq |V_{XX}|. \tag{2.31}$$

Because $\nabla^2 V = 0$, only two independent parameters are left in the diagonal EFG. Define

$$eq \equiv V_{ZZ} = \left(\frac{\partial^2 V}{\partial Z^2}\right)_o, \tag{2.32}$$

$$\eta \equiv \frac{(V_{XX} - V_{YY})}{V_{ZZ}} \qquad 0 \leq \eta \leq 1, \tag{2.33}$$

where eq is the largest principal field gradient, η is the asymmetry parameter, which measures the departure of the EFG tensor from cylindrical symmetry. In the principal axes XYZ,

$$\mathcal{H}_Q = A\left[3I_Z^2 - I^2 + \frac{\eta}{2}(I_+^2 + I_-^2)\right], \tag{2.34}$$

where

$$A = \frac{e^2qQ}{4I(2I-1)}, \tag{2.35}$$

$$I_\pm = I_X \pm iI_Y \qquad \text{as usual,} \tag{2.36}$$

and e^2qQ is the quadrupole coupling constant.

When the EFG is spherically symmetric, or of cubic symmetry, $eq = 0$, so that $\mathcal{H}_Q = 0$; when the EFG is cylindrically symmetric, $\eta = 0$. When $\eta = 0$, the matrix elements of $\mathcal{H}_Q$ will be,

$$< m|\mathcal{H}_Q|m' >= A[3m^2 - I(I+1)]\delta_{mm'} \tag{2.37}$$

and the energy levels are

$$E_m = A[3m^2 - I(I+1)]. \tag{2.38}$$

We see that the quadrupole energies are doubly degenerate in m, since the two states $\Psi_{\pm m}$ have the same energy. For half integer spins there are $I + \frac{1}{2}$ energy levels all doubly degenerate, while for integer spins there are $I + 1$ energy levels where I of them are doubly degenerate.

When $\eta \neq 0$, the energy levels become more complicated. For half integer spin nuclei, the energy levels are found by solving the secular equation of the $\mathcal{H}_Q$. For $I = \frac{3}{2}$, the secular equation can be solved exactly to obtain the energy levels [38],

$$E_{\pm\frac{3}{2}} = 3A\left(1 + \frac{\eta^2}{3}\right)^{\frac{1}{2}}, \tag{2.39}$$

$$E_{\pm\frac{1}{2}} = -3A\left(1+\frac{\eta^2}{3}\right)^{\frac{1}{2}}. \tag{2.40}$$

Note that the energy levels are still degenerate; only one line can be excited.

For integer spins the energy levels can be solved exactly. The energy levels for $I = 1$ are

$$E_{\pm} = A(1 \pm \eta), \tag{2.41}$$

$$E_0 = -2A, \tag{2.42}$$

giving rise to 3 NQR lines,

$$\nu_{\pm} = \frac{3e^2qQ}{4h}(1 \pm \frac{\eta}{3}), \tag{2.43}$$

$$\nu_d = \nu_+ - \nu_- = \frac{\eta e^2qQ}{2h}. \tag{2.44}$$

By detecting any two of these lines, e^2qQ and η can be determined.

Transitions between different energy levels are possible if an oscillating magnetic field is applied and its frequency satisfies the resonant condition

$$\Delta E = h\nu. \tag{2.45}$$

The nature of this induced transition is the same as the NMR case, the oscillating field interacts with the magnetic dipole moment of the nucleus. Since now the different energy levels are not equally spaced, several resonant lines may be observed. The energy levels for $I = \frac{5}{2}$ are shown in figure 2.8(a).

2.5 NQR Linewidth

In broad-line NMR, great attention has been paid to resonance line shapes; much useful information can be gleaned from them. However, a general theory of line shape for NQR has not been developed yet: NQR linewidths have not been generally of interest. In

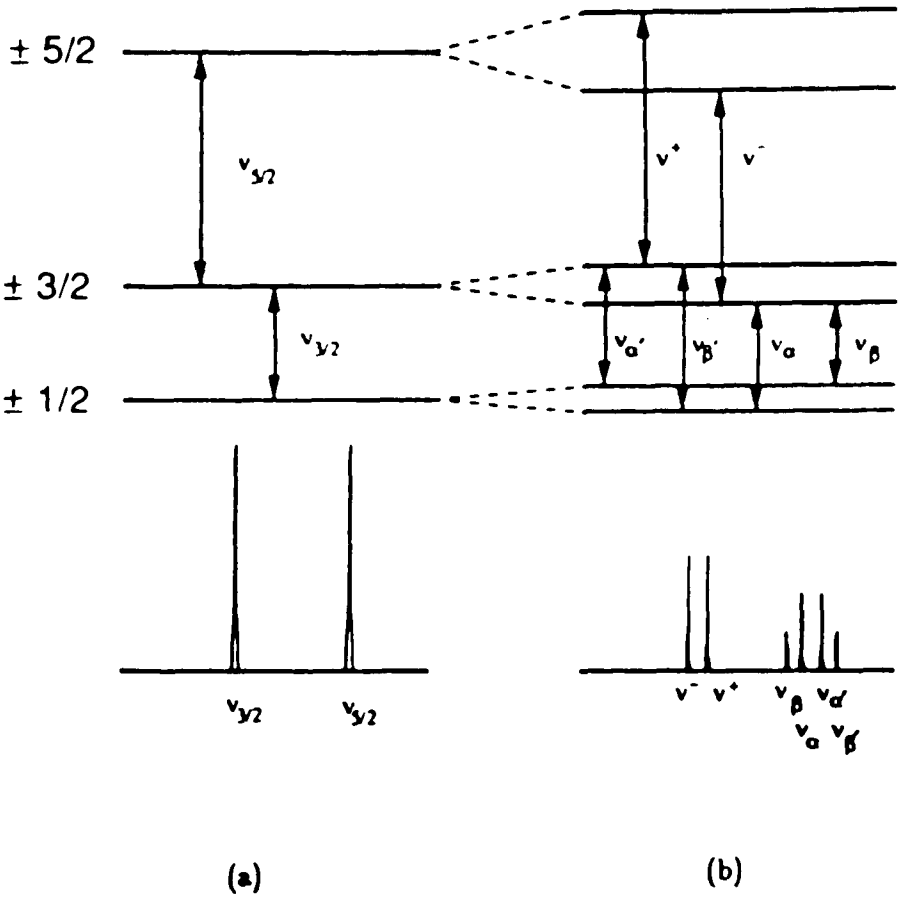

Figure 2.8: Zeeman effect in NQR. Top low, quadrupole energy levels of spin $\frac{5}{2}$ nuclei (a) Without magnetic field H_o. (b) With small field H_o. Bottom low, the corresponding NQR transition lines.

this section, I will discuss some differences between the sources of linewidth between NQR and NMR.

Eq. 2.21 is still valid for NQR, except that the contribution to inhomogeneous broadening is very different. In NQR, the inhomogeneity of the electric field gradient is the main source of inhomogeneous line broadening, which occurs when individual spins see a slightly different EFG, thus forming a frequency distribution. The sources of inhomogeneous EFG could be inperfect crystal structures, impurities, strains and dislocations. In general, any disorder in the crystal has an effect in broadening NQR lines, and NQR is rarely observed in amorphous materials due to the difficulty in detecting very broad lines. The presence of impurity ions or molecules has the effect of increasing the linewidth and decreasing the apparent intensity. Fedin and Kitaigorodskii [39] have shown that a single impurity molecule can affect several hundred molecules' NQR frequency.

The effects of lattice motion on NQR linewidths differ from those of NMR in one important respect. There the lattice motion only affects the perturbing hamiltonian and result in a narrowing of NMR line. In the NQR case, molecular motions affect the local EFG thus the main quadrupole hamiltonian. Two kinds of molecular motions, torsional oscillations and hindered rotations, were considered by Abragam [32], and their effects were to broaden NQR lines. Since the amplitude of molecular motion is a function of temperature, temperature dependence of the NQR frequency and linewidth has been studied extensively. Normally, the NQR frequency decreases when the temperature rises since rapid molecular motions partially average the EFG to a smaller value. It is also shown that the spin-lattice relaxation time T_1 decreases as temperature increases, thus, at certain high temperatures, T_1 can contribute to T_2^* and broaden the resonance line.

2.6 The Zeeman Effect in NQR

When a small constant magnetic field H_o (50 -200 Gauss) is applied along the $\hat{z}$ axis at polar and azimuthal angles θ and ϕ with respect to the principal Z axis, the total hamiltonian becomes $\mathcal{H} = \mathcal{H}_Q + \mathcal{H}_M$, where $\mathcal{H}_M$ expressed in the principal XYZ axes has the form,

$$\mathcal{H}_M = -\hbar\omega_o(I_Z\cos\theta + I_X\sin\theta\cos\phi + I_Y\sin\theta\sin\phi), \tag{2.46}$$

whith $\omega_o = \gamma H_o$.

For $\hbar\omega_o \ll e^2qQ$, $\mathcal{H}_M$ can be treated as a small perturbation. The m degeneracy of the quadrupole energy levels will be removed. In the case of $\eta = 0$, for $|m| > \frac{1}{2}$, the originally degenerate energy level split to become two levels,

$$E_{\pm m} = A[3m^2 - I(I+1)] \mp m\hbar\omega_o\cos\theta. \tag{2.47}$$

Thus, for $|m| > \frac{1}{2}$, the $\pm m \rightarrow \pm(m+1)$ transitions are split by a magnetic field into a doublet equally spaced at $\pm\omega_o\cos\theta$ from the original line, and each line has half the intensity of the unsplit line. The Zeeman splitting $2\omega_o\cos\theta$ of such a pair is maximum for $\theta = 0°$ and zero for $\theta = 90°$. Their intensities are independent of the orientation of the Zeeman field. This orientational dependence of the Zeeman splitting permits one to locate the symmetry axes of the EFG tensor experimentally.

In powdered crystals, there is an isotropic distribution of the orientations of the principal axes, thus all possible values of θ are equally likely and the Zeeman splitting is wiped out. The resulting resonant line is uniformly broadened with a width $2\omega_o$ and centered at the original line. Therefore, there will always be a small contribution of about 150 Hz to the NQR linewidth from the earth's magnetic field of 0.5 G.

For $|m| = \frac{1}{2}$, since $\mathcal{H}_M$ has finite off-diagonal elements between $\pm\frac{1}{2}$ states, there is zero-order mixing of the states $\Psi_{\pm\frac{1}{2}}$, so that new states Ψ_+ and Ψ_- are formed with energies given by,

$$E_\pm = A[\frac{3}{4} - I(I+1)] \mp \frac{f}{2}\hbar\omega_o\cos\theta, \tag{2.48}$$

where

$$f = [1 + (I + \frac{1}{2})^2 \tan^2\theta]^{\frac{1}{2}}. \tag{2.49}$$

The $\Delta m = \pm 1$ transitions between the mixed $\Psi_\pm$ and the $\Psi_{\pm\frac{3}{2}}$ states give four lines, labeled as ν_α, ν_β, $\nu_{\alpha'}$, and $\nu_{\beta'}$. The frequencies and intensities of these four lines depend on the angle θ. This orientational dependence also allows one to locate the symmetric axis experimentally. A detailed description of this technique can be found in ref. 38.

Fig. 2.8(b) depicts the quadrupolar energy levels of $I = \frac{5}{2}$ nuclei under the influence of small magnetic field.

2.7 Quadrupolar Effects in NMR

When $\vec{H}_o$ is large such that $\hbar\omega_o \gg e^2qQ$, it is $\mathcal{H}_Q$ that can be treated as the small perturbation. In the case of $\eta = 0$, the total hamiltonian expressed in the laboratory xyz axes is [32, 35],

$$\begin{aligned}
\mathcal{H}_T &= \mathcal{H}_M + \mathcal{H}_Q \\
&= -\gamma\hbar I_z H_o + A[3I_Z^2 - I^2] \\
&= -\gamma\hbar I_z H_o + A[3I_z^2\cos^2\theta + 3I_x^2\sin^2\theta + \\
&\qquad 3(I_zI_x + I_xI_z)\sin\theta\cos\theta - I^2].
\end{aligned} \tag{2.50}$$

To first order in the perturbation, the transition m to $m-1$ becomes,

$$\nu_m = \nu_o - \nu_Q\frac{m - \frac{1}{2}}{2}[3\cos^2\theta - 1], \tag{2.51}$$

where

$$\begin{aligned}
\nu_o &= \frac{\gamma H_o}{2\pi}, \qquad \text{the unperturbed NMR frequency,} \\
\nu_Q &= \frac{3e^2qQ}{2I(2I-1)h}.
\end{aligned} \tag{2.52}$$

In a single crystal, there are $2I$ transitions whose positions depend on θ. The situation of a single crystal with $\eta = 0$ and $I = \frac{3}{2}$, is shown in Fig. 2.9 [40]. The $m = \frac{1}{2}$ to

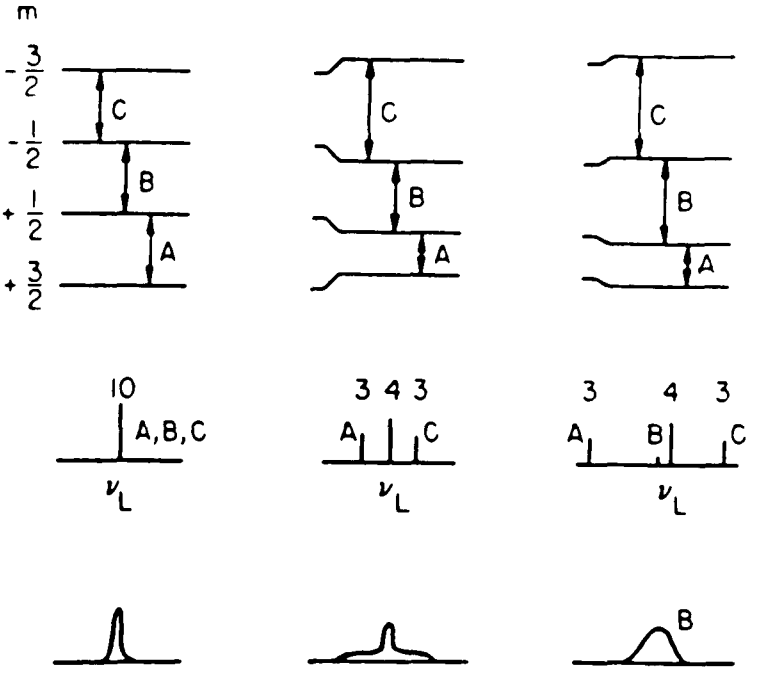

Figure 2.9: Quadrupole splitting of NMR of Spin $\frac{3}{2}$. Top: energy levels. Middle: spectrum of a single nucleus. The numerals indicate relative intensities. Bottom: line shape in an imperfect crystal. Left: no quadrupole interaction. Center: first-order splitting of satellites. Right: second-order shifting of central component. ν_L is Larmor frequency.

$m = -\frac{1}{2}$ transition (the central transition) is unshifted. The $2I - 1$ other transitions are called "satellite" transitions, they are symmetrically disposed about the central component in a pair corresponding to the transitions $m \leftrightarrow m - 1$ and $-(m - 1) \leftrightarrow -m$. In a glass or powdered crystal, all possible orientations will be equally likely and the resulting lineshape will be a "powder pattern". The first order powder pattern for $I = \frac{3}{2}$, $\eta = 0$, is shown in Fig. 2.10(a).

When $\mathcal{H}_Q$ is stronger, it may be necessary to consider second order perturbation effects. The frequency shift for the central transition m to $m - 1$, calculated to second order is

$$\nu_m = \nu_o - \nu_Q \frac{(m - \frac{1}{2})}{2}(3\cos^2\theta - 1) + \frac{\nu_Q^2}{72\nu_o}B \tag{2.53}$$

where B is a function of θ, m, and I. Usually in crystalline powders or glasses only the central line is observed, when second order is considered, because it is not shifted to first order, whereas the satellite transitions are broadened so much that they are undetectable. From Eq. 2.53 we can see that the width of the second order powder pattern of the central line is inversely proportional to the NMR frequency. This fact can be used as an experimental check on the order of the perturbation. The second order powder pattern for $I = \frac{3}{2}$, $\eta = 0$ is shown in Fig. 2.10(b).

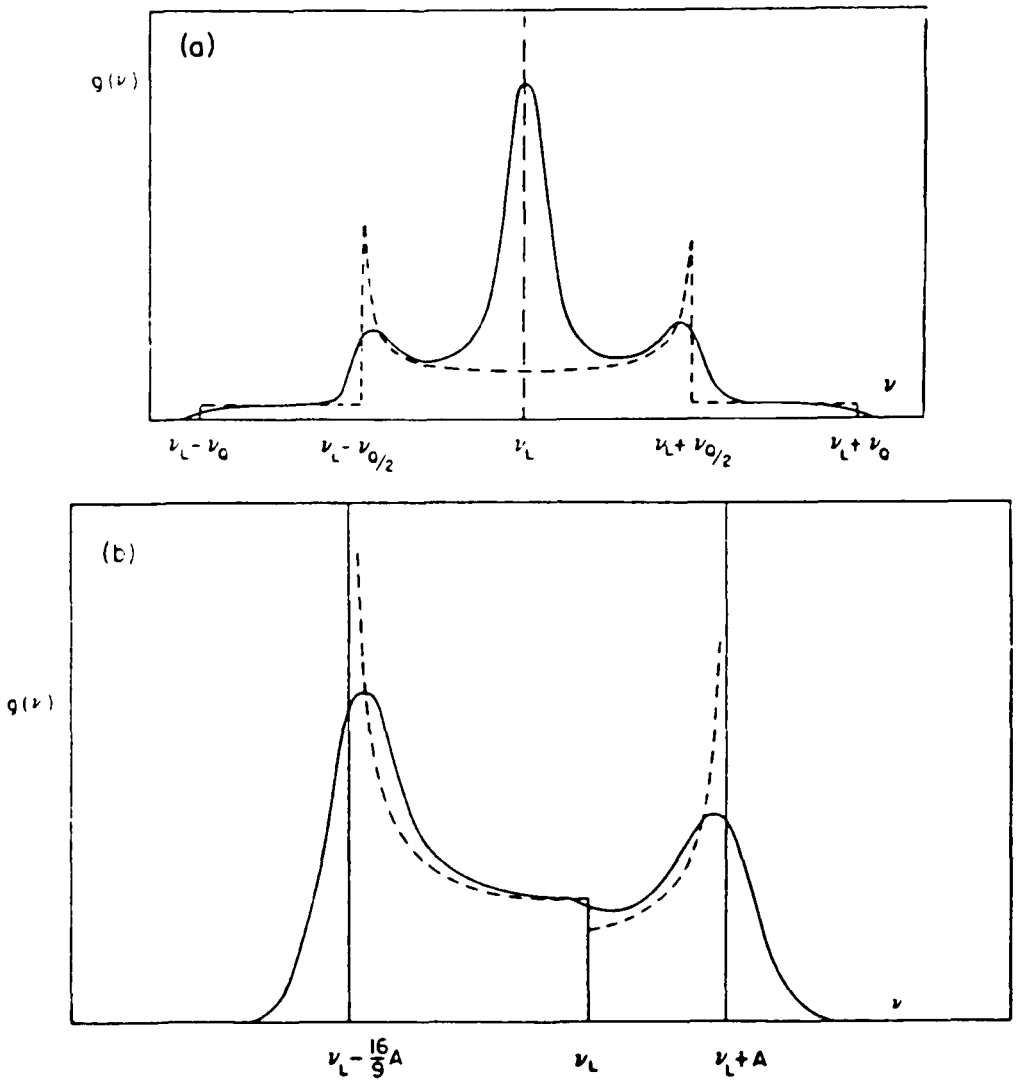

Figure 2.10: NMR powder patterns due to quadrupolar interaction of symmetric field gradient. (after N. Bloembergen [41]). (a) First-order pattern for $I = \frac{3}{2}$, $\nu_Q = \frac{e^2qQ}{2h}$. Dashed curve is obtained from theory. With dipolar broadening superimposed, the solid curve results. (b) Second-order pattern, central component, $A = (a - \frac{3}{4})\nu_Q^2/16\nu_L$, ν_L = Larmor frequency. Dotted curve derives from theory. Solid curve includes dipolar broadening.

Chapter 3

Brief Description of Dressed Atom Theory for Magnetic System

3.1 Hamiltonian of a Dressed Atom

If a system has hamiltonian $\mathcal{H}_{nd}$ and is subjected to two irradiations, $H_1 \cos(\omega_1 t)$ and $H_2 \cos(\omega t)$, instead of considering all of the possible transition which the two irradiations could produce, the "dressed" atom theory will consider an atom dressed by the photons of non-resonant field H_2 , whose more complex energy levels are then probed by the resonant field H_1 . The fundamental question is, what are the energy levels and other properties of the combination "atom plus field". The relevant hamiltonian then consists of three parts: $\mathcal{H}_{nd}$, the original nude system, $\mathcal{H}_{rf}$, the quantum field operator for the rf dressing irradiation; and V, the interaction between the original system and the dressing field.

In the presence of a static magnetic field H_o along the z axis,

$$\mathcal{H}_{nd} = -\hbar\gamma H_o I_z = \omega_o I_z \tag{3.1}$$

where $\omega_o = -\gamma H_o$ is the Lamour frequency, I_z is the z component of angular momentum operator, $\hbar$ has been set to be equal to 1, and γ is the gyromagnetic ratio. In general, $\gamma = g\mu_B$, where g is the Landé g-factor, and μ_B is the Bohr magneton. In the field H_o, an energy level will be split into $(2I+1)$ Zeeman levels, each with quantum number m, where $-I \leq m \leq I$, and energy separation ω_o. We shall refer to these $(2I+1)$ levels as $|\, m >$ with eigenenergy $m\omega_o$.

For an rf field with frequency ω and polarization $\vec{\varepsilon}$, the quantum field hamiltonian

is written as

$$\mathcal{H}_{rf} = \omega a^{+} a, \tag{3.2}$$

where a^{+} and a are the creation and annihilation operators. The eigenstates of this hamiltonian are $\mid n >$ with corresponding eigenenergies $n\omega$, representing n photons of the filed. The effect of the operators a^{+} and a on the state $\mid n >$ is, as usual,

$$\begin{aligned} a^{+} \mid n > &= \sqrt{n+1} \mid n+1 > \\ a \mid n > &= \sqrt{n} \mid n-1 > \end{aligned} \tag{3.3}$$

In quantum theory, electric and magnetic fields are operators defined for each mode (frequency ω and polarization $\vec{\epsilon}$) which act on the field state described by photons. If the rf field is uniform over the whole region where there are atoms, the mode of the rf field can be taken to be that of a plane wave in the dipole approximation, then the operator of the magnetic field is,

$$\vec{H}_2 = \mu(a\vec{\epsilon} + a^{+}\vec{\epsilon}^{*}) \tag{3.4}$$

where μ is a constant which measures, in some way, the "magnetic field of a photon". The magnitude of this constant is extremely small, 10^{-14} G, corresponding to a typical experimental situation. This exposes that magnetic fields commonly used contain a very large number of photons.

The rf fields realized in experiments have a well defined phase. They are represented by states $\mid \alpha >$ which are a coherent superposition of states of different number of photons. These states, called "coherent" states have been studied in detail by Glauber [42]. They are defined as eignstates of the annihilation operator:

$$a \mid \alpha >= \alpha \mid \alpha > \tag{3.5}$$

their time development expansion in terms of the basis states $\mid n >$ is,

$$\mid \alpha(t) >= \epsilon^{-\frac{1}{2}|\alpha|^2} \sum_{n} \frac{\alpha^n e^{-in\omega t}}{(n!)^{\frac{1}{2}}} \mid n > \tag{3.6}$$

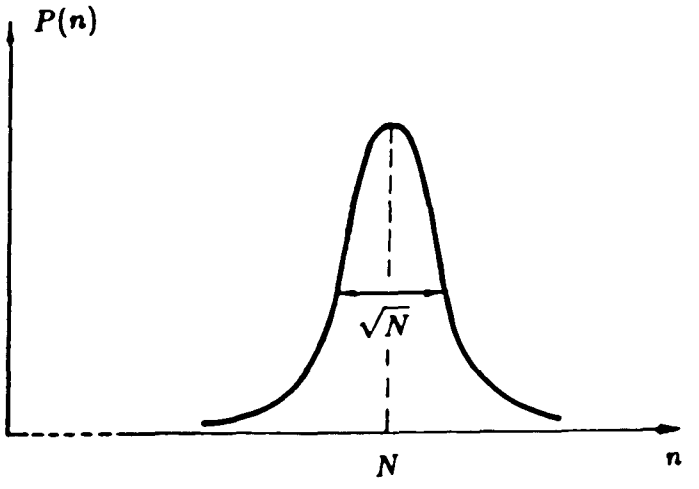

Figure 3.1: Probability $P(n)$ to find n photons in the rf field as function of photon number n.

The probability $P(n)$ to find n photons in the rf field is a Poisson distribution centered at the mean photon number $N = |\alpha|^2$ (we limit ourselves to real values of α), and with relative distribution width given by $\sqrt{N}$, as shown in Fig. 3.1.

The quantum coupling between the atom and the rf field is obtained from the classical magnetic dipolar interaction,

$$V_{Cl} = -\gamma \vec{J} \bullet \vec{H}_{Cl}(t) \tag{3.7}$$

where $\vec{J}$ is the total angular momentum, $\vec{J} = \hbar \vec{I}$. According to the fundamental properties [42] of the coherent state $|\alpha(t)>$, the mean value of the magnetic field operator in this state is equal to the classical value of the rf field. Thus, the quantum mechanical expression for the interaction hamiltonian V is obtained by replacing $\vec{H}_{Cl}(t)$ in Eq. 3.7 by the field operator Eq. 3.4,

$$V = \lambda \vec{J} \bullet (a\vec{\varepsilon} + a^{+}\vec{\varepsilon}^{*}) \tag{3.8}$$

where the coupling constant $\lambda = -\gamma\mu$ can be evaluated to be,

$$\lambda = -\frac{\gamma H_2}{2\sqrt{N}} = \frac{\omega_2}{2\sqrt{N}} \tag{3.9}$$

with $\omega_2 = -\gamma H_2$ the strength of the dressing field.

For a linearly polarized rf field along the oz axis (π polarization),

$$V_\pi = \lambda J_z(a + a^+) \tag{3.10}$$

For a circularly polarized rf field with its rotating axes along (or opposite to) the oz axis (σ_+ or σ_- polarization),

$$V_{\sigma_+} = \lambda(aJ_+ + a^+J_-) \tag{3.11}$$

$$V_{\sigma_-} = \lambda(aJ_- + a^+J_+) \tag{3.12}$$

For a linear polarized field along ox axis perpendicular to oz axis, σ polarization, the field is a coherent superposition of σ_+ and σ_- photons,

$$\begin{aligned} V_\sigma &= \lambda J_x(a + a^+) \\ &= \frac{\lambda}{2}(aJ_+ + a^+J_-) + \frac{\lambda}{2}(aJ_- + a^+J_+) \end{aligned} \tag{3.13}$$

where $J_\pm = J_x \pm iJ_y$, as usual.

One can write the total hamiltonian of the dressed atom in this form:

$$\mathcal{H} = \mathcal{H}_o + V \tag{3.14}$$

where $\mathcal{H}_o = \omega_o I_z + \omega a^+ a$, has eigenstates $\mid m, n >$ and eigenenergies $m\omega_o + n\omega$.

3.2 Resolvent Method

When the dressing is weak, i.e.

$$\omega_2 << \omega, \omega_o, \tag{3.15}$$

one can treat V as a small perturbation on $\mathcal{H}_o$. The energy level diagram of $\mathcal{H}_o$ for $J = \frac{1}{2}$ is shown in Fig. 3.2. Due to the presence of rf photons, the energy diagram shows an infinite number of crossing points. The crossing happens when $\omega_o = (n - n')\omega$, and the crossing points are labeled as I_n^P where level $| +, n >$ crosses with $| -, n + P >$ ($J = \frac{1}{2}$, so states $| \pm\frac{1}{2} >$ are simply expressed as $| \pm >$).

We know that the effect of the perturbation V on the levels of $\mathcal{H}_o$ can be very important whenever some energy levels are degenerate, that is for all crossing points of the levels of $\mathcal{H}_o$. It is therefore essential to determine the behavior of the levels of the dressed atom near these points. To this end, one can appeal to the resolvent method which allows one to comfortably separate the degenerate levels of interest from all the others. Since the resolvent method will also be used in other section of this thesis, the main formulas are described below [3, 1].

The resolvent $G(z)$ of the hamiltonian $\mathcal{H}$ is defined as,

$$G(z) = \frac{1}{z - \mathcal{H}} \tag{3.16}$$

$G(z)$ is simply related to the evolution operator $U(t) = e^{-i\mathcal{H}t}$:

$$U(t) = \frac{1}{2\pi i} \int_c e^{-izt} G(z) dz \tag{3.17}$$

where C is the contour in the complex plane shown in Fig. 3.3. $G(z)$ is an analytic function on the complex z plane except eventually on the real axis where poles and cuts corresponding to the discrete and continuous eigenvalues of $\mathcal{H}$ may be found.

For $t > 0$ ($t < 0$), only the part of the contour C above (below) the real axis gives a non zero contribution.

If $| a >$ and $| b >$ are eigenstates of $\mathcal{H}_o$, then $< a | G(z) | a >$ gives the probability amplitude that, the system being in state $| a >$ at $t = 0$, remains in the same state at time t under the effect of V; $< b | G(z) | a >$ give the transition amplitude for the system from $| a >$ to $| b >$ under the effect of V.

Depending on the problem to be solved, usually, only a few elements of the matrix $G(z)$ need be evaluated. So, we need the projection, $\bar{G}(z)$, of $G(z)$, into a subspace,$\mathcal{E}$,

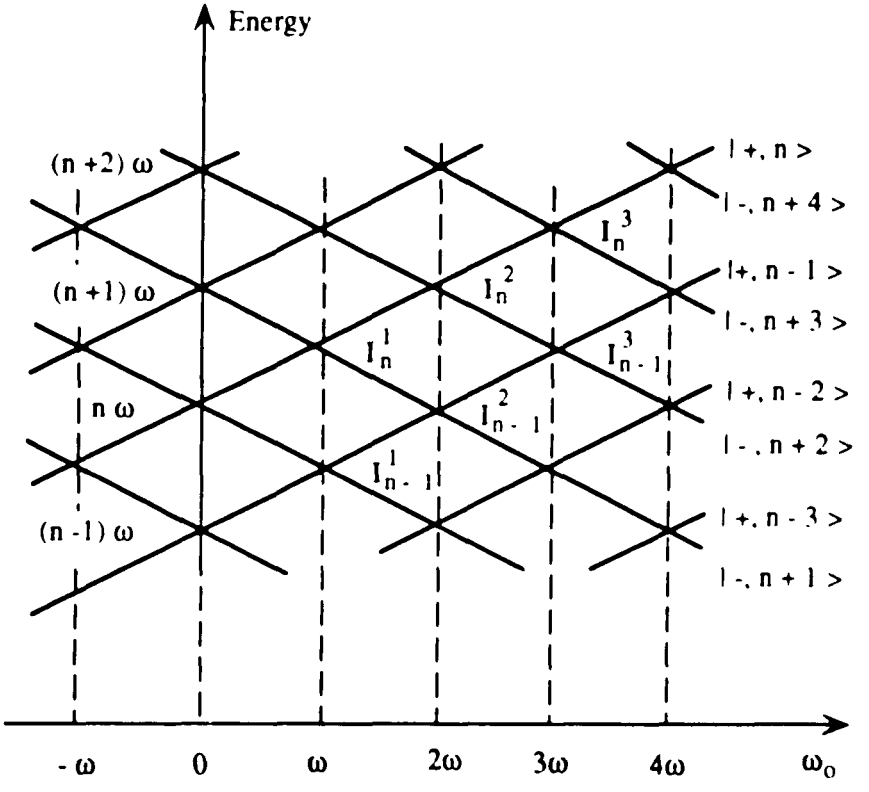

Figure 3.2: Energy level diagram of hamiltonian $\mathcal{H}_o = \omega_o I_z + \omega a^+ a$ as function of static magnetic field $\omega_o = -\gamma H_o$ for $J = \frac{1}{2}$ atoms.

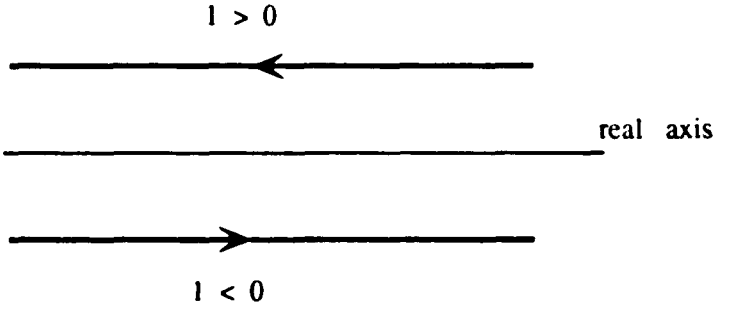

Figure 3.3: Contour C in the complex plane.

of the Hilbert space. The subspace ε may be chosen to be spanned by the eigenstates of $\mathcal{H}_o$, or, just be subtended by an energy level crossing point of $\mathcal{H}_o$ depending on the problem. If P (and Q) are the projections onto (out of) ε, we have,

$$\bar{G}(z) = PG(z)P \tag{3.18}$$

and

$$\begin{aligned} P^2 &= P, \quad P+Q = 1, \quad PQ = 0, \\ Q^2 &= Q, \quad [P,\mathcal{H}_o] = 0, \quad [Q,\mathcal{H}_o] = 0 \end{aligned} \tag{3.19}$$

Also, in a general way for any operator A:

$$\bar{A} = PAP. \tag{3.20}$$

$\bar{G}$ and $\bar{A}$ are projections of operator G and A which operate only inside ε.

The explicit expression of $\bar{G}(z)$ can be derived as,

$$\bar{G}(z) = \frac{1}{z - \bar{\mathcal{H}}_o - \bar{R}(z)} \tag{3.21}$$

where $\bar{R}(z)$ gives the effect of perturbation V. For small V, $\bar{R}(z)$ can be expressed as,

$$\bar{R}(z) = PVP + PV\frac{Q}{z-\mathcal{H}_o}VP + PV\frac{Q}{z-\mathcal{H}_o}V\frac{Q}{z-\mathcal{H}_o}VP + \ldots \tag{3.22}$$

One may keep the first one or two non zero terms of $\bar{R}(z)$ for small perturbation.

The eigenenergies of $\mathcal{H}$ are the poles of $\bar{G}(z)$, that is to say, the zeros of the following equations:

$$z - \bar{\mathcal{H}}_o - \bar{R}(z) = 0. \tag{3.23}$$

When solving the eigenenergies and eigenstates of $\mathcal{H}$ near the crossing of $\mathcal{H}_o$, one may replace the value of $\bar{R}(z)$ approximately by $\bar{R}(E_c)$, where E_c is the degenerate common energy, and solve the secular equation of

$$\tilde{\mathcal{H}} = \bar{\mathcal{H}}_o + \bar{R}(E_c) \tag{3.24}$$

where $\tilde{\mathcal{H}}$ is an effective hamiltonian of $\mathcal{H}$ referred to the multiplicity of degenerate levels.

3.3 Crossing and Anticrossings of Energy Level Diagram

Now let's apply the above formulas to an angular momentum $J = \frac{1}{2}$ system to illustrate their use. As before, $|a>$ and $|b>$ are eigenstates of $\mathcal{H}_o$ that cross at common energy E_c. According to Eq. 3.24, eigenenergies of $\mathcal{H}$ are eigenvalues of the following matrix,

$$\begin{bmatrix} E_a + \bar{R}_{aa} & \bar{R}_{ab} \\ \bar{R}_{ba} & E_b + \bar{R}_{bb} \end{bmatrix} \tag{3.25}$$

where by taking the first two terms in Eq. 3.22, $\bar{R}(E_c)$ has the form,

$$\bar{R}_{aa} = \sum_{i \neq a,b} \frac{<a|V|i><i|V|a>}{E_c - E_i}, \tag{3.26}$$

$$\bar{R}_{bb} = \sum_{i \neq a,b} \frac{<b|V|i><i|V|b>}{E_c - E_i}, \tag{3.27}$$

and

$$\bar{R}_{ab} = <a|V|b> + \sum_{i,j,\cdots,k \neq a,b} \frac{<a|V|i><i|V|j> \cdots <k|V|b>}{(E_c - E_i)(E_c - E_j)\cdots(E_c - E_k)} \tag{3.28}$$

The diagonal elements of the matrix $\bar{R}_{aa}$ (or $\bar{R}_{bb}$) describe virtual transitions to levels $|i>$ other than $|a>$ and $|b>$, while the off-diagonal elements of the matrix $\bar{R}_{ab}$ describe real transitions from level $|a>$ to $|b>$ either directly or through intermediate levels $|i> |j> \cdots |k>$. Two fundamentally different cases occur depending on whether there exists a coupling $\bar{R}_{ab}$ between the two levels $|a>$ and $|b>$.

3.3.1 Level Crossings

If $|a>$ and $|b>$ are not coupled by V, $\bar{R}_{ab} = 0$, to all orders, we have the crossing case. From Eq. 3.25, in the neighbourhood of crossing, the eigenenergies of $\mathcal{H}$ are,

$$\begin{aligned} E_{\bar{a}} &= E_a + \bar{R}_{aa} \\ E_{\bar{b}} &= E_b + \bar{R}_{bb} \end{aligned} \tag{3.29}$$

Equations 3.25 and 3.29 are just the standard second order non-degenerate perturbation formula. Under the influence of virtual transitions to levels $|i>$ other than $|a>$

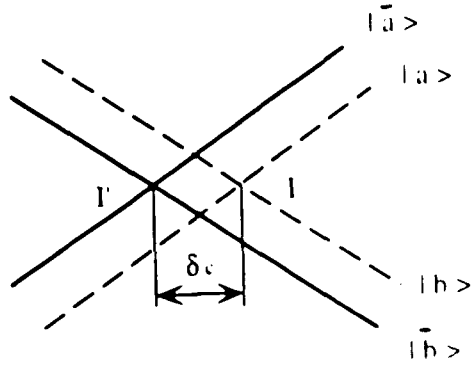

Figure 3.4: The crossing point I is shifted to I' due to virtual transitions.

and $|b>$, the two levels which cross at point I are then shifted to point I', which differs from I by an amount δ_c, which is second order in V, as shown in Fig. 3.4.

As for the eigenstates of $\mathcal{H}$, they are, to zero order, identical to the unperturbed states of $\mathcal{H}_o$, $|a>$ and $|b>$. To higher order, they are given, near the level crossing, by classic expressions of non-degenerate perturbation theory which relate the changes in the levels to different orders under the influence of non-resonant virtual transitions. They can be written, up to a normalization constant:

$$|\bar{a}>=|a>+\frac{Q}{E_c-\mathcal{H}_o}V|a>+\frac{Q}{E_c-\mathcal{H}_o}V\frac{Q}{E_c-\mathcal{H}_o}V|a>+\cdots \qquad (3.30)$$

Due to the effect of V, the eigenstates of $\mathcal{H}$ now contain admixtures of states with different photon numbers.

3.3.2 Level Anticrossings

If $|a>$ and $|b>$ are coupled by V, $\bar{R}_{ab}\neq 0$, we have the anticrossing case.

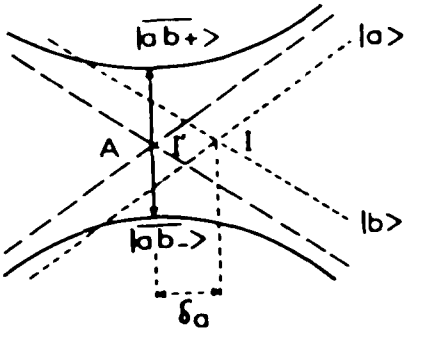

Figure 3.5: Due to virtual and real transitions, level crossing becomes shifted anticrossing.

By solving Eq. 3.25, we have,

$$E_{\bar{ab},\pm} = \frac{E_a + E_b + \bar{R}_{aa} + \bar{R}_{bb}}{2} \pm \frac{1}{2}\sqrt{(E_a + \bar{R}_{aa} - E_b - \bar{R}_{bb})^2 + 4|\bar{R}_{ab}|^2} \qquad (3.31)$$

The structure of Eq. 3.31 is shown in Fig. 3.5. Because of the effect of virtual transitions to levels $|i>$ other than $|a>$ and $|b>$, as in the *1st* case, level crossing point I are shifted to I' by an amount δ_a which is *2nd* order in V. Because of the effect of real transitions between $|a>$ and $|b>$, described by the non-diagonal elements of the matrix $\bar{R}_{ab}$, the levels thus shifted also repel one another following two branches of an hyperbola to form an anticrossing centered at I'. The minimum distance A between the two levels which anticross is equal to twice the intensity of the coupling, $2\bar{R}_{ab}$. As for the eigenstates of $\mathcal{H}$ near I', to the order of zero which is the only one of interest to us here, they are made up of a mixture of the two non-perturbed states $|a>$ and $|b>$, which can be expressed as,

$$\begin{aligned} |\overline{ab,+}> &= \cos\frac{\theta}{2}|a> + \sin\frac{\theta}{2}|b> \\ |\overline{ab,-}> &= -\sin\frac{\theta}{2}|a> + \cos\frac{\theta}{2}|b> \end{aligned} \qquad (3.32)$$

with,

$$\tan\frac{\theta}{2} = \frac{2\bar{R}_{ab}}{E_a + \bar{R}_{aa} - E_b - \bar{R}_{bb}} \tag{3.33}$$

The effect of the dressing photons not only changes the energy levels of the atom, but also produces a profound change in the eigenfunctions of the system. The original states $|a>$ and $|b>$ are no longer eigenstates and the atom oscillates between the states $|a>$ and $|b>$. The transition probability $P_{a\to b}(t)$ of the dressed atom from the state $|a>$ at time $t = 0$ to be at the state $|b>$ at time t can be gotten through the following. Reversing Eq. 3.32, we got,

$$|a> = \cos\frac{\theta}{2}\,|\overline{ab,+}> - \sin\frac{\theta}{2}\,|\overline{ab,-}> \tag{3.34}$$

The time evolution of state $|a>$ is,

$$|a(t)> = \epsilon^{-i\mathcal{H}t}\,|a> = \cos\frac{\theta}{2}\,\epsilon^{-iE_{|\overline{ab,+}>}t}\,|\overline{ab,+}> - \sin\frac{\theta}{2}\,\epsilon^{-iE_{|\overline{ab,-}>}t}\,|\overline{ab,-}> \tag{3.35}$$

Then, the probability of the dressed atom to be at state $|b>$ at time t is,

$$P_{a\to b}(t) = |<b|a(t)>|^2 = \sin^2\theta\sin^2\left(\frac{E_{|\overline{ab,+}>} - E_{|\overline{ab,-}>}}{2}\right)t \tag{3.36}$$

Eq. 3.36 is just the well known formula of Breit and Rabi [43, 44]. At anticrossing, $P_{a\to b}(t)$ has its maximum value, while far away from the anticrossing, $P_{a\to b}(t)$ is small. For $J = \frac{1}{2}$, and σ polarized rf field, the crossing I_n^{2P+1} crossed by states $|-, n>$ and $|+, n-(2P+1)>$ becomes an anticrossing of the dressed atom [3]. The atom oscillates from $|-, n>$ to $|+, n-(2P+1)>$ by absorbing $(2P+1)$ rf photons. The ordinary magnetic resonances and multiple quanta transitions are closely related to anticrossings of the dressed atom.

3.4 Energy Level Diagrams of $J = \frac{1}{2}$ System

Crossings and anticrossings are very important features of dressed atom energy diagrams and they can explain the various resonances due to photon dressing, like resonant

frequency shift, splittings, side bands, Haroche's resonances, multiple quantum transitions etc.. The energy levels of the dressed atom are simply deduced by considering the behaviour of the levels near the crossing points of $\mathcal{H}_o$, namely, whether they form shifted crossings or anticrossings. Different polarized rf photons bring different forms of the interaction hamiltonian V, thus, different energy level diagrams of the dressed atom. Whether the crossings of $\mathcal{H}_o$ in Fig. 3.2 remain crossings or become anticrossings of the dressed atom depends on whether the interaction V couples the crossed states. The detailed derivation of the energy level diagrams of dressed atoms can be found in Ref. 3 and 4, here we just illustrate their main features. Figs. 3.6 - 3.8 show the energy levels of a $J = \frac{1}{2}$ system in the presence of σ, σ_+ and π polarized photons, respectively. The solid lines are energy levels of hamiltonian $\mathcal{H}$ while the dashed lines are those of $\mathcal{H}_o$. Note that for π polarization, the energy levels of $\mathcal{H}$ are identical to those of $\mathcal{H}_o$ (with an energy translation $-\frac{\lambda^2}{4\omega}$) [45], all of the crossings of $\mathcal{H}_o$ remain as crossings of $\mathcal{H}$.

There is a very significant and interesting effect due to σ polarized photons, i.e. dressing field is linear and perpendicular to the static field. It is derived theoretically [3] and proved experimentally [15] that the slope of the energy levels near zero static field, which defines the Landé g factor of the dressed atom, is the following function of the dressing strength ω_2,

$$g = g_o J_o(\frac{\omega_2}{\omega}) \tag{3.37}$$

where g and g_o are the Landé factor for dressed atom and nude atom respectively, and J_o is the zero*th* order spherical Bessel function. Changes of the Landé factor of the atom in the presence of dressing photons imply a corollary change of all physical properties tied to the paramagnetism of the atomic level studied.

Modification of the Landé factor, together with the admixture of the eigenfunctions due to the photons, explain all the changes in the magnetic properties of the dressed systems.

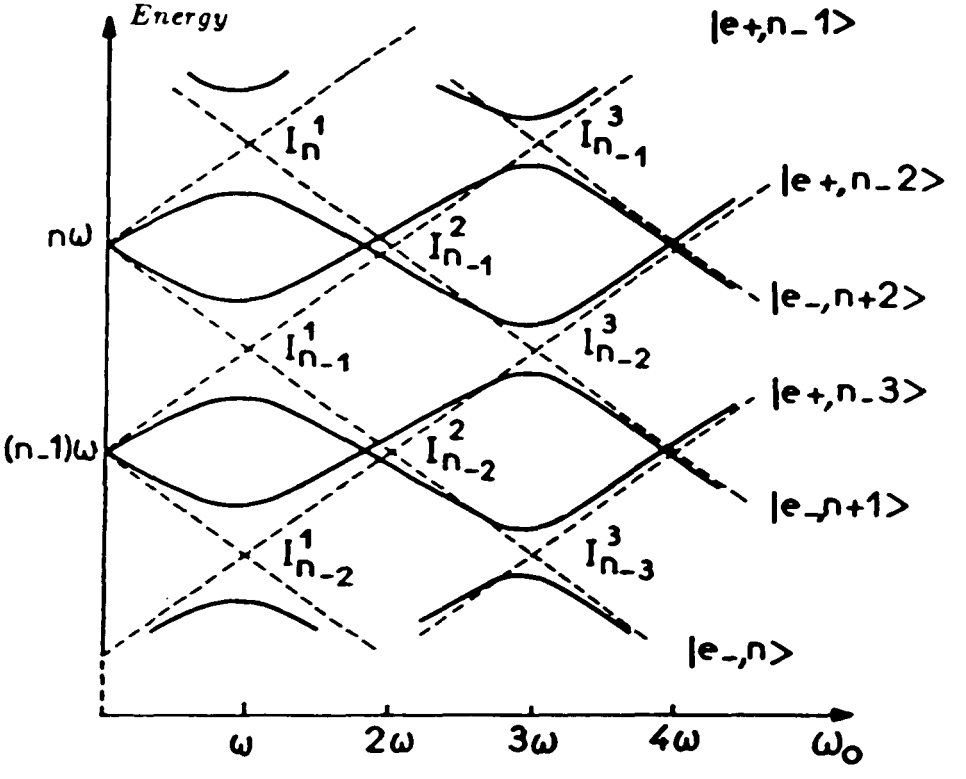

Figure 3.6: Energy level diagram of $J = \frac{1}{2}$ atom dressed by σ polarized photons as a function of the static field $\omega_o = -\gamma H_o$. Dashed lines are the unperturbed levels of hamiltonian $\mathcal{H}_o$, $e\pm$ stands for $m = \pm\frac{1}{2}$ respectively.

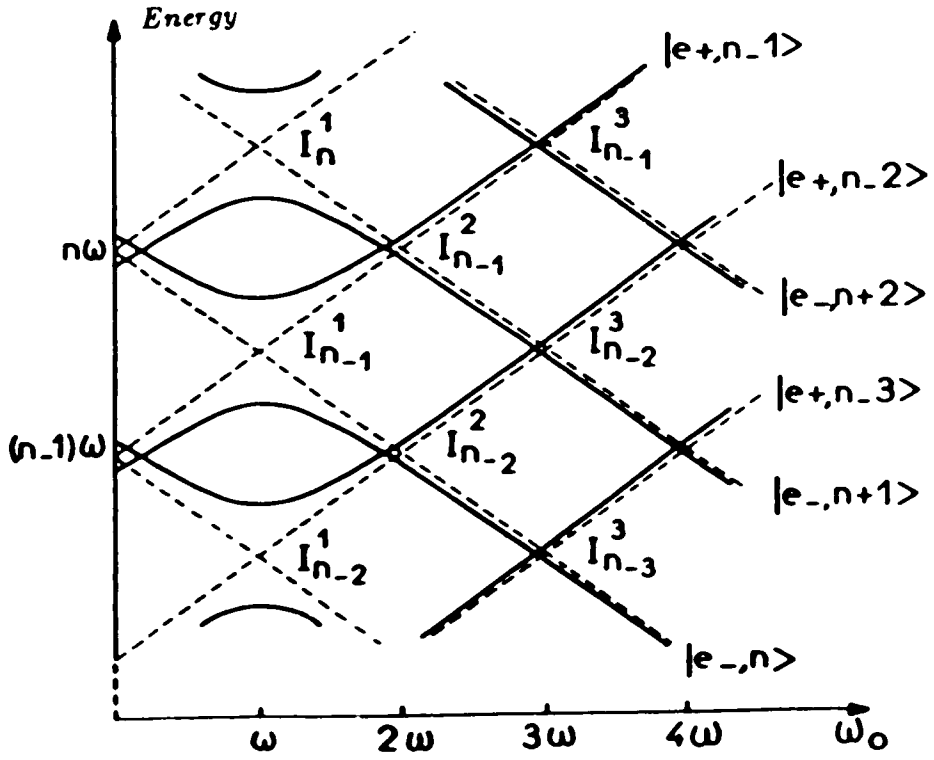

Figure 3.7: Energy level diagram of a $J = \frac{1}{2}$ system dressed by σ_+ polarized photons as function of the static field $\omega_o = -\gamma H_o$. Dashed lines are the unperturbed levels of the hamiltonian $\mathcal{H}_o$, $e\pm$ stands for $m = \pm\frac{1}{2}$ respectively.

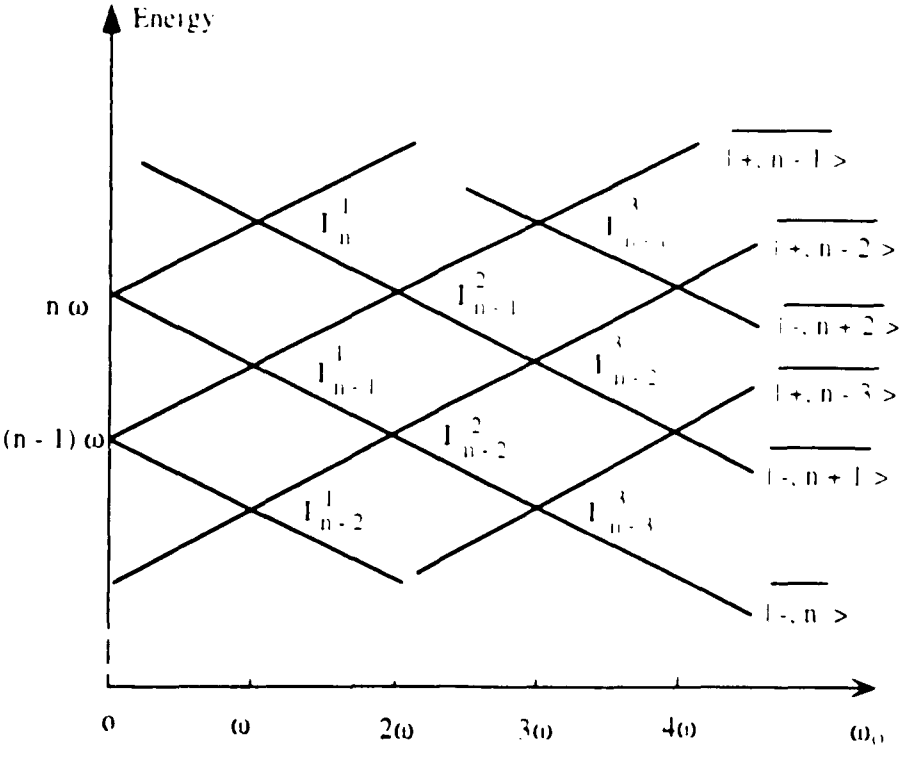

Figure 3.8: Energy level diagram of a $J = \frac{1}{2}$ system dressed by π polarized photons as a function of the static field $\omega_o = -\gamma H_o$. $e\pm$ stands for $m = \pm\frac{1}{2}$ respectively.

Chapter 4

Photon Dressing Theory for a Spin $I = 1$ Pure Quadrupolar System

Photon dressing theory for an $I = \frac{3}{2}$ pure quadrupolar system (single crystal of $NaClO_3$) has been worked out by Ito in 1982 [31]. The methods used and main features of the $I = \frac{3}{2}$ NQR photon dressing theory are basically extensible to any half integer spin system. In this chapter, I will develop the theory for integer spins, using $I = 1$ as the example. The difference in half-integer and integer spin cases arises mainly because the energy levels of half integer spins are all doubly degenerated, while for integer spin, there is one level, $m_\zeta = 0$, which is not degenerate. Integer spin nuclei are rare because they require an odd number of protons and an odd number of neutrons. This combination usually is not favored by nuclear binding energy considerations. However, ${}_7N^{14}$ nuclei have spin 1 and an abundance of about 99.6% [38], and have large quadrupole moment. Photon dressing theory for spin $I = 1$ NQR is studied because of its importance for Nitrogen compounds, but it will, of course, be applicable to any integer spin case, such as deuterium NQR. The methods used are similar to those used for $I = \frac{3}{2}$ nuclei. Guided by the conditions observed in our experiment, this treatment will be limited to the case of axially symmetric electric field gradients (EFG).

4.1 The Case of Linearly Polarized Dressing Field

4.1.1 Total Hamiltonian

The total hamiltonian of a nucleus plus the dressing photons is, according to Chapter 3,

$$\mathcal{H} = \mathcal{H}_Q + \omega a^+ a + V$$

$$= \mathcal{H}_o + V \tag{4.1}$$

where $\mathcal{H}_o = \mathcal{H}_Q + \omega a^+ a$, and $\mathcal{H}_Q$ is the nude hamiltonian for the nuclear quadrupole interaction. For axially symmetric EFG, and spin $I = 1$, we have,

$$\mathcal{H}_Q = \frac{\epsilon^2 qQ}{4}(3I_\zeta^2 - 2) \tag{4.2}$$

where ζ refers to the $\xi\eta\zeta$ principal axis system of the the EFG tensor. The eigenfunctions of $\mathcal{H}_Q$ are denoted by $|m_\zeta>$ with eigenenergy $E_Q^{m_\zeta}$. One can see that the eigenenergy $E_Q^{m_\zeta}$ is doubly degenerated in m_ζ. For $I = 1$ there are only two energy levels, one degenerate with $m_\zeta = \pm 1$, and the other non-degenerate with $m_\zeta = 0$. They are given by,

$$\begin{aligned} E_Q^{\pm 1} &= \frac{\epsilon^2 qQ}{4} = \frac{1}{3}\omega_Q \\ E_Q^{o} &= -\frac{\epsilon^2 qQ}{2} = -\frac{2}{3}\omega_Q \end{aligned} \tag{4.3}$$

where ω_Q is the NQR frequency which is the separation between these two energy levels and is equal to $\frac{3}{4}\epsilon^2 qQ$.

The eigenfunctions of $\mathcal{H}_o$ are denoted by $|m_\zeta, n>$ which is the direct product of the eigenfunctions of $\mathcal{H}_Q$ and $\omega a^+ a$, The corresponding eigenenergies are equal to $E_Q^{m_\zeta} + n\omega$.

The energy diagram of $\mathcal{H}_o$ is shown on Fig. 4.1. It consists of manifolds separated from each other by one photon energy ω; each manifold corresponds to a given value of n and is composed of two quadrupole energy levels corresponding to $m_\zeta = \pm 1$ and 0. The condition $\omega_Q >> \omega$ is applied so that there are overlaps between different manifolds of certain photon number. In the diagram, the long dashed lines, solid lines, and long-short dashed lines are used for manifolds of photon number $n + 1$, n, and $n - 1$ respectively. In contrast to the energy diagram of $\mathcal{H}_o$ in the magnetic resonance case, Fig. 3.2, this diagram of pure quadrupole system does not show any level crossing point.

The interaction term V in Eq. 4.1 has the form, according to Eq. 3.8,

$$V = \lambda \vec{I} \bullet (a\vec{\varepsilon} + a^+ \vec{\varepsilon}^*). \tag{4.4}$$

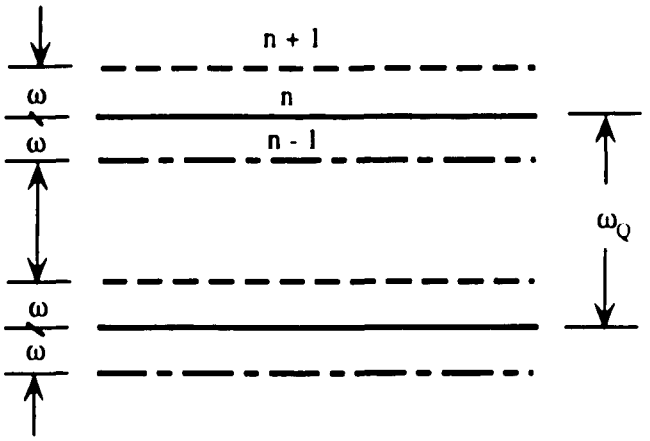

Figure 4.1: Engery level diagram of $\mathcal{H}_o = \mathcal{H}_Q + \omega a^+ a$ for $I = 1$ nuclei.

For a linearly polarized dressing field along the z axis,

$$\vec{\varepsilon} = \vec{k}, \qquad \text{and} \qquad \vec{\varepsilon}^* = \vec{\varepsilon}, \tag{4.5}$$

So we have,

$$V = \lambda \vec{I} \bullet \vec{k}(a + a^+) \tag{4.6}$$

The geometrical relation between the z axis and the $\xi\eta\zeta$ coordinate system is shown in Fig. 4.2, where θ is the angle between the z and the ζ axes, φ is the angle between the direction of orthogonal projection of the z axis into the $\xi\eta$ plane and the ξ axis. Then we have,

$$\vec{k} = \cos\theta \vec{\epsilon}_\zeta + \sin\theta \cos theta \vec{\epsilon}_\xi + \sin\theta \sin\varphi \vec{\epsilon}_\eta \tag{4.7}$$

and Eq. 4.6 becomes,

$$\begin{aligned} V &= \lambda \cos\theta I_\zeta (a + a^+) + \frac{\lambda}{2} \sin\theta e^{-i\varphi} I_+ (a + a^+) + \frac{\lambda}{2} \sin\theta e^{i\varphi} I_- (a + a^+) \\ &= V_\zeta + V_+ + V_- \end{aligned} \tag{4.8}$$

where

$$V_\zeta = \lambda \cos\theta I_\zeta (a + a^+)$$

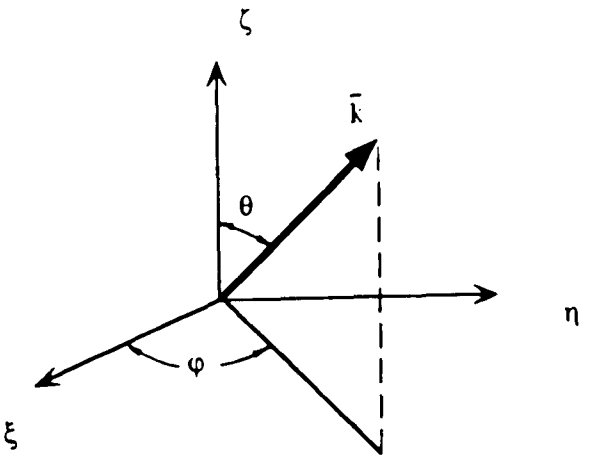

Figure 4.2: Geometrical relation of the oscillating field with the principal $\xi\eta\zeta$ axes.

$$V_+ = \frac{\lambda}{2}\sin\theta\, e^{-i\varphi} I_+ (a + a^+)$$

$$V_- = \frac{\lambda}{2}\sin\theta\, e^{i\varphi} I_- (a + a^+) \tag{4.9}$$

and

$$I_\pm = I_\xi \pm i I_\eta \tag{4.10}$$

are the raising and lowering operators in the principal axes. The effect of V_ζ won't change the quantum number m_ζ, while V_+ (V_-) will increase (decrease) the quantum number m_ζ by 1. Therefore the effect of V' can only join the states with $\Delta m_\zeta = 0, \pm 1$.

For systems with axially symmetric EFG, we can set $\varphi = 0$ in Eqs. 4.8 and 4.9.

The frequency ω of the nonresonant field should satisfy the condition

$$\omega_Q >> \omega > \frac{1}{T_2}, \tag{4.11}$$

where ω_Q and T_2 are the NQR frequency and transverse relaxation time of spin $I = 1$ nuclei under consideration, respectively. Therefore, the interaction of the nuclei with the nonresonant field can be treated as a small perturbation on the levels of $\mathcal{H}_o$ compared with the electric quadrupole interaction, and the effects of the magnetic dipole

interaction between the spin $I = 1$ nuclei and its neighbour nuclei can be neglected.

4.1.2 The Effects of V_1 within the Manifolds

Since the energy levels of $\mathcal{H}_o$ are doubly degenerate in m_ζ, the states with the same $|m_\zeta|$ have the same energy and are thus much more closely related to each other than to those with different $|m_\zeta|$, we can consider the effects of V on the states with same or different $|m_\zeta|$ separately. For $I = 1$, we consider two manifolds with $|m_\zeta| = 0$ and 1, respectively.

We use projection operator P onto the subspace subtended by $\mathcal{H}_o$,

$$\begin{aligned} P &= \sum_{m_\zeta} P_{m_\zeta} \\ P_{m_\zeta} &= \sum_{n} |m_\zeta, n><m_\zeta, n|, \end{aligned} \tag{4.12}$$

Then, divide V into two parts, V_1 and V_2, as follows,

$$\begin{aligned} V_1 &= \sum_{|m_\zeta|=|m'_\zeta|} P_{m_\zeta} V P_{m'_\zeta} \\ V_2 &= \sum_{|m_\zeta|\neq|m'_\zeta|} P_{m_\zeta} V P_{m'_\zeta} \end{aligned} \tag{4.13}$$

where V_1 has nonzero matrix elements within the manifolds $|\pm 1, n>$ and $|0, n>$, and V_2 between the manifolds.

We will first consider the changes due to V_1, then treat V_2 as perturbation between these modified manifolds.

The specific form of V_1 has five terms,

$$V_1 = P_1 V P_1 + P_1 V P_{-1} + P_{-1} V P_{-1} + P_{-1} V P_1 + P_0 V P_0 \tag{4.14}$$

The last term $P_0 V P_0$ is equal to zero, because the eigenvalue of V_ζ on state $|0, n>$ is zero. The state $|0, n>$ of $\mathcal{H}_o$ is not changed under the effect of V_1.

The terms P_1VP_{-1} and $P_{-1}VP_1$ are also equal to zero for they joint the states with $\Delta m_\zeta = \pm 2$.

The only contribution to V_1 is from P_1VP_1 and $P_{-1}VP_{-1}$, and they are calculated to be,

$$P_{\pm 1}VP_{\pm 1} \tag{4.15}$$

$$= \sum_{n,n'} |\pm 1, n><\pm 1, n|V|\pm 1, n'><\pm 1, n'|$$

$$= \pm\lambda\cos\theta \sum_{n,n'} |\pm 1, n><\pm 1, n|(a+a^+)|\pm 1, n'><\pm 1, n'| \tag{4.16}$$

In the manifold $|\pm 1, n>$, matrix elements V_1 only have diagonal terms. Isolating the manifold $|\pm 1, n>$ from the others and using the fictitious spin $\frac{1}{2}$ formalism, the effect of V_1 on $|\pm 1, n>$ can be written as,

$$V_1^{\pm 1} = \lambda\cos\theta\,\sigma_\zeta(a+a^+) \tag{4.17}$$

where $\sigma_\zeta = \begin{pmatrix} 1 & 0 \\ 0 & -1 \end{pmatrix}$ is the Pauli matrix in the manifold $|\pm 1, n>$.

Labelling the sum of the hamiltonians $\mathcal{H}_o$ and $V_1^{\pm 1}$ as $\mathcal{H}'$, $\mathcal{H}'$ has the form,

$$\mathcal{H}' = \mathcal{H}_Q + \omega a^+a + \lambda\cos\theta\,\sigma_\zeta(a+a^+) \tag{4.18}$$

We note that $\mathcal{H}'$ commutes with I_ζ, and as a result we can decompose it into $2I+1$ hamiltonians $\mathcal{H}'_{m_\zeta}$, each acting inside their own subspace $|m_\zeta, n>$ of given m_ζ. We also note, that $\mathcal{H}'$ includes two parts, where $\mathcal{H}_Q$ only acts on the nuclear states, while $\omega a^+a + V_1^{\pm 1}$ only act on the photon states. We rewrite the hamiltonian in the decomposed form and the photon part has the expression:

$$\mathcal{H}'^P_{\pm 1} = \omega a^+a \pm \lambda\cos\theta\,(a+a^+)$$

$$= \omega(a^+ \pm \frac{\lambda}{\omega}\cos\theta)(a \pm \frac{\lambda}{\omega}\cos\theta) - \frac{\lambda^2}{\omega}\cos^2\theta \tag{4.19}$$

Now let's introduce Glauber's unitary operator [42],

$$D(\pm\frac{\lambda}{\omega}\cos\theta) = e^{\mp\frac{\lambda}{\omega}\cos\theta(a^+ - a)} \tag{4.20}$$

and it displaces the operators a and a^+ according to the scheme,

$$\begin{aligned} D(\pm\frac{\lambda}{\omega}\cos\theta)a^+ D^+(\pm\frac{\lambda}{\omega}\cos\theta) &= a^+ \pm \frac{\lambda}{\omega}\cos\theta \\ D(\pm\frac{\lambda}{\omega}\cos\theta)a D^+(\pm\frac{\lambda}{\omega}\cos\theta) &= a \pm \frac{\lambda}{\omega}\cos\theta \end{aligned} \tag{4.21}$$

It follows that,

$$\mathcal{H}'^P_{\pm 1} = D(\pm\frac{\lambda}{\omega}\cos\theta)(\omega a^+ a - \frac{\lambda^2}{\omega}\cos^2\theta)\, D^+(\pm\frac{\lambda}{\omega}\cos\theta) \tag{4.22}$$

From this the spectum of $\mathcal{H}'_{\pm 1}$ can be immediately deduced:

$$E'_{\pm 1} = E_Q^{\pm 1} + n\omega - \frac{\lambda^2}{\omega}\cos^2\theta \tag{4.23}$$

The $m_\zeta = \pm 1$ states are still energy degenerate under the effect of V_1. The eigenenergy of $\mathcal{H}'$ is approximately equal to that of $\mathcal{H}_o$, because, by using Eq. 3.9,

$$\frac{\lambda^2}{\omega}\cos^2\theta = \frac{(\gamma H_2)^2}{4N\omega}\cos^2\theta \doteq 0, \tag{4.24}$$

where γ, $\cos\theta$ are of the order of 1, ω is in the value of a few thousand Hertz, H_2 is a few tens Gauss. We know that it takes about 10^{28} photons to make up the magnetic field of 1 Gauss [4], that is to say, N is in the order of 10^{29}. So, Eq. 4.24 is totally justified.

The eigenstates of $\mathcal{H}'_{\pm 1}$ labeled by $|\overline{\pm 1, n}>$, are given by,

$$|\overline{\pm 1, n}> = \exp[\mp\frac{\lambda}{\omega}\cos\theta\,(a^+ - a)]\ |\pm 1, n> \tag{4.25}$$

The effect of V_1 although does not quite change the energy levels of $\mathcal{H}_o$, but causes the admixture of states of different photon number n. Transitions between states of different n is forbidden, because the electric dipole operator and the rf operators commute so

that the selection rule for an optical transition is $\Delta n = 0$. Due to the effect of V_1, transitions between the states $|0, n>$ and $|\overline{\pm 1, n'}>$ become possible. The transition frequency is $\omega_Q + (n - n')\omega$, when n' equals n, it gives the main NQR line ω_Q; when n' differs from n, it gives sidebands located at either side of ω_Q with a separation of $(n - n')\omega$ in frequency. The intensities of these lines are proportional to the square of the matrix element $< 0, n|\mathcal{H}_I|\overline{\pm 1, n'}>$ with $\mathcal{H}_I$ the electric dipole operator.

4.1.3 The Effect of V_2 as a Perturbation

Now let us consider the effect of V_2 between the states $|\overline{\pm 1, n}>$ and $|0, n>$. The explicit form for V_2 has four terms:

$$V_2 = P_1 V P_0 + P_0 V P_1 + P_{-1} V P_0 + P_0 V P_{-1} \tag{4.26}$$

by using the formula of raising and lowering operators,

$$I_\pm |I, m> \;=\; \sqrt{(I \mp m)(I \pm m + 1)}\, |I, m + 1>, \tag{4.27}$$

V_2 is calculated to be,

$$\begin{aligned} P_{\pm 1} V P_0 \;&=\; P_{\pm 1} V_\pm P_0 \\ &=\; \frac{\sqrt{2}}{2}\lambda \sin\theta \sum_{n,n'} |\pm 1, n> < \pm 1, n|(a + a^+)|\pm 1, n'> < 0, n'| \end{aligned} \tag{4.28}$$

$$\begin{aligned} P_0 V P_{\pm 1} \;&=\; P_0 V_\mp P_{\pm 1} \\ &=\; \frac{\sqrt{2}}{2}\lambda \sin\theta \sum_{n,n'} |0, n> < 0, n|(a + a^+)|0,, n'> < \pm 1, n'| \end{aligned} \tag{4.29}$$

It is clear that V_2 is a hermitian operator. Treating V_2 as a small perturbation on states $|\overline{\pm 1, n}>$ and $|0, n>$, the energy change due to 2nd order non-degenerate perturbation theory, is given by,

$$\Delta E_{|\overline{\pm 1, n}>} \;=\; \sum_{n'} \frac{|< \overline{\pm 1, n}|V_2|0, n'>|^2}{\omega_Q + (n - n')\omega}$$

$$\Delta E_{|0,n>} = \sum_{n'} \frac{|<0,n|V_2|\overline{1,n'}>|^2 + |<0,n|V_2|\overline{-1,n'}>|^2}{-\omega_Q + (n-n')\omega} \tag{4.30}$$

where $\omega_Q = E_Q^{\pm 1} - E_Q^0$, with $\hbar \equiv 1$.

Now we need to calculate these matrix elements. We will calculate one of them in detail and for the rest of them just give their expressions. Let

$$y_2 = +\frac{\lambda}{\omega}\cos\theta\,(a^+ - a), \tag{4.31}$$

then

$$\begin{aligned} <\overline{1,n}|V_2|0,n'> &= <1,n|\exp(y_2)|P_1 V P_0|0,n'> \\ &= \frac{\sqrt{2}}{2}\lambda\sin\theta\sum_{r,s}<1,n|\exp(y_2)|1,r> \\ &\qquad <1,r|(a+a^+)|1,s><0,s|0,n'> \end{aligned} \tag{4.32}$$

where r and s are photon numbers, the summation over n and n' in Eqs. 4.28 and 4.29 has been replaced by r and s to avoid confusion. Using Eq. 3.3 and the relation derived by Polonsky [45],

$$<n|\exp[-\frac{\lambda}{\omega}(a^+ - a)]|n'> = J_{n-n'}(\frac{\omega_2}{\omega}) \tag{4.33}$$

where $J_{n-n'}$ is the $(n-n')th$ order spherical Bessel function, and noting that V_2 and the exponential $\exp[y_2]$ only act on the photon states, we have,

$$\begin{aligned} &<\overline{1,n}|V_2|0,n'> \\ &= \frac{\sqrt{2}}{2}\lambda\sin\theta\sum_{r,s}<n|\exp(y_2)|r>\cdot\{\sqrt{s}<r|s-1> \\ &\qquad + \sqrt{s+1}<r|s+1>\}\cdot<s|n'> \\ &= \frac{\sqrt{2}}{2}\lambda\sin\theta\sum_{r}J_{n-r}(x_2)\{\sqrt{r+1}<r+1|n'> + \sqrt{r}<r-1|n'>\} \\ &= \frac{\sqrt{2}}{2}\lambda\sin\theta\{\sqrt{n'}\,J_{n-n'+1}(x_2) + \sqrt{n'+1}\,J_{n-n'-1}(x_2)\} \end{aligned} \tag{4.34}$$

where

$$x_2 = -\frac{\omega_2}{\omega}\cos\theta. \tag{4.35}$$

Here we need to make an approximation. As mentioned before, the dressing field we are studying consists of a very large number of photons. Consider the photon distribution curve shown in Fig. 3.1 of Chapter 3. Most of the photons present are near the average photon number N. Therefore,

$$\sqrt{n'} \doteq \sqrt{n'+1} \doteq \sqrt{n'+P} \doteq \sqrt{N} \tag{4.36}$$

where P is an integer. P could be of the order of hundred*ths* or even thousand*ths*, but compare to N, it is negligible.

Using the relation of spherical Bessel functions,

$$J_n(x) = \frac{x}{2n}\{J_{n-1}(x) + J_{n+1}(x)\} \tag{4.37}$$

and the expression for λ as in Eq. 3.9, we finally get,

$$\begin{aligned} < \overline{1,\, n}\,|V_2|\,0,\, n' > &\doteq \frac{\sqrt{2}}{4}\omega_2 \sin\theta\,\{J_{n-n'+1}(x_2) + J_{n-n'-1}(x_2)\} \\ &= -\frac{\sqrt{2}}{2}\omega\tan\theta\,(n-n')\,J_{n-n'}(x_2) \end{aligned} \tag{4.38}$$

Similarly, we can get,

$$< \overline{-1,\, n}\,|V_2|\,0,\, n' > = \frac{\sqrt{2}}{2}\omega\tan\theta\,(n-n')\,J_{n-n'}(x_1) \tag{4.39}$$

where

$$x_1 = \frac{\omega_2}{\omega}\cos\theta = -x_2. \tag{4.40}$$

And,

$$\begin{aligned} < 0,\, n\,|V_2|\,\overline{1,\, n'} > &= < \overline{-1,\, n}\,|V_2|\,0,\, n' > \\ < 0,\, n\,|V_2|\,\overline{-1,\, n'} > &= < \overline{1,\, n}\,|V_2|\,0,\, n' > \end{aligned} \tag{4.41}$$

Note that the expressions of these four matrix elements are very similar except for their sign and for the argument of the Bessel functions. With the help of another relation of spherical Bessel functions,

$$J_{-n}(x) = (-1)^n J_n(x) = J_n(-x) \tag{4.42}$$

we can see that, after squaring, these four matrix elements all give the same value. So we can conclude that after perturbation of V_2, the states $|\overline{\pm 1, n}>$ are still energy degenerate. The energy change of these states, by inserting the above matrix elements into Eq. 4.30 are expressed below,

$$\begin{aligned} \Delta E_{|\overline{\pm 1,n}>} &= \sum_{n'} \frac{\frac{1}{2}\omega^2 \tan^2\theta\,(n-n')^2 J^2_{n-n'}(x_1)}{\omega_Q + (n-n')\omega} \\ &= \sum_{P} \frac{\frac{1}{2}\omega^2 \tan^2\theta\, P^2 J^2_P(x_1)}{\omega_Q + P\omega} \end{aligned} \tag{4.43}$$

$$\Delta E_{|0,n>} = \sum_{P} \frac{\omega^2 \tan^2\theta\, P^2 J^2_P(x_1)}{-\omega_Q + P\omega} \tag{4.44}$$

where $P = n - n'$. For the summation over n', n' can take the values from 1 to ∞, theoretically. Therefore the summation over P should start from $n-1$ to $n-\infty$, which includes three parts, $P = 0$, from 1 to $n-1$, and from -1 to $n-\infty$. ΔE is caused by the coupling of V_2 between states with different photon numbers, this coupling becomes smaller and smaller when the difference in photon number P getting bigger and bigger. Therefore we can extend the summation over P and take it from 1 to ∞ and -1 to $-\infty$. The part that P equal to zero has no contribution to ΔE, so from Eq. 4.43 we have,

$$\begin{aligned} \Delta E_{|\overline{\pm 1,n}>} &= \sum_{P=1}^{\infty} \frac{\frac{1}{2}\omega^2 \tan^2\theta\, P^2 J^2_P(x_1)}{\omega_Q + P\omega} + \sum_{P=-\infty}^{-1} \frac{\frac{1}{2}\omega^2 \tan^2\theta\, P^2 J^2_P(x_1)}{\omega_Q + P\omega} \\ &= \sum_{P=1}^{\infty} \frac{1}{2}\omega^2 \tan^2\theta\, P^2 J^2_P(x_1) \left(\frac{1}{\omega_Q + P\omega} + \frac{1}{\omega_Q - P\omega} \right) \\ &= \sum_{P=1}^{\infty} \frac{\omega^2 \tan^2\theta\, P^2 J^2_P(x_1)}{\omega_Q^2 - P^2\omega^2} \end{aligned} \tag{4.45}$$

To express ΔE in normalized form, divide Eq. 4.45 by ω. We then have,

$$\frac{\Delta E_{|\widetilde{\pm 1, n}>}}{\omega} = \tan^2\theta \sum_{P=1}^{\infty} \frac{\frac{\omega}{\omega_Q}}{1 - P^2(\frac{\omega}{\omega_Q})^2} P^2 J_P^2(\frac{\omega_2}{\omega}\cos\theta) \tag{4.46}$$

In the same way, from Eq. 4.44, we get,

$$\frac{\Delta E_{|0, n>}}{\omega} = -2\tan^2\theta \sum_{P=1}^{\infty} \frac{\frac{\omega}{\omega_Q}}{1 - P^2(\frac{\omega}{\omega_Q})^2} P^2 J_P^2(\frac{\omega_2}{\omega}\cos\theta) \tag{4.47}$$

Examining Eqs. 4.46 and 4.47, we see the following effects: The perturbation of V_2 shifts the energy level of $|\widetilde{\pm 1, n}>$ upward and $|0, n>$ downward; the amount of downward shift is twice as much as the upward shift; the amount of energy shifts are not functions of photon number n, which implies that, the NQR frequency shift caused by this energy change is uniform for both main line and side bands.

4.1.4 Energy level Diagrams of the Dressed Nuclei

Adding up E' and ΔE, we get the spectrum of the dressed nuclei. Labelling the states of the total hamiltonian $\mathcal{H}$ as $|\widetilde{\pm 1, n}>$ and $|\widetilde{0, n}>$, and expressing their energies in normalized dimensionless form, we have,

$$\frac{E_{|\widetilde{\pm 1, n}>}}{\omega} = \frac{1}{3}\frac{\omega_Q}{\omega} + n + \tan^2\theta \sum_{P=1}^{\infty} \frac{\frac{\omega}{\omega_Q}}{1 - P^2(\frac{\omega}{\omega_Q})^2} P^2 J_P^2(\frac{\omega_2}{\omega}\cos\theta) \tag{4.48}$$

and

$$\frac{E_{|\widetilde{0, n}>}}{\omega} = -\frac{2}{3}\frac{\omega_Q}{\omega} + n - 2\tan^2\theta \sum_{P=1}^{\infty} \frac{\frac{\omega}{\omega_Q}}{1 - P^2(\frac{\omega}{\omega_Q})^2} P^2 J_P^2(\frac{\omega_2}{\omega}\cos\theta) \tag{4.49}$$

The energy levels are plotted as a function of dressing field strength $\frac{\omega_2}{\omega}$ by numerical computation using Eqs. 4.48 and 4.49. The summation over P from 1 to infinity is treated as follows. The Bessel function $y = J_P(x)$ is an oscillating function, its amplitude decays when x gets bigger. The starting oscillating amplitude of $J_P(x)$ gets smaller when P gets bigger. $J_0(x)$ has the largest starting oscillating amplitude which is equal to 1. The computational program is set that $J_P(x)$ is added up for $P = 1$ to

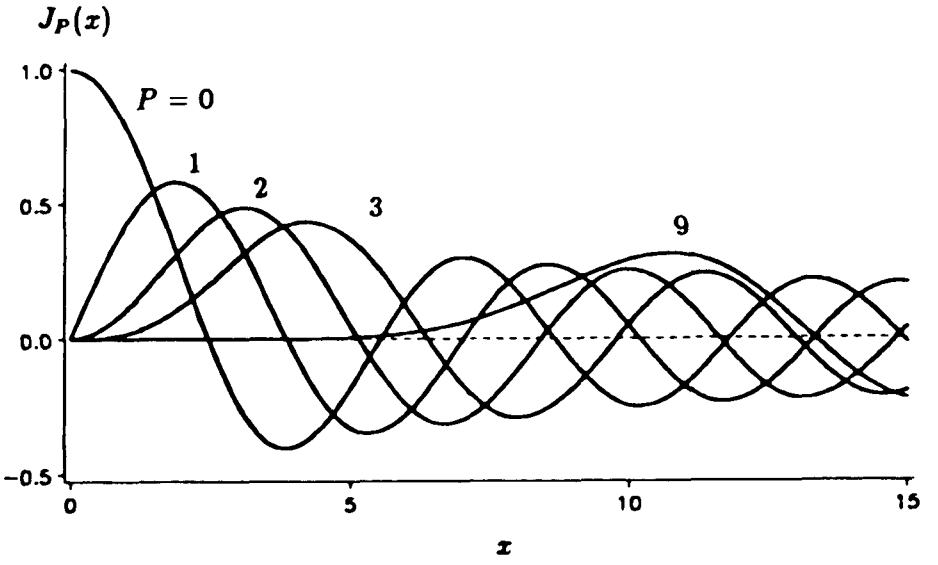

Figure 4.3: Spherical Bessel function $J_P(x)$ vs. x for $P = 0, 1, 2, 3,$ and 9.

$P = 40$, for $P > 40$, if $|J_P|$ value is bigger than 10^{-40}, its value is added, otherwise, the program stops adding. One question arises that is it possible that for certain values of P and x, $J_P(x) = 0$, but $|J_{P+1}(x)| > 0$? If this is possible, then the program set in the above mentioned way is not correct. This question is fully taken care of. If x_P^n is the n*th* root of $J_P(x)$, from the theory of Bessel function [46], we know,

$$\begin{aligned} x_{P+1}^n &> x_P^n, && \text{for same n, and,} \\ x_P^{n+1} &> x_P^n, && \text{for same } P. \end{aligned} \tag{4.50}$$

This situation is illustrated in Fig 4.3. The argument of the Bessel function in Eqs. 4.48 and 4.49 is $\frac{\omega_2}{\omega}\cos\theta$. The maximum dressing strength we are considering is about $\frac{\omega_2}{\omega} = 10$, which corresponds to a range of 0 to 10 for the argument x. Table 4.1 list the first zeros x_P^1 of $J_P(x)$, which are determined from Newton's formula [47]

$$x_n = x_{n-1} - \frac{f(x_{n-1})}{f'(x_{n-1})}. \tag{4.51}$$

The starting point x_0 for x_0^1 equals 2.4, and those for x_P^1 are taken as x_{P-1}^1. The values

P	0	1	2	3	4	5
x_p^1	2.4048	3.8317	5.1356	6.3802	7.5883	8.7715
P	6	7	8	9	10	11
x_p^1	9.9361	11.0864	12.2251	13.3543	14.4755	15.5898

Table 4.1: First zeroes of spherical Bessel function $J_P(x)$.

of Bessel function are calculated by using subroutine DBSJNS in IMSL of Fortran Subroutines for Mathematical Application. It is clear from the table that the range of interest only covers the first zeroes up to $J_6(x)$. As a result, the above mentioned program is justified. Eqs. 4.48 and 4.49 are functions of angle θ. For different relative orientations of the oscillation dressing field and the principal ζ axis, the dressed nuclei have different energies. When a powdered or polycrystalline sample is under study, the resulting energy diagram will spread out to a certain width. When $\theta = 90^o$, the term $\tan\theta J_P(\frac{\omega_2}{\omega}\cos\theta) = \infty \cdot 0$ for $P \neq 0$, so the value of E is not computable. The limit value of $\Delta E/\omega$ when $\theta = 90^o$ is theoretically calculated, they have the forms,

$$\Delta E_{|\overline{\pm 1,n}>}\Big|_{\theta=90^o} = \frac{1}{4}\frac{\omega_Q\omega_2^2}{\omega_Q^2-\omega^2}$$

$$\Delta E_{|0,n>}\Big|_{\theta=90^o} = -\frac{1}{2}\frac{\omega_Q\omega_2^2}{\omega_Q^2-\omega^2} \qquad (4.52)$$

The computed value of $\Delta E/\omega$ for θ approaching 90^o matches very well with the theoretical limit value. When $\theta = 0$, the limit values of ΔE is,

$$\Delta E_{|\overline{\pm 1,n}>}\Big|_{\theta=0} = \Delta E_{|0,n>}\Big|_{\theta=0} = 0. \qquad (4.53)$$

This means that the application of a linearly polarized dressing field along the principal ζ axis won't produce any change.

Energy diagrams for $\theta = 30^o$ and 90^o are drawn on Fig. 4.4 and 4.5 using values of the parameters corresponding to our experimental conditions, $\frac{\omega_Q}{2\pi} = 3.5\ MHz$, $\frac{\omega}{2\pi} = 11.1$

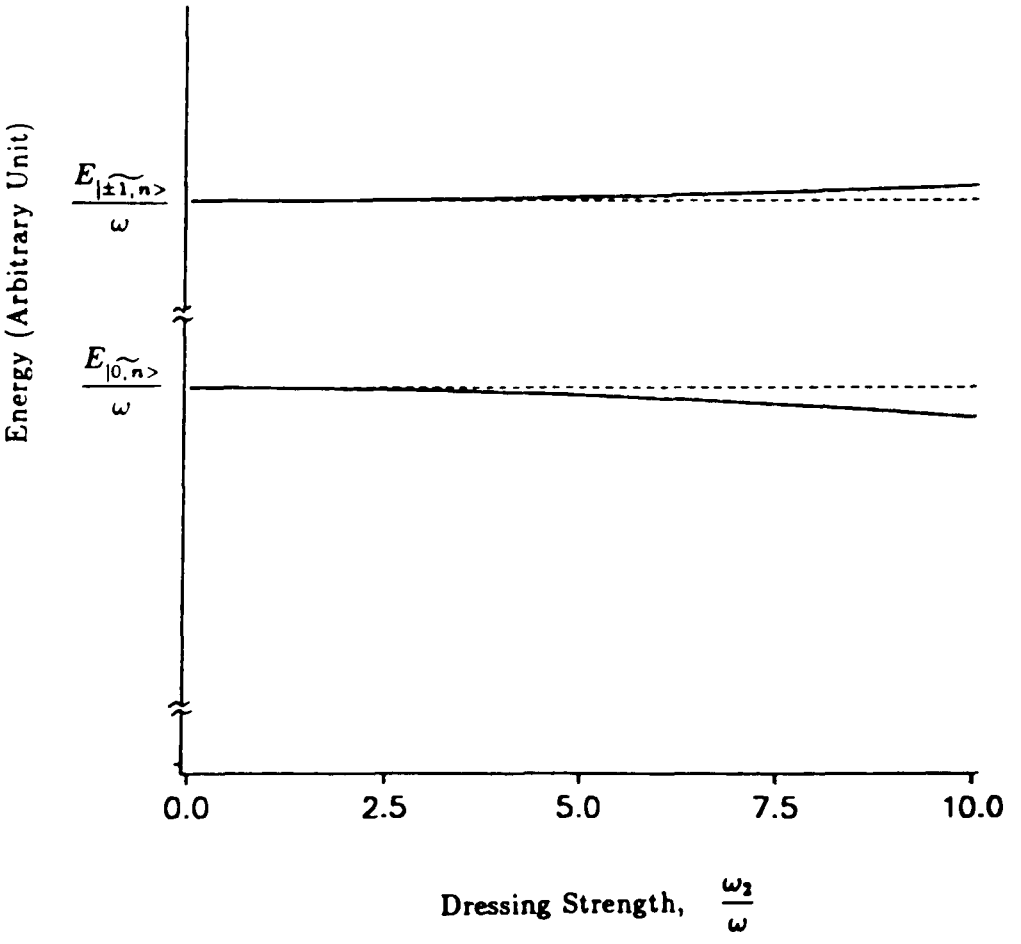

Figure 4.4: Normalized energy of spin $I = 1$ nuclei dressed by linearly polarized photons as function of dressing strength $\frac{\omega_2}{\omega}$ when $\theta = 30°$. The parameters used are $\frac{\omega_Q}{2\pi} = 3.50\ MHz$ and $\frac{\omega}{2\pi} = 11.1\ KHz$. Dashed lines are unperturbed levels of $\mathcal{H}_o$.

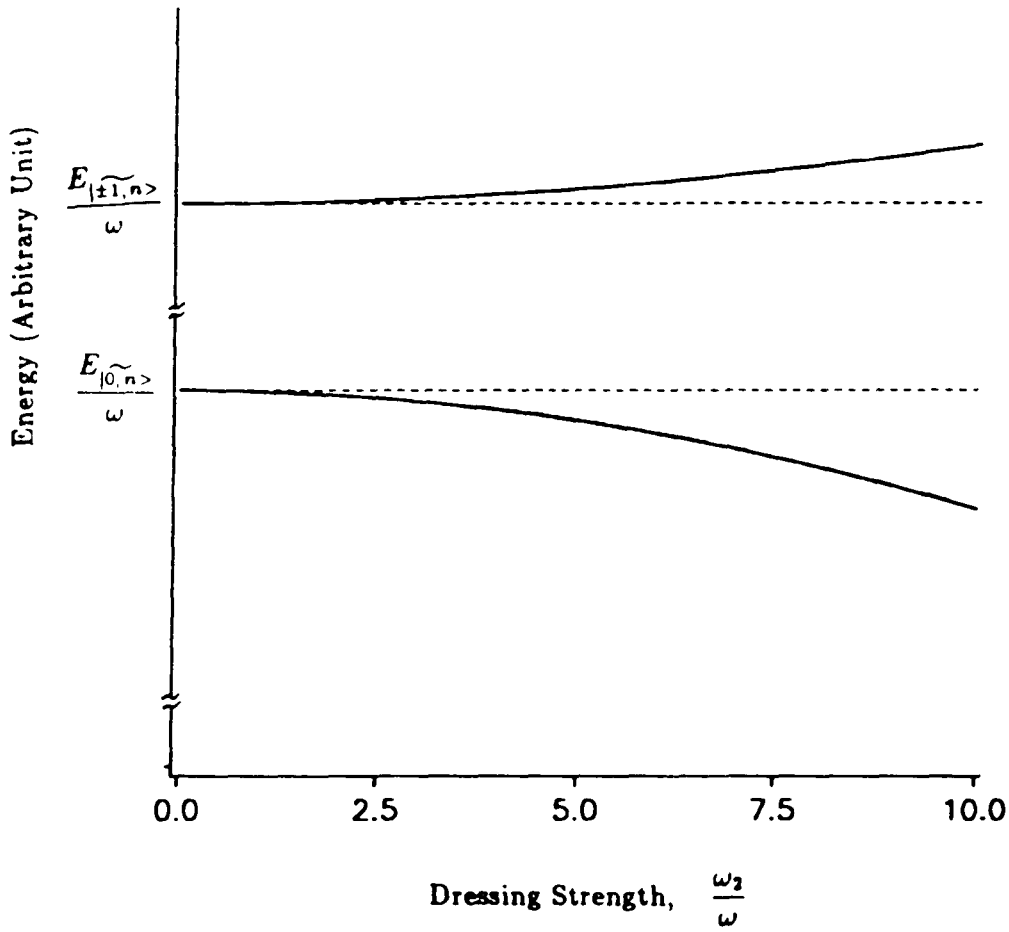

Figure 4.5: Normalized energy of spin $I = 1$ nuclei dressed by linearly polarized photons as function of dressing strength $\frac{\omega_2}{\omega}$ when $\theta = 90°$. The parameters used are $\frac{\omega_Q}{2\pi} = 3.50$ MHz and $\frac{\omega}{2\pi} = 11.1$ KHz. Dashed lines are unperturbed levels of $\mathcal{H}_o$.

kHz. The solid lines are the energy levels of the total hamiltonian $\mathcal{H}$ while the dashed lines are those of $\mathcal{H}_o$. Please note that the ordinate is marked broken in the middle which means it is suppressed a lot to bring the energy levels of $|\widetilde{\pm 1, n}>$ and $|\widetilde{0, n}>$ to the same figure.

Fig. 4.6 depicts the energy levels of $\theta = 0°$, $30°$, $60°$, and $90°$. The outmost solid curves are for $\theta = 90°$, and the two horizontal straight lines are for $\theta = 0°$, which are identical to the energy levels of $\mathcal{H}_o$. The width of this energy spreading due to orientational dependence, can be quantitatively studied through the linewidth of the powder pattern discussed in Chapter 5.

Figs. 4.4 - 4.6 are energy level diagrams of definite photon number n. The complete diagram should consist of many similar manifolds as shown in these figures separated from each other by one photon energy ω. Because $\omega \ll \omega_Q$, there are overlaps between different manifolds.

Because of the energy shift discussed above, the NQR frequency will be shifted. The amount of this shift $\frac{\Delta\omega}{\omega}$ can be obtained by Eqs. 4.46 and 4.47,

$$\frac{\Delta\omega}{\omega} = \frac{\Delta E_{|\widetilde{\pm 1, n}>} - \Delta E_{|0, n>}}{\omega}$$

$$= 3\tan^2\theta \sum_{P=1}^{\infty} \frac{\frac{\omega}{\omega_Q}}{1 - P^2(\frac{\omega}{\omega_Q})^2} P^2 J_P^2(\frac{\omega_2}{\omega}\cos\theta). \qquad (4.54)$$

Eq. 4.54 tells us that the NQR frequency shift due to linearly polarized photon dressing is uniform for the main line and the sidebands. We can picture what happens as follows. Under the influence of linearly polarized photons, besides the appearance of sidebands located symmetrically at both sides of the original NQR line ω_Q, all of the lines, main lines and sidebands, are shifted by the same amount, given by Eq. 4.54. On the other hand, we can see that there is also an orientational dependence to the frequency shift. When powder crystal samples are used, the frequency shift as a function of angle θ will spread out and thus result in a powder pattern. This will be fully discussed in Chapter 5.

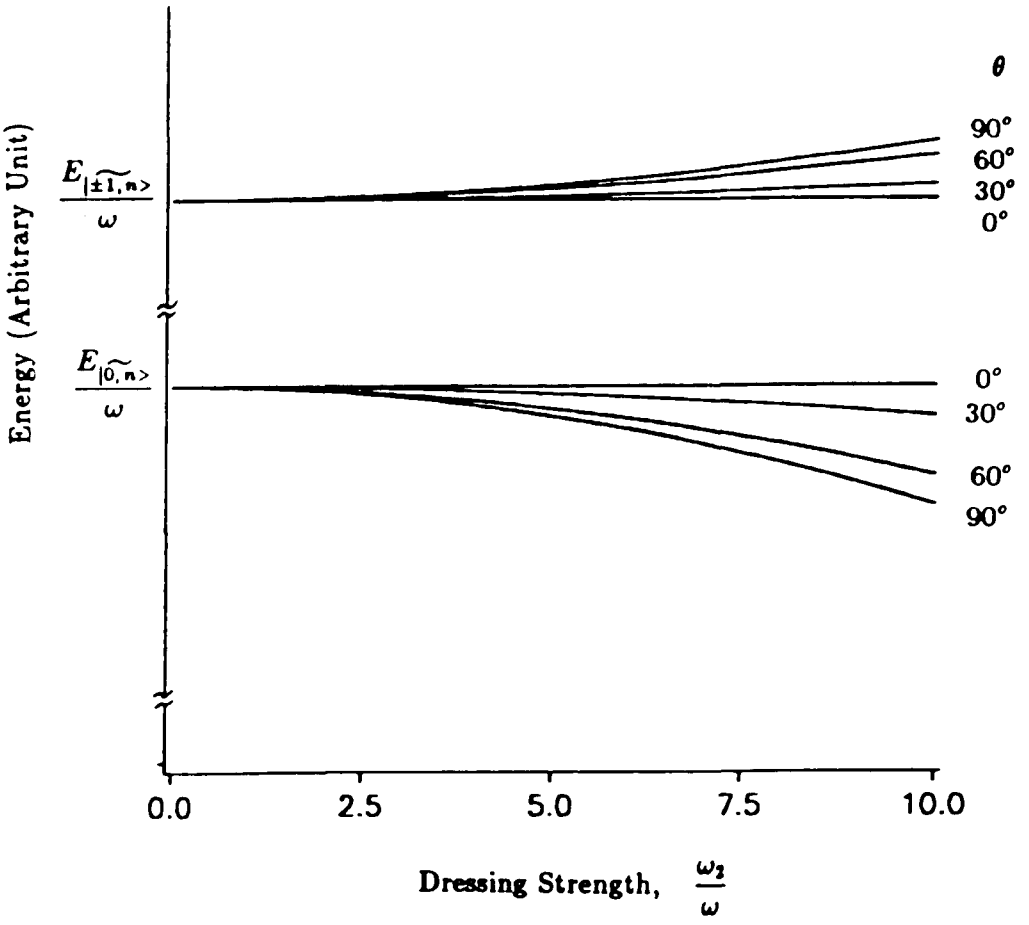

Figure 4.6: Normalized energy of spin $I = 1$ nuclei dressed by linearly polarized photons as function of dressing strength $\frac{\omega_2}{\omega}$ when $\theta = 0°$, $30°$, $60°$, and $90°$. The parameters used are $\frac{\omega_Q}{2\pi} = 3.50\ MHz$ and $\frac{\omega}{2\pi} = 11.1\ KHz$.

4.2 The Case of Circularly Polarized Dressing Field

4.2.1 The Total Hamiltonian

The total hamiltonian of spin $I = 1$ quadrupolar system in the presence of a circularly polarized dressing field has the same form as that for a linearly polarized dressing field, equation 4.1 and 4.2, except that the interaction term V is different.

Assume that the circularly polarized field rotates around the z axis in the laboratory coordinate system xyz, then the magnetic field $\vec{H}_2$ can be expressed as,

$$\vec{H}_2 = H_2(\cos\omega t\ \vec{i} + \sin\omega t\ \vec{j}). \tag{4.55}$$

In the principal $\xi\eta\zeta$ coordinate system of EFG, the dressing field seen by the nuclei is not only a circularly polarized single mode, but a mixture of linearly and circularly polarized coherent mode. The geometrical relation between the laboratory and principal coordinate axes of EFG, for an arbitrary case, is shown in Fig. 4.7, where θ is the angle between the z and ζ axes, ψ is the angle between the intersection line of oxy and $o\xi\eta$ planes and the ox axis, and φ is the angle between that intersection line and the $o\xi$ axis.

Let $\vec{\epsilon}_1$, $\vec{\epsilon}_2$, and $\vec{\epsilon}_3$ be unit vectors along the ξ, η, and ζ axes, respectively. Then the unit vectors $\vec{i}$ and $\vec{j}$ can be expressed in the $\xi\eta\zeta$ system as,

$$\begin{aligned} \vec{i} &= l_1\vec{\epsilon}_1 + l_2\vec{\epsilon}_2 + l_3\vec{\epsilon}_3 \\ \vec{j} &= m_1\vec{\epsilon}_1 + m_2\vec{\epsilon}_2 + m_3\vec{\epsilon}_3 \end{aligned} \tag{4.56}$$

with

$$\begin{aligned} l_1 &= \cos\psi\cos\varphi - \cos\theta\sin\psi\sin\varphi \\ l_2 &= -\cos\psi\sin\varphi - \cos\theta\sin\psi\cos\varphi \\ l_3 &= \sin\theta\sin\psi \\ m_1 &= \sin\psi\cos\varphi + \cos\theta\cos\psi\sin\varphi \\ m_2 &= -\sin\psi\sin\varphi + \cos\theta\cos\psi\cos\varphi \end{aligned}$$

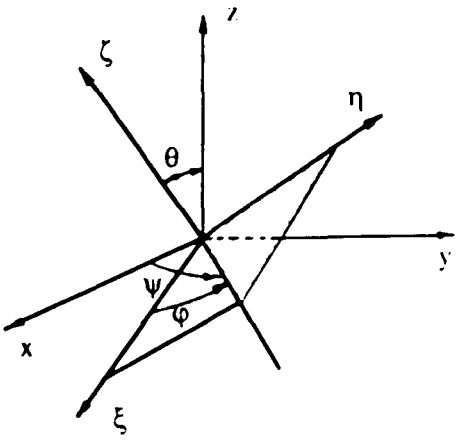

Figure 4.7: Geometrical relation between xyz and $\xi\eta\zeta$ axes.

$$m_3 = -\sin\theta\cos\psi \tag{4.57}$$

Inserting equations 4.56 and 4.57 into 4.55 and simplifying it with trigonometry formulas, we get the expression for $\vec{H}_2$ in the principal axes system of the EFG,

$$\begin{aligned}\vec{H}_2 = H_2\{&\vec{\epsilon}_1[\cos\varphi\cos(\omega t-\psi)+\cos\theta\sin\varphi\sin(\omega t-\psi)]\\ &+\vec{\epsilon}_2[\cos\theta\cos\varphi\sin(\omega t-\psi)-\sin\varphi\cos(\omega t-\psi)]\\ &-\vec{\epsilon}_3\sin\theta\sin(\omega t-\psi)\}\end{aligned} \tag{4.58}$$

All the sites we studied have a symmetric EFG, so that the orientation of ξ and η axes in the plane perpendicular to ζ axis is arbitrary. Thus, limiting ourselves to symmetric EFG systems, we can set the Eulerian angles ψ and φ equal to zero in equation 4.58 without further loss of generality. Then, by a little algebraic rearrangement, $\vec{H}_2$ can be expressed as,

$$\begin{aligned}\vec{H}_2 = H_2\{&-\sin\theta\sin\omega t\vec{\epsilon}_3+\frac{\cos\theta+1}{2}(\cos\omega t\vec{\epsilon}_1+\sin\omega t\vec{\epsilon}_2)\\ &+\frac{\cos\theta-1}{2}(-\cos\omega t\vec{\epsilon}_1+\sin\omega t\vec{\epsilon}_2)\}.\end{aligned} \tag{4.59}$$

In the principal EFG coordinate system, $\vec{H}_2$ is composed of three parts, one linear oscillating along the ζ axis with amplitude $H_2 \sin\theta$, the other two rotating and counter-rotating around the ζ axis with amplitudes $\frac{\cos\theta+1}{2}H_2$ and $\frac{\cos\theta-1}{2}H_2$, respectively. According to Eqns. 3.10 to 3.12 in Chapter 3, the three corresponding terms of the interaction hamiltonian V, labeled as V^o, V^+, and V^- respectively, are expressed below,

$$V = V^0 + V^+ + V^-, \tag{4.60}$$

and,

$$\begin{aligned} V^0 &= \lambda \sin\theta I_\zeta (a^+ + a) \\ V'^+ &= \frac{\lambda}{2}(\cos\theta + 1)(I_+ a + I_- a^+) \\ V^- &= \frac{\lambda}{2}(\cos\theta - 1)(I_+ a^+ + I_- a). \end{aligned} \tag{4.61}$$

4.2.2 Energy Levels of the Dressed Nuclei

The effect of V on the eigenstates of the hamiltonian $\mathcal{H}_o$ is treated in a manner identical to the linear polarization case in section 4.1. First, we use the projection operator P to separate V into V_1 and V_2 two parts acting within and between the manifolds $|\pm 1, n>$ and $|0, n>$ respectively. V_1 has no effect on manifold $|0, n>$, so it remains unchanged under the effect of V_1. In the manifold $|\pm 1, n>$, since $V^{(\pm)}$ has no matrix element between them, V_1 has the form,

$$V_1^{\pm 1} = P_1 V^0 P_1 + P_{-1} V^0 P_{-1}, \tag{4.62}$$

with

$$P_{\pm 1} V^0 P_{\pm 1} = \lambda \sin\theta \sum_{n,n'} |\pm 1, n><\pm 1, n|(a^+ + a)|\pm 1, n'><\pm 1, n'|. \tag{4.63}$$

By using the fictitious spin $\frac{1}{2}$ formulism, $V_1^{\pm 1}$ can be written as,

$$V_1^{\pm 1} = \lambda \sin\theta \sigma_\zeta (a^+ + a) \tag{4.64}$$

with σ_ζ the Pauli matrix in the manifold $|\pm 1, n>$.

The photon part of the hamiltonian $\mathcal{H}'_{\pm 1} = \mathcal{H}_0 + V_1^{\pm 1}$ in it's decomposed form is,

$$\begin{aligned}\mathcal{H}'^{P}_{\pm 1} &= \omega a^+ a \pm \lambda \sin\theta (a^+ + a) \\ &= \omega(a^+ \pm \frac{\lambda}{\omega}\sin\theta)(a \pm \frac{\lambda}{\omega}\sin\theta) - \frac{\lambda^2}{\omega}\sin^2\theta \end{aligned} \tag{4.65}$$

By using the displacement operator as in Eqs. 4.20 and 4.21, the eigenfunction and eigenvalue of hamiltonian $\mathcal{H}'_{\pm 1}$ are deduced to be the following:

$$|\overline{\pm 1, n}> = \exp[\mp\frac{\lambda}{\omega}\sin\theta\,(a^+ - a)]\ \ |\pm 1, n> \tag{4.66}$$

$$\begin{aligned} E'_{\pm 1} &= E_Q^{\pm 1} + n\omega - \frac{\lambda^2}{\omega}\sin^2\theta \\ &\doteq E_Q^{\pm 1} + n\omega \end{aligned} \tag{4.67}$$

The energy levels of $\mathcal{H}'_{\pm 1}$ are approximately equal to those of $\mathcal{H}_o$, but the eigenfunctions are contaminated by different photon numbers. Thus, as in the linear case, in addition to the original NQR line ω_Q, sidebands which differ from ω_Q an amount $(n - n')\omega$ will appear.

The effect of V_2 is treated as a small perturbation on states $|\overline{\pm 1, n}>$ and $|0, n>$ when condition 4.11 is satisfied. The form of V_2 here has many more terms than that of the linear case. By using Eq. 4.27 and the approximate relation 4.36, V_2 can be written as,

$$\begin{aligned} V_2 &= P_1V^+P_0 + P_1V^-P_0 + P_0V^+P_1 + P_0V^-P_1 \\ &\quad + P_{-1}V^+P_0 + P_{-1}V^-P_0 + P_0V^+P_{-1} + P_0V^-P_{-1} \\ &= \frac{\sqrt{2}}{2}\lambda(\cos\theta + 1)\sum_n \sqrt{n}\{|1, n><0, n+1| + |0, n><1, n-1| \\ &\quad + |-1, n><0, n-1| + |0, n><-1, n+1|\} \end{aligned}$$

$$+\frac{\sqrt{2}}{2}\lambda(\cos\theta-1)\sum_n\sqrt{n}\{|\,1,n><0,n-1\,|+|\,0,n><1,n+1\,|$$

$$+|\,-1,n><0,n+1\,|+|\,0,n><-1,n-1\,|\}. \quad (4.68)$$

As noted earlier, V_2 is a hermitian operator. Furthermore, the formulas of energy changes due to second order non-degenerate perturbation are the same as those given in Eq. 4.30. So, by using the same method as was used in the linear case, the matrix elements are calculated and they are listed below:

$$\begin{aligned}
<\overline{1,n}\,|V_2|\,0,n'> &= <0,n\,|V_2|\overline{-1,n'}> \\
&= -\frac{\sqrt{2}}{2}\omega\cot\theta(n-n')J_{n-n'}(x_4) \\
&\quad +\frac{\sqrt{2}}{4}\omega_2\{J_{n-n'+1}(x_4)-J_{n-n'-1}(x_4)\} \qquad (4.69)\\
<\overline{-1,n}\,|V_2|\,0,n'> &= <0,n\,|V_2|\overline{1,n'}> \\
&= \frac{\sqrt{2}}{2}\omega\cot\theta(n-n')J_{n-n'}(x_3) \\
&\quad +\frac{\sqrt{2}}{4}\omega_2\{J_{n-n'-1}(x_3)-J_{n-n'+1}(x_3)\} \qquad (4.70)
\end{aligned}$$

where

$$x_3=\frac{\omega_2}{\omega}\sin\theta=-x_4. \qquad (4.71)$$

Let $n-n'=P$, and use Eq. 4.42 to change the argument of the Bessel function x_4 into x_3, and square these matrix elements, we have,

$$\begin{aligned}
|<\overline{1,n}\,|V_2|\,0,n'>|^2 &= |<0,n\,|V_2|\overline{-1,n'}>|^2 \\
&= \frac{1}{2}\omega^2\cot^2\theta P^2J_P^2(x_3)+\frac{1}{8}\omega_2^2\{J_{P+1}(x_3)-J_{P-1}(x_3)\}^2 \\
&\quad -\frac{1}{2}\omega\omega_2\cot\theta PJ_P(x_3)\{J_{P-1}(x_3)-J_{P+1}(x_3)\} \qquad (4.72)
\end{aligned}$$

$$|<\overline{-1,n}|V_2|0,n'>|^2 = |<0,n|V_2|\overline{1,n'}>|^2$$

$$= \frac{1}{2}\omega^2\cot^2\theta P^2 J_P^2(x_3) + \frac{1}{8}\omega_2^2\{J_{P+1}(x_3) - J_{P-1}(x_3)\}^2$$

$$+\frac{1}{2}\omega\omega_2\cot\theta P J_P(x_3)\{J_{P-1}(x_3) - J_{P+1}(x_3)\} \qquad (4.73)$$

Note that the above two expressions are almost identical except the third term has the opposite sign, so that after taking into account the perturbation of V_2, the degeneracy of states $|\overline{\pm 1,n}>$ will be removed. By the same considerations as those of the linear case when changing the summation over n' into that of over P, and analyzing the behavior of each term in Eqs. 4.72 and 4.73 when P is replaced by $-P$, the energy change due to V_2 can be expressed as follows,

$$\Delta E_{|\overline{\pm 1,n}>} = \frac{\omega_2^2}{2\omega_Q}J_1^2(x_3)$$

$$+\sum_{P=1}^{\infty}\frac{\omega_Q}{\omega_Q^2 - P^2\omega^2}\left\{\omega^2\cot^2\theta P^2 J_P^2(x_3)\right.$$

$$\left.+\frac{1}{4}\omega_2^2[J_{P+1}(x_3) - J_{P-1}(x_3)]^2\right\}$$

$$\pm\sum_{P=1}^{\infty}\frac{\omega^2\omega_2}{\omega_Q^2 - P^2\omega^2}\cot\theta P^2 J_P(x_3)[J_{P-1}(x_3) - J_{P+1}(x_3)] \qquad (4.74)$$

and

$$\Delta E_{|0,n>} = -\frac{\omega_2^2}{\omega_Q}J_1^2(x_3) - \sum_{P=1}^{\infty}\frac{2\omega_Q}{\omega_Q^2 - P^2\omega^2}\left\{\omega^2\cot^2\theta P^2 J_P^2(x_3)\right.$$

$$\left.+\frac{1}{4}\omega_2^2[J_{P-1}(x_3) - J_{P+1}(x_3)]^2\right\}. \qquad (4.75)$$

4.2.3 Energy Level Diagrams of the Dressed Nuclei

Finally, we are able to express the energy levels of the total hamiltonian $\mathcal{H}$ by taking the sum of E' and ΔE. The dimensionless expressions of the energies are given below,

$$\frac{E_{|\overline{\pm 1,n}>}}{\omega} = \frac{1}{3}\frac{\omega_Q}{\omega} + n + \frac{1}{2}\frac{\omega_2}{\omega_Q}\frac{\omega_2}{\omega}J_1^2(x_3)$$

$$+\sum_{P=1}^{\infty}\left\{\frac{\frac{\omega}{\omega_Q}}{1-P^2(\frac{\omega}{\omega_Q})^2}\cot^2\theta P^2 J_P^2(x_3)\right.$$

$$\left.+\frac{1}{4}\frac{\frac{\omega_2}{\omega_Q}\frac{\omega_2}{\omega}}{1-P^2(\frac{\omega}{\omega_Q})^2}[J_{P+1}(x_3)-J_{P-1}(x_3)]^2\right\}$$

$$\pm\sum_{P=1}^{\infty}\frac{\frac{\omega}{\omega_Q}\frac{\omega_2}{\omega}}{1-P^2(\frac{\omega}{\omega_Q})^2}\cot\theta P^2 J_P(x_3)[J_{P-1}(x_3)-J_{P+1}(x_3)] \quad (4.76)$$

$$\frac{E_{|\widetilde{0,n}>}}{\omega} = -\frac{2}{3}\frac{\omega_Q}{\omega}+n-\frac{\omega_2}{\omega_Q}\frac{\omega_2}{\omega}J_1^2(x_3)$$

$$-\sum_{P=1}^{\infty}\left\{\frac{2\frac{\omega}{\omega_Q}}{1-P^2(\frac{\omega}{\omega_Q})^2}\cot^2\theta P^2 J_P^2(x_3)\right.$$

$$\left.+\frac{1}{2}\frac{\frac{\omega_2}{\omega_Q}\frac{\omega_2}{\omega}}{1-P^2(\frac{\omega}{\omega_Q})^2}[J_{P-1}(x_3)-J_{P+1}(x_3)]^2\right\} \quad (4.77)$$

Expressions 4.76 and 4.77 are plotted for $\frac{E}{\omega}$ versus dressing strength $\frac{\omega_2}{\omega}$ by numerical computation. The computational program about the summation over P is set in the same manner as that described in the linear polarization case. Here, when $\theta = 0°$ the energy values are uncomputable, equal to $0\cdot\infty$. The limit values of ΔE at $\theta = 0°$ are calculated theoretically. They are,

$$\Delta E_{|\widetilde{\pm 1,n}>}\Big|_{\theta=0°} = \frac{1}{2}\frac{\omega_2^2}{\omega_Q^2-\omega^2}(\omega_Q\pm\omega)$$

$$\Delta E_{|0,n>}\Big|_{\theta=0°} = -\frac{\omega_Q\omega_2^2}{\omega_Q^2-\omega^2} \quad (4.78)$$

The computed value of ΔE when θ approaches zero matches the theoretical limit value very well. When $\theta = 90°$, only the first and third terms of ΔE in Eqs. 4.74 and 4.75 make a contribution.

Figs. 4.8 and 4.9 depict the energy levels of spin $I = 1$ nuclei dressed by a circularly polarized field when $\theta = 0°$ and $90°$ respectively. The parameters ω_Q and ω are taken to be the same values as those of linear dressing. The solid lines are the energy levels of total hamiltonian $\mathcal{H}$ while the dashed lines are those of $\mathcal{H}_o$. The top solid line, which

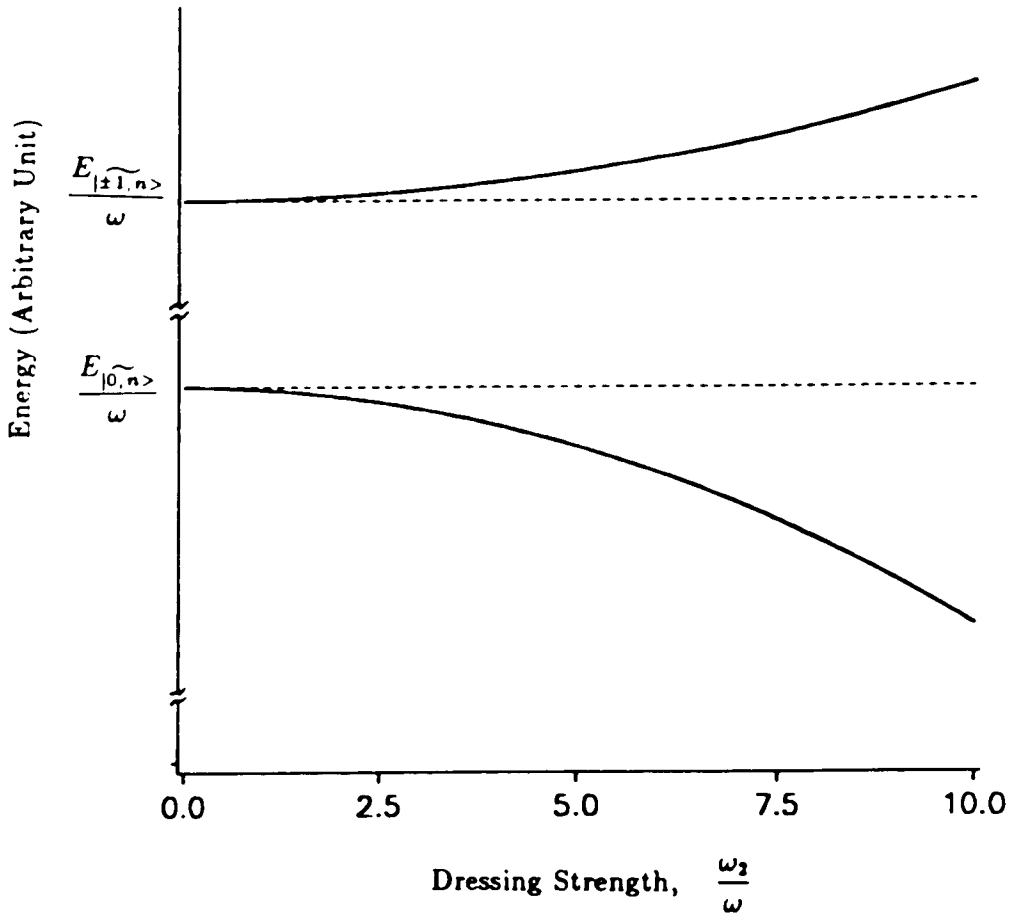

Figure 4.8: Normalized energy of spin $I = 1$ nuclei dressed by circularly polarized photons as function of dressing strength $\frac{\omega_2}{\omega}$ when $\theta = 0°$, The parameters used are $\frac{\omega_Q}{2\pi} = 3.50\ MHz$ and $\frac{\omega}{2\pi} = 11.1\ KHz$. Dashed lines are unperturbed levels of $\mathcal{H}_o$

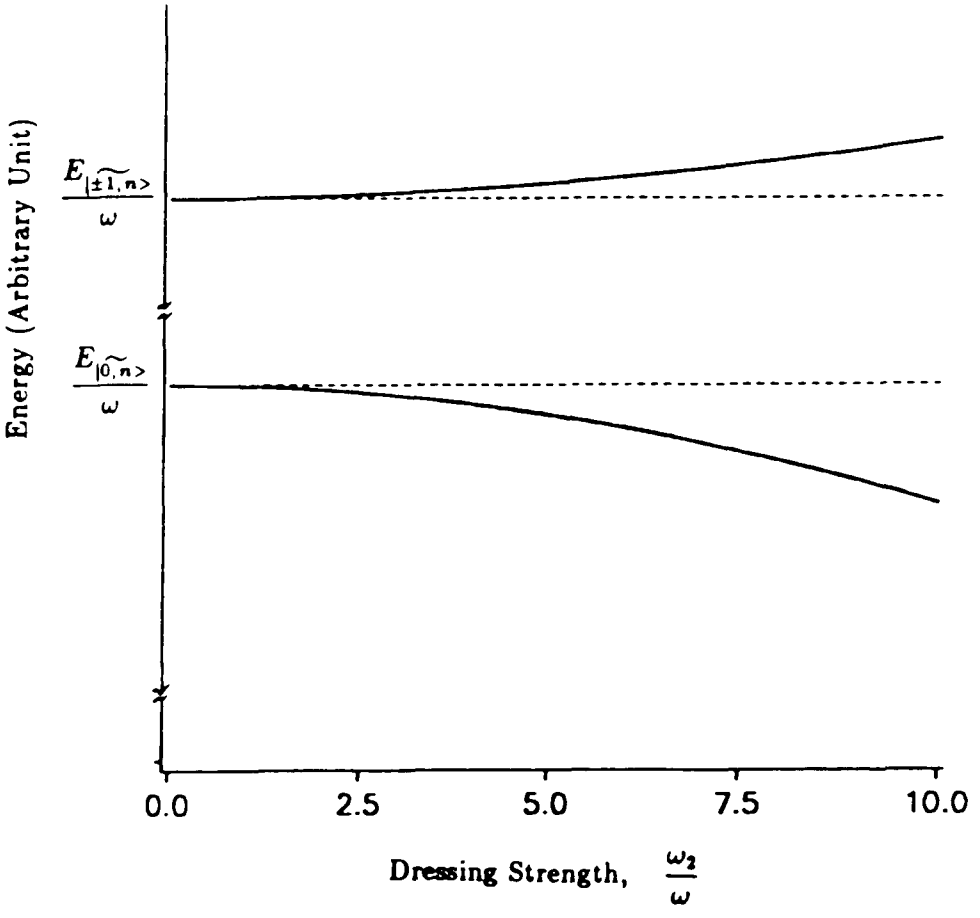

Figure 4.9: Normalized energy of spin $I = 1$ nuclei dressed by circularly polarized photons as a function of dressing strength $\frac{\omega_2}{\omega}$ when $\theta = 90°$, The parameters used are $\frac{\omega_Q}{2\pi} = 3.50\ MHz$ and $\frac{\omega}{2\pi} = 11.1\ KHz$. Dashed lines are the unperturbed levels of $\mathcal{H}_o$

stands for states $|\widetilde{\pm 1, n}>$, is a single line instead of two lines as predicted by Eq. 4.74, because the energy difference between these two states is too small to be shown on the same scale. It has been numerically computed that this energy difference divided by 2π is only 0.74 Hz for the dressing strength $\frac{\omega_2}{\omega} = 3.0$, and 2.95 Hz for $\frac{\omega_2}{\omega} = 6.0$. Compared to the NQR linewidth, $\Delta\omega_Q$, such a small difference is completely negligible. Although the degeneracy between states $|\overline{\pm 1, n}>$ is theoretically removed by the effect of V_2, the numerical analysis tells us that these states are still nearly degenerate.

Fig. 4.10 depicts the energy levels of $\theta = 0°$, $30°$, $60°$, and $90°$. The outmost solid lines are for $\theta = 0°$, the line gets closer to middle (that is to say, getting flatter), when the θ value gets bigger. The width of this spreading can be seen in the width of the transition powder patterns, which are discussed in Chapter 5.

The energy diagrams of linearly and circularly polarized dressing fields do not show a big difference. Compared to the energy levels of $\mathcal{H}_o$, they both curve up or down as the dressing strength increases, but remain two energy levels. i.e., the diagrams do not show any energy level crossings or anticrossings. Contrast this to the case of half integer spins, for example, spin $I = \frac{3}{2}$, as studied by Ito and Hashi [28, 30, 31]. For a circularly polarized dressing field, under the effect of V_1, the degeneracy of $|\pm\frac{1}{2}, n>$ states is removed and exhibits an infinite number of level crossings, then the effect of the perturbation V_2 produces anticrossing and shifted crossings. Due to the appreciable change of the states $|\pm\frac{1}{2}, n>$, the NQR lines not only exhibit a shift, but also a splitting, the original single NQR transition from $|\pm\frac{3}{2}, n>$ to $|\pm\frac{1}{2}, n>$ splits into two lines at anticrossings. This difference of the energy level diagrams between spin I equals 1 and $\frac{3}{2}$ can be generalized to any integer or half integer spin. Whether the degeneracy of pure quadrupole energy levels can be lifted or not, depends on whether V_1 has nonzero off-diagonal matrix elements within a manifold. The expression of V for a circularly polarized dressing field in Eq. 4.61 can only join states with $\Delta m_\zeta = 0$ or ± 1, so that only the degenerate states $|\pm\frac{1}{2}, n>$ can possibly be coupled by V, all of the other degenerate states $|\pm m_\zeta, n>$ with $|m_\zeta|$ bigger than $\frac{1}{2}$ are not coupled by V. That is the root of the different response to the photon dressing between integer and

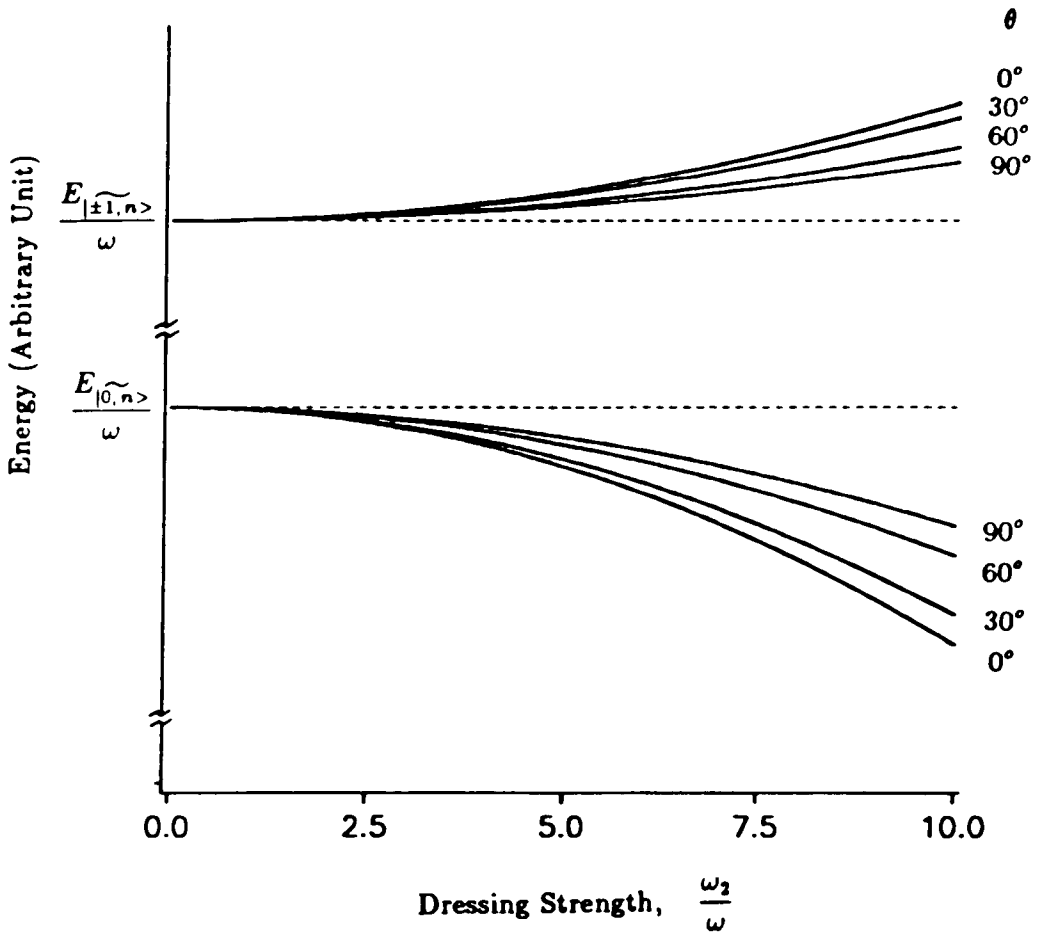

Figure 4.10: Normalized energy of spin $I = 1$ nuclei dressed by circularly polarized photons as a function of dressing strength $\frac{\omega_2}{\omega}$ when $\theta = 0°$, $\theta = 30°$, $\theta = 60°$, and $90°$. The parameters used are $\frac{\omega_Q}{2\pi} = 3.50\ MHz$ and $\frac{\omega}{2\pi} = 11.1\ KHz$. Dashed lines are unperturbed levels of $\mathcal{H}_o$

half integer spins. It can be predicted that, the various interesting phenomena related to crossings [48] and anticrossings [49] can be observed in half integer spin dressed by circularly polarized photons, but not in integer spin nuclei. For a linearly polarized dressing field, although V_1 has nonzero off-diagonal matrix elements between $|\pm\frac{1}{2}, n>$, these off diagonal elements are equal due to the nature of the interaction V in Eq. 4.9. Symmetric matrices can always be diagonized with their orthonormal eigenvectors. As a result, the effect of V_1 in the presence of a linearly polarized dressing field does not produce any crossings, and the energy level diagrams of half integer or integer spin in the presence of linearly polarized photons do not exhibit any real difference. However, when an additional weak static magnetic field is applied to the nuclei, the zero*th* order Zeeman splitting of the $|\pm\frac{1}{2}, n>$ states is modified by the Bessel function J_0, but the $|\pm\frac{3}{2}, n>$ states are not [31, 45]. This difference arises also because the interaction between the static field and the nuclei can only joint states with $\Delta m_\zeta = 0$ or ± 1, so that the states $|\pm\frac{3}{2}, n>$ are not coupled by this interaction. For the same reason, we can predict that the zero*th* order Zeeman splitting of integer spins in the presence of linearly polarized dressing field will not be modified by Bessel function at all.

Although the energy level diagram of spin $I = 1$ nuclei in the presence of linearly or circularly polarized photon do not show real differences, the amount of the energy shift due to these two different polarized photons is different. Figs. 4.4 to 4.6 for the linear case and Figs 4.8 to 4.10 for the circular case are plotted on the same scale. The maximum (or minimum) shift for the linear case happens when $\theta = 90^o$ (or 0^o), while for circular case, the maximum (or minimum) shift happens when $\theta = 0^o$ (or 90^o). The maximum shift for the circular case is about twice as much as that of the linear case, as seen from Eqns 4.52 and 4.78, and the minimum shift of the circular case is about the same as the maximum shift of the linear case, as shown in the figures.

Due to the effect of V_2, according to second order non-degenerate perturbation theory, the state $|\widetilde{1, n}>$ of the total hamiltonian $\mathcal{H}$ is now contaminated with the state $|\overline{1, n}>$ and $|0, n>$; state $|\widetilde{-1, n}>$ is contaminated with $|\overline{-1, n}>$ and $|0, n>$; and state $|\widetilde{0, n}>$ is the mixture of states $|\overline{\pm 1, n}>$ and $|0, n>$. Therefore, theoretically,

transitions between all three states of $\mathcal{H}$ are possible and three NQR lines are expected in each band (meaning each $n - n'$ value). However, since the energy difference between the states $|\pm\widetilde{1, n}>$ is extremely small, a few Hz for a substantial dressing strength, the transition frequency between $|\pm\widetilde{1, n}>$ is neglected. The observable NQR line is from $|\pm\widetilde{1, n}>$ to $|\widetilde{0, n}>$, labeled as $\omega_{\pm}$. The frequency shift between $\omega_{\pm}$ and ω_Q, labeled as $\Delta\omega_{\pm}$, is expressed in the normalized form as below,

$$\begin{aligned}\frac{\Delta\omega_{\pm}}{\omega} &= \frac{3}{2}\frac{\omega_2^2}{\omega_Q\omega}J_1^2(x_3) + \sum_{P=1}^{\infty}\left\{\frac{\omega}{\omega_Q}\cot^2\theta P^2 J_P^2(x_3)\right. \\ &\quad \left. + \frac{1}{4}\frac{\omega_2^2}{\omega_Q\omega}[J_{P-1}(x_3) - J_{P+1}(x_3)]^2\right\} \\ &\quad \pm \sum_{P=1}^{\infty}\frac{\frac{\omega\omega_2^2}{\omega_Q^2}}{1 - P^2(\frac{\omega}{\omega_Q})^2}\cot\theta P^2 J_P(x_3)[J_{P-1}(x_3) - J_{P+1}(x_3)] \qquad (4.79)\end{aligned}$$

As discussed before, the difference between $\Delta\omega_+$ and $\Delta\omega_-$ is very small.

The frequency shift $\Delta\omega_{\pm 1}$ is also a function of angle θ, when powder crystal or polycrystalline samples are used, the lines are broadened and form a powder pattern. This will be discussed in the following chapter 5.

Chapter 5

Powder Patterns of NQR Lines Due to Photon Dressing

5.1 General Powder Pattern Formula

The NQR frequency shifts due to an applied non-resonant oscillating or rotating field, Eqs. 4.54 and 4.79 are functions of θ, the angle between the principal EFG ζ axis and the oscillating or rotating field. When the specimen under study is polycrystalline, the random distribution of orientations gives rise to a continuous distribution of frequencies, thus the resulting resonance is in a powder pattern.

Let

$$\mu \equiv \cos\theta \tag{5.1}$$

and $P(\mu)d\mu$ be the probability that μ lines between μ to $\mu + d\mu$. Since μ is a periodical continuous function of angle θ, the integral of this probability over it's whole range of contribution should be equal to unity. Because all orientations are equally likely, no particular direction has preference, $P(\mu)$ should be a constant. So we have,

$$\begin{aligned} \int_{-1}^{1} P(\mu)d\mu &= P(\mu)\int_{-1}^{1} d\mu \\ \int_{-1}^{1} P(\mu)d\mu &= P(\mu)\int_{-1}^{1} d\mu \\ &= 1 \end{aligned} \tag{5.2}$$

From Eq. 5.2, the constant $P(\mu)$ is deduced immediately,

$$P(\mu) = \frac{1}{2} \tag{5.3}$$

Let $g(\nu)$ be the normalized shape function of an NQR line. The intensity of a resonant

line between frequencies ν and $\nu + d\nu$, is given by $g(\nu)d\nu$, and is proportional to the number of nuclei which contribute to frequencies between ν and $\nu + d\nu$, that is to say, proportional to the probability that μ lines between μ and $\mu + d\mu$. Then we can write,

$$g(\nu)d\nu = 2P(\mu)d\mu \tag{5.4}$$

where the proportionality constant has been set to be one, and the factor of two appears in the equation because $+\mu$ and $-\mu$ correspond to the same frequency ω in equations 4.54 and 4.79. Inserting the constant $P(\mu)$ into 5.4, we have the expression for the shape function,

$$g(\nu) = \left|\frac{d\mu}{d\nu}\right|. \tag{5.5}$$

The absolute value has been taken because the intensity of a resonant line must be positive.

Applying Eq. 5.5 to the cases of oscillating and rotating dressing field and plotting the powder patterns, are the subjects of the following sections.

5.2 Powder Pattern of Spin $I = 1$ NQR Lines in the Presence of a Linearly Polarized Dressing Field

The NQR frequency shift due to linearly polarized photon dressing, Eq. 4.54, is expressed by the quantity $\frac{\Delta\omega}{\omega}$, where $\Delta\omega = \Delta(2\pi\nu)$, is the change in the NQR circular frequency, and ω is the circular frequency of the photon, which is a constant. The actual NQR frequency is the sum of the nude NQR circular frequency ω_Q, which has a certain value for certain nuclei, plus the frequency change $\Delta\omega$. The term ω_Q will not contribute anything to the shape function $g(\nu)$ because it is not a function of angle θ, all of the contribution to the line shape comes from the term $\Delta\omega$. If we let $z = \frac{\Delta\omega}{\omega}$, then the shape function $g(\nu)$ can be expressed by

$$g(z) = \left|\frac{d\mu}{dz}\right| \tag{5.6}$$

where nothing has been changed except the variable ν to z. Eq. 5.6 is equivalent to Eq. 5.5 in our case.

Let

$$A(P,\omega,\omega_Q) = \frac{3\frac{\omega}{\omega_Q}}{1 - P^2(\frac{\omega}{\omega_Q})^2} P^2 \tag{5.7}$$

and by Eq. 5.1 we have

$$\tan^2\theta = \frac{1-\mu^2}{\mu^2} \tag{5.8}$$

Continuing the use of x_1 to represent the argument $\frac{\omega_2}{\omega}\mu$ of the Bessel function, we rewrite Eq. 4.54 as follows,

$$z = \frac{1-\mu^2}{\mu^2} \sum_{P=1}^{\infty} A J_p^2(x_1). \tag{5.9}$$

Now we need to obtain the total differential dz with respect to $d\mu$. With the help of the following relation of Bessel functions,

$$\frac{d}{dx} J_P(x) = \frac{1}{2}[J_{P-1}(x) - J_{P+1}(x)] \tag{5.10}$$

we find the derivative of Eq. 5.9 by parts. We have,

$$dz = \left\{ -\frac{2}{\mu^3} \sum_{P=1}^{\infty} A J_P^2(x_1) + \frac{1-\mu^2}{\mu^2} \sum_{P=1}^{\infty} A J_P(x_1)[J_{P-1}(x_1) - J_{P+1}(x_1)] \frac{\omega_2}{\omega} \right\} d\mu. \tag{5.11}$$

Now, with the help of another Bessel function relation,

$$\frac{2J_P(x)}{x} = \frac{1}{P}[J_{P-1}(x) + J_{P+1}(x)], \tag{5.12}$$

Eq. 5.11 can be rewritten in a simpler form,

$$dz = \frac{\omega_2}{\omega} \sum_{P=1}^{\infty} A J_P(x_1) \left\{ \left(\frac{1-\frac{1}{P}}{\mu^2} - 1 \right) J_{P-1}(x_1) - \left(\frac{1+\frac{1}{P}}{\mu^2} - 1 \right) J_{P+1}(x_1) \right\} d\mu \tag{5.13}$$

Finally, from equations 5.6 and 5.13, we obtain the expression for the shape function for a linearly polarized dressing field,

$$g(z) = \frac{\frac{\omega}{\omega_2}}{\left| \sum_{P=1}^{\infty} \frac{3\frac{\omega}{\omega_Q}}{1-P^2(\frac{\omega}{\omega_Q})^2} P^2 J_P(x_1) \left[\left(\frac{1-\frac{1}{\mu^2}}{\mu^2} - 1 \right) J_{P-1}(x_1) - \left(\frac{1+\frac{1}{\mu^2}}{\mu^2} - 1 \right) J_{P+1}(x_1) \right] \right|} \tag{5.14}$$

Note that the shape function 5.14 only considers the broadening due to non-resonant photon dressing, and does not include any other broadening mechanism.

The shape function $g(z)$ is plotted as function of z by numerical computation. Figs. 5.1 to 5.3 depict lineshapes of $I = 1$ nuclei dressed by linearly polarized photons when $\frac{\omega_2}{\omega} = 0.66$, 2.0, and 4.0 respectively. The parameters used are $\frac{\omega_Q}{2\pi} = 3.5$ MHz, $\frac{\omega}{2\pi} = 11.1$ kHz. The abscissa of the graph is expressed as the dimensionless quantity $\frac{\Delta\omega}{\omega}$. To find out the value of the frequency shift at a specific position on the graph, simply multiply the abscissa value of that position by 11.1 kHz, which gives the frequency shift $\frac{\Delta\omega}{2\pi}$ in units of kHz. The lineshapes which are represented by solid curves in the figures have intensity distribution in the frequency domain. $\Delta\omega$ changes from zero to its maximum shift, corresponding to θ going from zero to 90°. The value of maximum frequency shift is also the width of the powder pattern. The intensity of the line at $\theta = 90°$ diverges. The dashed vertical line in the figure stands for the asymptote when θ approaches to 90°. For a single crystal, where θ has a fixed value, we expect to get a sharp line with no width. The actual θ value for a single crystal depends on what sample is studied and under what geometrical arrangements the experiment is performed. As an example, consider θ equal to 45°. The position of its infinitely sharp line is marked on Fig. 5.1 to 5.3 as X. We can see that when a powdered sample is under study, the peak of the NQR line is shifted more, compared to the single crystal case, and the line is much more broadened. Note that, for the special case where the linearly polarized dressing field oscillates along the ζ axis of the single crystal, $\theta = 0$, and there will be neither a shift nor a broadening. The photon dressing has no effect

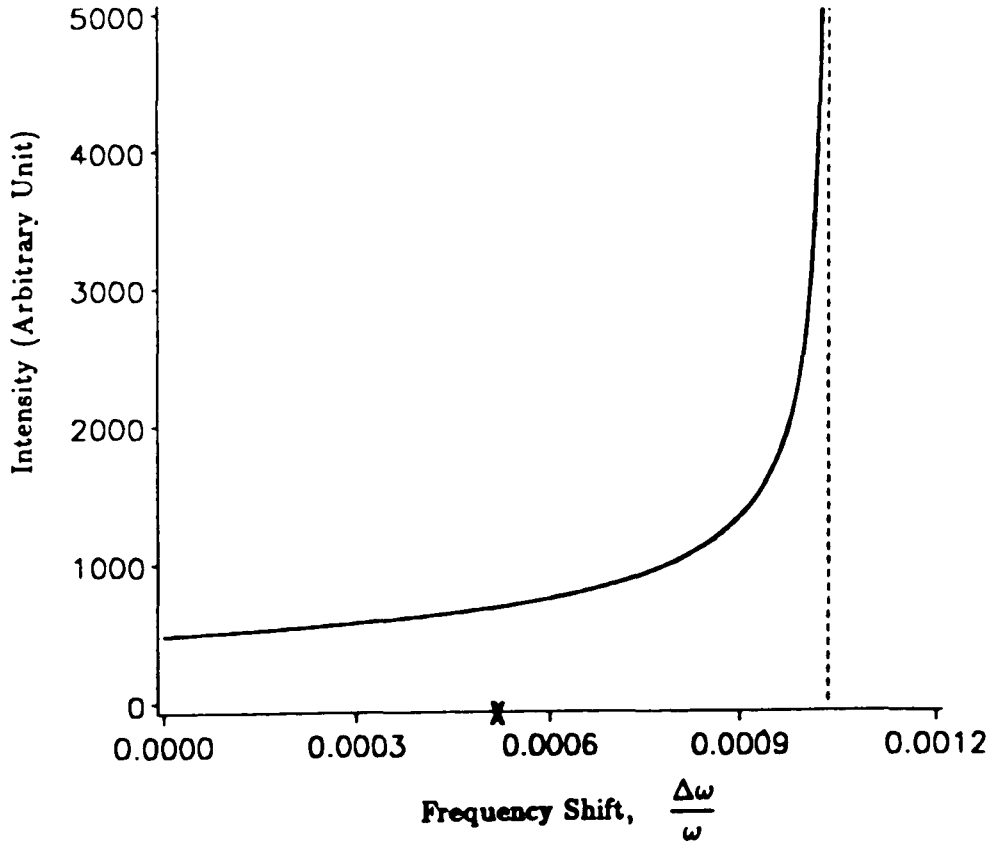

Figure 5.1: Powder pattern for a spin $I = 1$ NQR line in the presence of linearly polarized photons when $\frac{\omega_2}{\omega} = 0.66$. The parameters used are $\frac{\omega_Q}{2\pi} = 3.5\ MHz$ and $\frac{\omega}{2\pi} = 11.1\ kHz$. "$X$" indicates the frequency shift $\frac{\Delta\omega}{2\pi}$ of $5.75\ Hz$ when $\theta = 45°$. The peak shift at $\theta = 90°$ is $11.50\ Hz$.

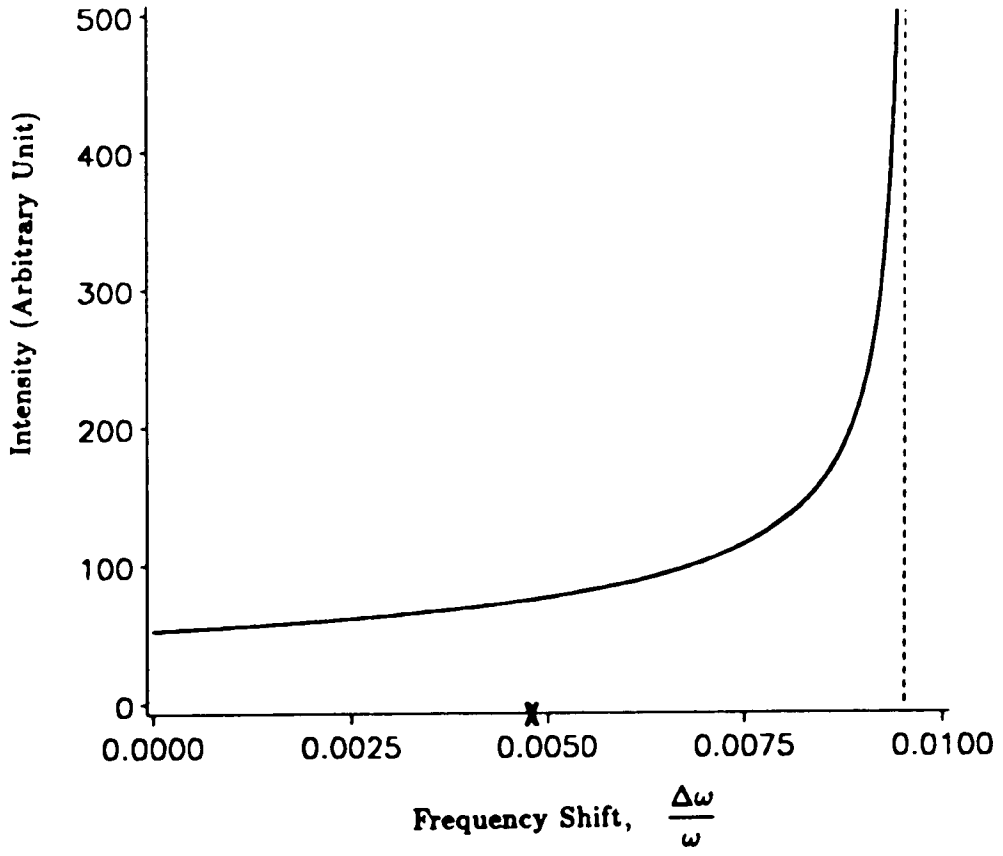

Figure 5.2: Powder pattern for a spin $I = 1$ NQR line in the presence of linearly polarized photons when $\frac{\omega_Q}{\omega} = 2.0$. The parameters used are $\frac{\omega_Q}{2\pi} = 3.5\ MHz$ and $\frac{\omega}{2\pi} = 11.1\ kHz$. "$X$" indicates the frequency shift $\frac{\Delta\omega}{2\pi}$ of 52.80 Hz when $\theta = 45°$. The peak shift at $\theta = 90°$ is 105.61 Hz.

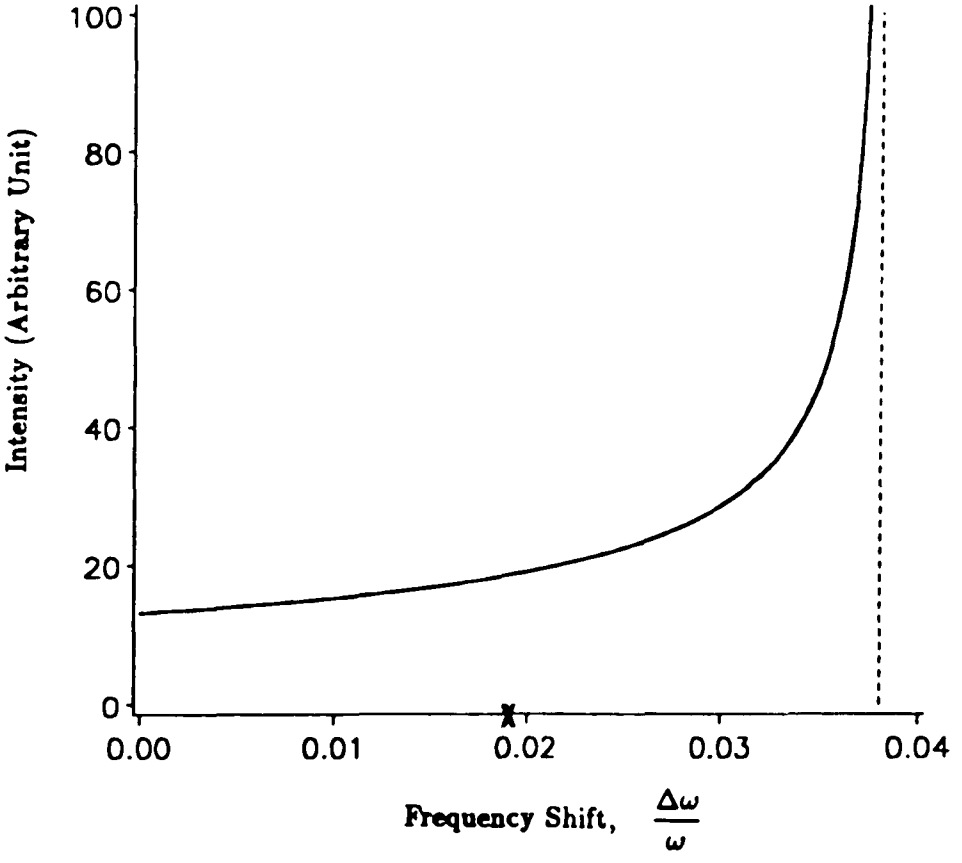

Figure 5.3: Powder pattern for a spin $I = 1$ NQR line in the presence of linearly polarized photons when $\frac{\omega_2}{\omega} = 4.0$. The parameters used are $\frac{\omega_Q}{2\pi} = 3.5\ MHz$ and $\frac{\omega}{2\pi} = 11.1\ kHz$. "$X$" indicates the frequency shift $\frac{\Delta\omega}{2\pi}$ of 211.23 Hz when $\theta = 45^o$. The peak shift at $\theta = 90^o$ is 422.47 Hz.

in single crystals when θ equals zero.

As the dressing strength $\frac{\omega_2}{\omega}$ gets larger, the peak of the lineshape is shifted more, but the lineshape does not get further broadened. This is because the shape function is normalized, so that the area under the lineshape is unity. For large dressing strength, the peak is shifted more, so that the intensity away from the peak becomes smaller, which acts like background noise and does not really effect the linewidth. This feature can be seen clearly in Fig. 5.4, which depicts the lineshapes of dressing strength $\frac{\omega_2}{\omega}$ = 1.0, 2.0, 3.0, and 6.0 in the same scale. The peak shift is $\frac{\Delta\omega}{2\pi}$, therefore, the width of the lines for these dressing strength are equal to 26.41 Hz, 105.61 Hz, 245.77 Hz, and 947.9 Hz, respectively, but the intensity of the lineshapes away from $\theta = 90^{\circ}$ drops to smaller and smaller values as $\frac{\omega_2}{\omega}$ gets bigger.

Fig. 5.1 depicts the lineshape when $\frac{\omega_2}{\omega}$ = 0.66. The particular value 0.66 is the maximum dressing strength that we reached in our experiment. Due to the limited power of the amplifier used in the experiment, the maximum dressing field we can reach was 24 G, which corresponds to $\frac{\omega_2}{\omega}$ = 0.66 for ^{14}N with a dressing frequency $\frac{\omega}{2\pi}$ = 11.1 kHz. In Fig. 5.1 the peak shift $\frac{\Delta\omega}{2\pi}$ = 11.50 Hz, which is not observable in the experiment. In our experiment, as detailed in Chapter 7, no data were taken for a linearly polarized field. However, we did look for the effect of an oscillating field by applying only one channel of current: no shift was observed even with maximum power, but side bands did appear. These results are consistent with the theory developed here.

5.3 Powder Pattern of Spin I = 1 NQR Line in the Presence of a Circularly Polarized Dressing Field

Now we apply equation 5.5 to the case of a circularly polarized dressing field.

Let

$$Z_{\pm} = \frac{\Delta\omega_{\pm}}{\omega}, \tag{5.15}$$

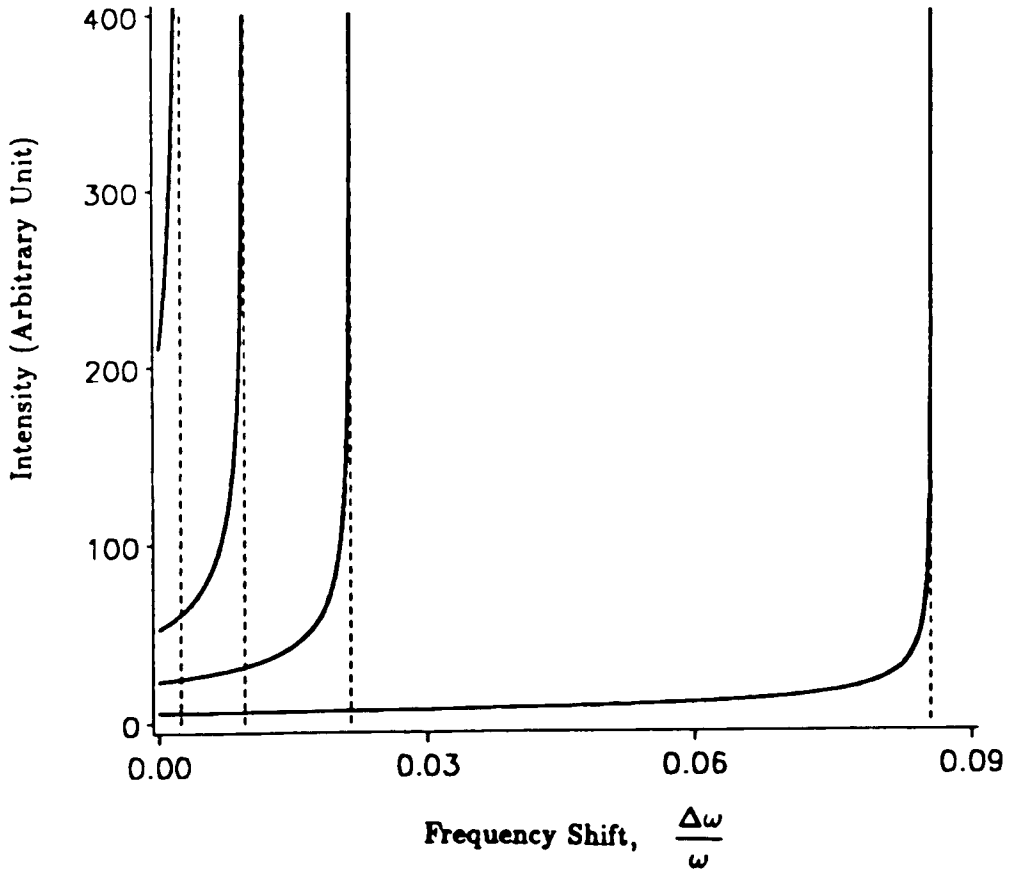

Figure 5.4: Powder pattern for a spin $I = 1$ NQR line in the presence of linearly polarized photons when $\frac{\omega_2}{\omega} = 1.0$, 2.0, 3.0, and 6.0. The parameters used are $\frac{\omega_Q}{2\pi} = 3.5\ MHz$ and $\frac{\omega}{2\pi} = 11.1\ kHz$.

$$B = \frac{\frac{3}{4}\frac{\omega_2^2}{\omega_Q \omega}}{1 - P^2(\frac{\omega}{\omega_Q})^2} \tag{5.16}$$

$$C = \frac{\frac{\omega\omega_2}{\omega_Q^2}}{1 - P^2(\frac{\omega}{\omega_Q})^2} P^2 \tag{5.17}$$

and by Eq. 5.1,

$$\cot\theta = \frac{\mu}{\sqrt{1-\mu^2}} \frac{\omega_2}{\omega} \sqrt{1-\mu^2}, \tag{5.18}$$

We can rewrite Eq. 4.79 as,

$$\begin{aligned} Z_\pm &= \frac{3}{2}\frac{\omega_2^2}{\omega_Q \omega} J_1^2(x_3) \\ &\quad + \sum_{P=1}^{\infty} \left\{ A \frac{\mu^2}{1-\mu^2} J_P^2(x_3) + B[J_{P-1}(x_3) - J_{P+1}(x_3)]^2 \right\} \\ &\quad \pm \sum_{P=1}^{\infty} C \frac{\mu}{\sqrt{1-\mu^2}} J_P(x_3)[J_{P-1}(x_3) - J_{P+1}(x_3)] \end{aligned} \tag{5.19}$$

The derivative of $Z_\pm$ with respect to $d\mu$ is done by deriving each term in Eq. 5.19 by parts. The following lists the derivatives of several block terms,

$$\frac{d}{d\mu}\frac{\mu^2}{1-\mu^2} = \frac{2\mu}{(1-\mu^2)^2} \tag{5.20}$$

$$\frac{d}{d\mu} x_3 = -\frac{\omega_2}{\omega}\frac{\mu}{\sqrt{1-\mu^2}} \tag{5.21}$$

$$\frac{d}{d\mu}\frac{\mu}{\sqrt{1-\mu^2}} = \frac{1}{(1-\mu^2)^{3/2}} \tag{5.22}$$

By using the Bessel function relation of Eq. 5.10, we obtain the expression for the derivative $dZ_\pm/d\mu$,

$$\begin{aligned} \frac{dZ_\pm}{d\mu} &= -\frac{3\omega_2^3}{2\omega^2\omega_Q}\frac{\mu}{\sqrt{1-\mu^2}} J_1(x_3)[J_0(x_3) - J_2(x_3)] \\ &\quad + \sum_{P=1}^{\infty} A \left\{ \frac{2\mu}{(1-\mu^2)^2} J_P^2(x_3) - \frac{\omega_2}{\omega}\frac{\mu^3}{(1-\mu^2)^{3/2}} J_P(x_3)[J_{P-1}(x_3) - J_{P+1}(x_3)] \right\} \end{aligned}$$

$$-\sum_{P=1}^{\infty} B\frac{\omega_2}{\omega}\frac{\mu}{\sqrt{1-\mu^2}}[J_{P-1}(x_3)-J_{P+1}(x_3)][J_{P-2}(x_3)-2J_P(x_3)+J_{P+2}(x_3)]$$

$$\pm\sum_{P=1}^{\infty} C\left\{\frac{1}{(1-\mu^2)^{3/2}}J_P(x_3)[J_{P-1}(x_3)-J_{P+1}(x_3)]\right.$$

$$-\frac{\omega_2}{2\omega}\frac{\mu^2}{1-\mu^2}[J_{P-1}(x_3)-J_{P+1}(x_3)]^2$$

$$\left.-\frac{\omega_2}{2\omega}\frac{\mu^2}{1-\mu^2}[J_{P-2}(x_3)-2J_P(x_3)+J_{P+2}(x_3)]\right\} \qquad (5.23)$$

The shape functions of the lines $\omega_\pm$, labeled as $g(Z_\pm)$, are the absolute value of the reciprocal of Eq. 5.23,

$$g(Z_\pm)=\frac{1}{\left|\frac{dZ_\pm}{d\mu}\right|} \quad . \qquad (5.24)$$

Employing equations 5.19, 5.23, and 5.24 in a numerical computation, we obtained the powder pattern lineshapes for a circularly polarized dressing field. The same parameters as those for the linearly polarized dressing field were used. The resulting lineshapes for ω_+ at dressing strengths $\frac{\omega_2}{\omega}$ = 0.66, 3.0, and 6.0 are plotted in Figs. 5.5 to 5.7, respectively. The lineshape for ω_- at a dressing strength of $\frac{\omega_2}{\omega}$ = 3.0 is plotted in Fig. 5.8. The solid line on the graph shows the lineshape, the left dashed line is the asymptote of the line when θ = 90°, and the right dashed line simply connects the line to the abscissa.

Note that a comparison of Figs. 5.6 and 5.8, which plot the lineshapes of ω_+ and ω_- at same dressing strength, shows that they are almost identical. This is because the energy levels of $|\widetilde{\pm, n}>$, are almost degenerate, as derived in the last chapter.

Now consider the lineshapes resulting from the influence of circularly and linearly polarized dressing fields. Both are broadened by the photon dressing and have about the same width; the lineshapes both exhibit a peak intensity corresponding to θ equals 90 degrees. Comparison between the amounts of the peak shift $\frac{\Delta\omega}{2\pi}$ and width of the powder patterns of these two differently polarized photon dressing at the same dressing

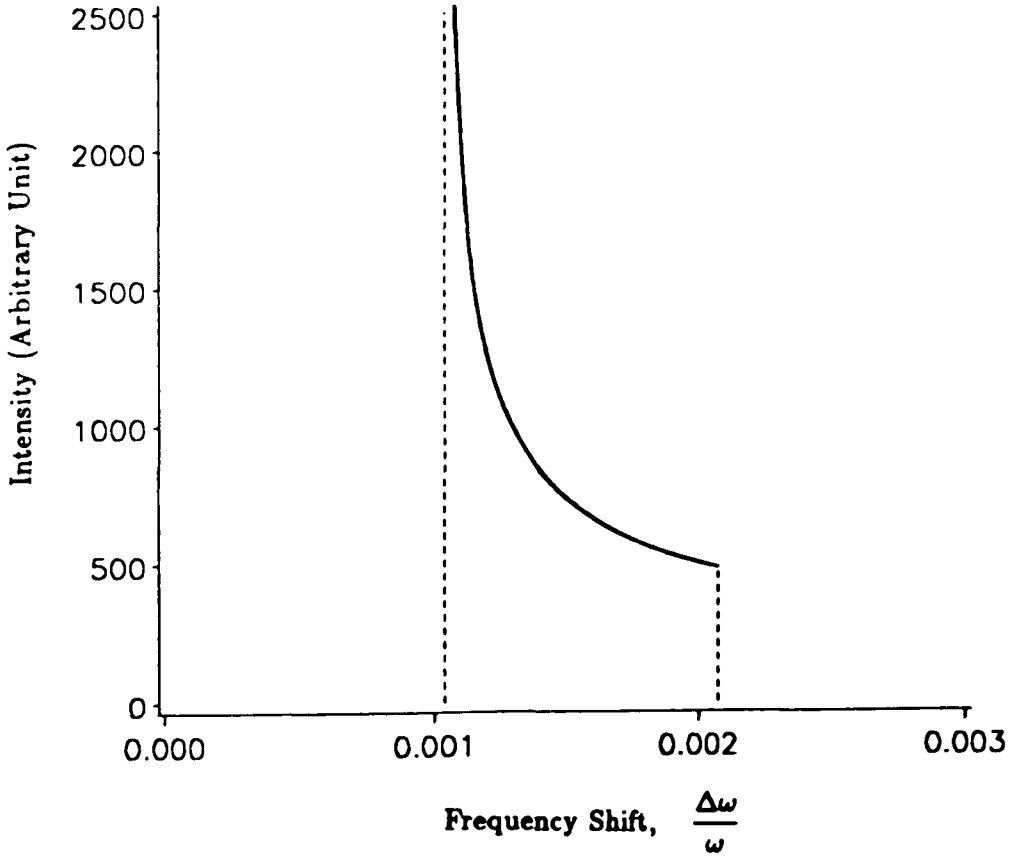

Figure 5.5: Powder pattern for a spin $I = 1$ NQR line ω_+ in the presence of circularly polarized photons when $\frac{\omega_2}{\omega} = 0.66$. The parameters used are $\frac{\omega_Q}{2\pi} = 3.5\ MHz$ and $\frac{\omega_c}{2\pi} = 11.1\ kHz$. The frequency shift $\frac{\Delta\omega}{2\pi}$ at $\theta = 0°$ is 23.02 Hz, at $\theta = 90°$ (peak) is 11.50 Hz.

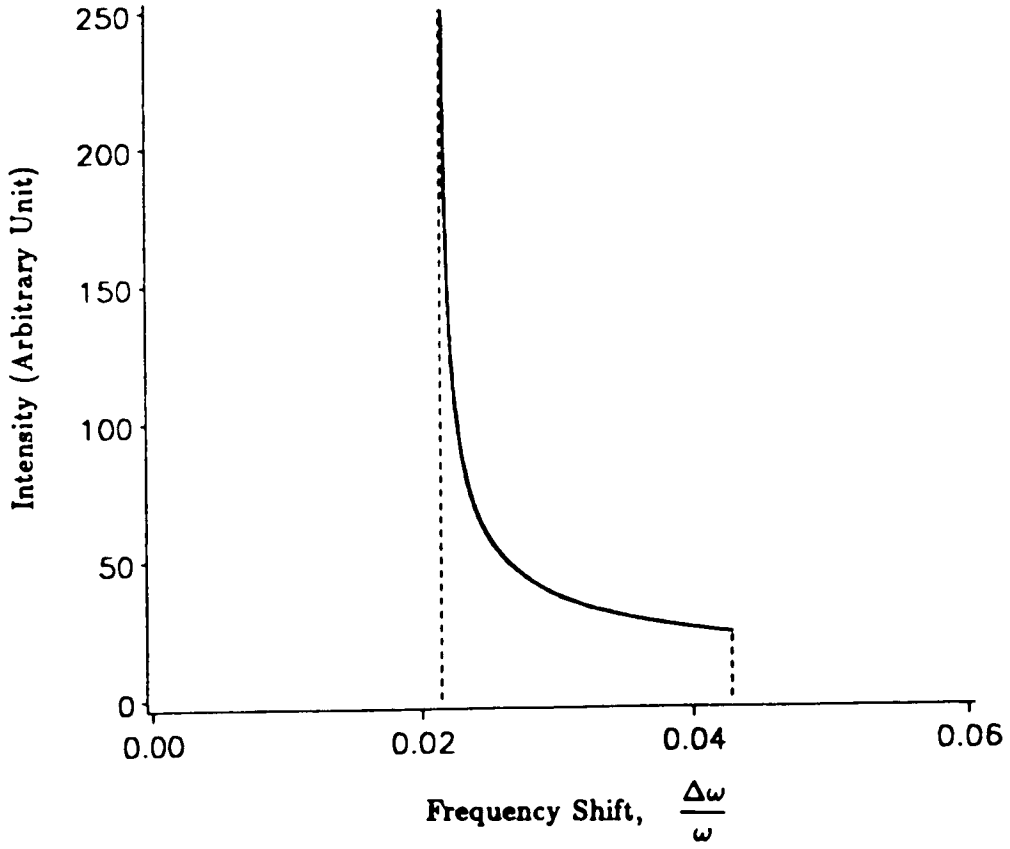

Figure 5.6: Powder pattern for a spin $I = 1$ NQR line ω_+ in the presence of circularly polarized photons when $\frac{\omega_2}{\omega} = 3.0$. The parameters used are $\frac{\omega_Q}{2\pi} = 3.5\ MHz$ and $\frac{\omega}{2\pi} = 11.1\ kHz$. The frequency shift $\frac{\Delta\omega}{2\pi}$ at $\theta = 0^o$ is 475.75 Hz, at $\theta = 90^o$ (peak) is 237.65 Hz.

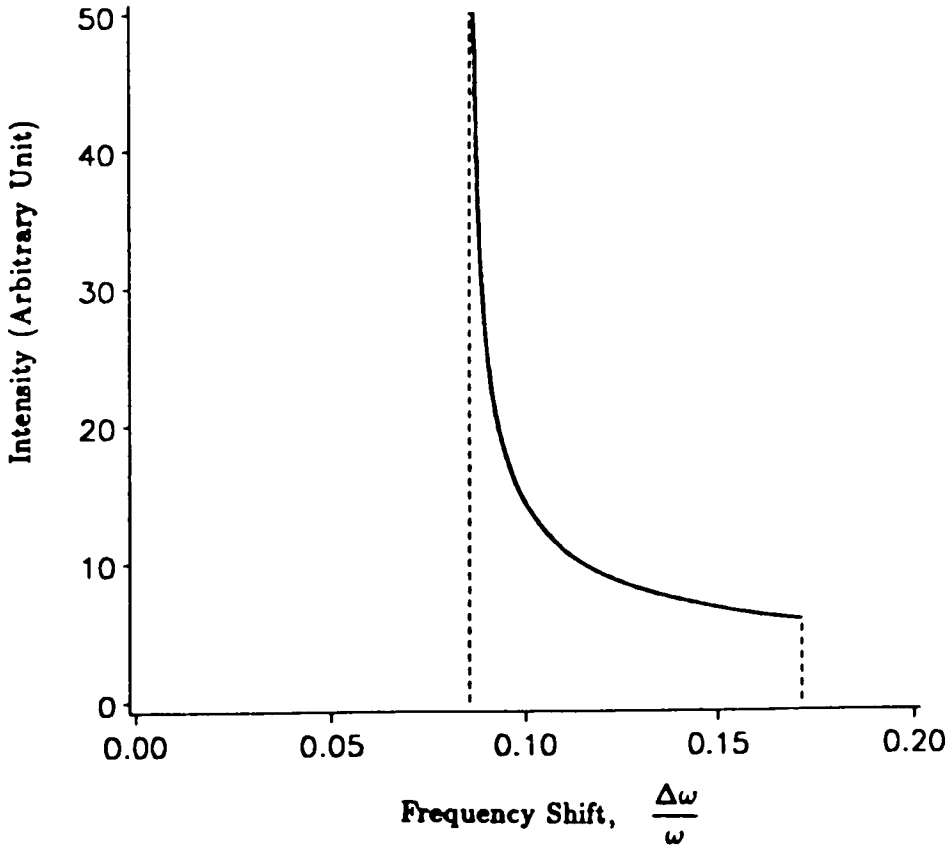

Figure 5.7: Powder pattern for a spin $I = 1$ NQR line ω_+ in the presence of circularly polarized photons when $\frac{\omega_2}{\omega} = 6.0$. The parameters used are $\frac{\omega_Q}{2\pi} = 3.5\ MHz$ and $\frac{\omega}{2\pi} = 11.1\ kHz$. The frequency shift $\frac{\Delta\omega}{2\pi}$ at $\theta = 0°$ is 1902.54 Hz, at $\theta = 90°$ (peak) is 950.60 Hz.

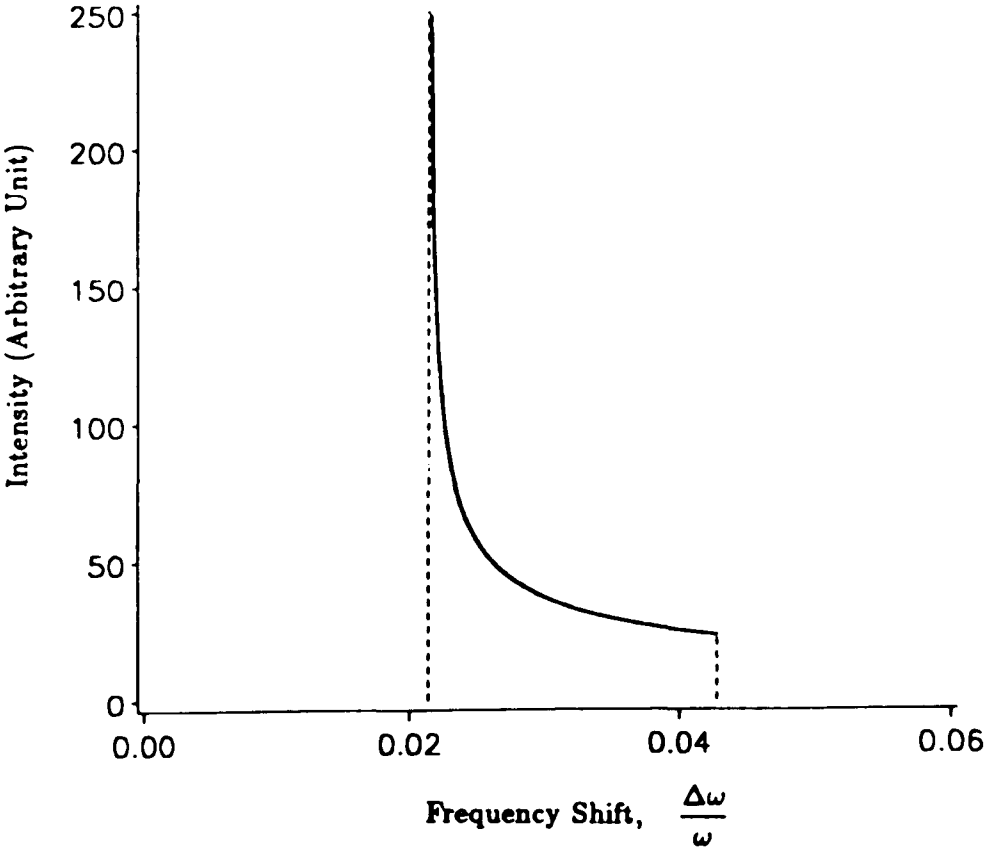

Figure 5.8: Powder pattern for a spin $I = 1$ NQR line ω_- in the presence of circularly polarized photons when $\frac{\omega_2}{\omega} = 3.0$. The parameters used are $\frac{\omega_Q}{2\pi} = 3.5\ MHz$ and $\frac{\omega_c}{2\pi} = 11.1\ kHz$. The frequency shift $\frac{\Delta\omega}{2\pi}$ at $\theta = 0°$ is 474.75 Hz, at $\theta = 90°$ (peak) is 237.65 Hz.

Dressing strength $\frac{\omega_1}{\omega}$		0.66	1.0	3.0	6.0
Peak shift at	linear	11.50	26.41	245.77	950.48
$\theta = 90^o$	circular	11.50	26.40	237.65	950.60
Width of powder pattern	linear	11.50	26.41	245.77	950.48
(Hz)	circular	11.52	26.46	237.1	951.94

Table 5.1: Peak shift $\frac{\Delta\omega}{2\pi}$ and width of powder patterns for linearly and circularly polarized dressing field.

strength, does not show any significant difference. The relevant values are summarized in Table 5.1. From these computations one can conclude that one would obtain the same shift and the same width in an experiment with either type of dressing.

Our results show that under the influence of a linearly or circularly polarized dressing field, the NQR line of spin $I = 1$ nuclei is shifted and broadened, but not split. The two different dresing polarizations do not lead to major differences. This is in contrast to the case of spin equals $\frac{3}{2}$ nuclei [28, 30, 31], where there is a frequency shift in the presence of linear polarized dressing, similar to the results as our spin 1 case; but where there is both a shift and a splitting of the lines in the presence of circularly polarized dressing, which is very different from our results. The reason for this difference has been discussed in section 4.2.

For nuclei of integer spin, however, there is an interesting difference between linearly and circularly polarized dressing. Although for both polarization, the $\theta = 90^o$ orientation corresponds to the peak intensity of the lineshape, this orientation corresponds to maximum frequency shift in the linearly polarized dressing, but minimum frequency shift in the circularly polarized case. Note that the "shoulder" of the lineshape is located at left side of the peak in the linearly polarized case, but on the right side of the peak in the circularly polarized case.

For a single crystal sample arranged to have θ equals zero, one expects no effect when the dressing field is linearly polarized, but maximum frequency shift when the dressing field is circularly polarized. This intersting characteristic can be used to locate the orientation of the principal EFG ζ axis of a single crystal by rotating the single crystal while searching for the maximum (or zero) of the frequency shift under the effect of circularly (or linearly) polarized photon dressing. For dressing strength $\frac{\omega_2}{\omega} = 3.0$, the frequency difference between the maximum and minimum of the shift is about 400 Hz, sufficient to enable one to locate the ζ axis.

Fig. 5.9 depicts the lineshapes when $\frac{\omega_2}{\omega} = 1.0$, 3.0, and 6.0. The intensity of the lines at $\theta = 90^o$ does not equal to infinity in this case, but is a large finite quantity. Similar as the linear case, although the lineshape has intensities over the whole range of frequency shift away from $\theta = 90^o$, the intensity drops quickly compared to the peak value and would probably not be detected.

Fig. 5.5 is the lineshape for $\frac{\omega_2}{\omega} = 0.66$, the maximum dressing strength reachable in our experiment. The peak shift $\frac{\Delta\omega_\pm}{2\pi}$ is 11.5 Hz. For the samples we studied with linewidth of about one kHz, this shift is not observable. The experimental data showed that the NQR line was narrowed (due to photon dressing on neighbour photon), but not shifted under the effect of circularly polarized photon dressing, which is consistent with our theory.

5.4 Powder Pattern of Spin $I = \frac{3}{2}$ NQR line in the Presence of a Linearly Polarized Dressing Field

The Na NQR frequency shift caused by linearly polarized non-resonant photon dressing in a single crystal of $NaClO_3$, expressed by equations (2.12) and (2.13) in Ito's paper[31], can be generalized to that of any spin $I = \frac{3}{2}$ nucleus in the powder or polycrystalline specimen with axially symmetric EFG. This frequency shift can be expressed

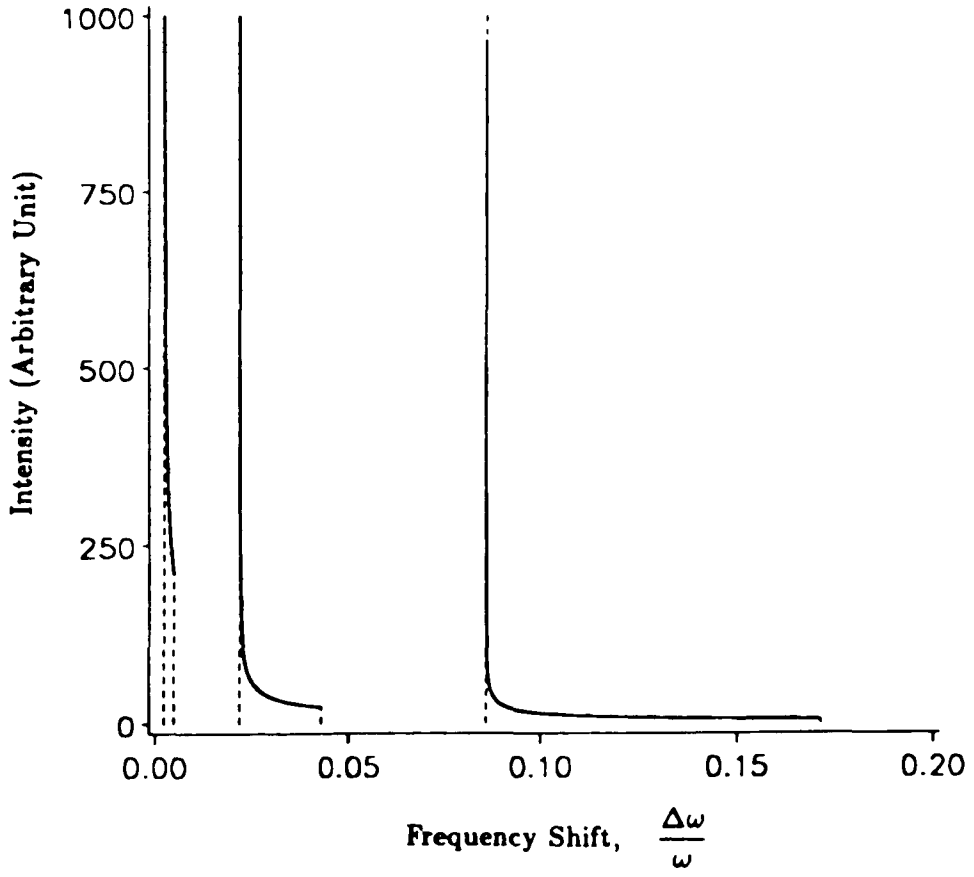

Figure 5.9: Powder pattern for a spin $I = 1$ NQR line ω_+ in the presence of circularly polarized photons when $\frac{\omega_2}{\omega} = 1.0$, 3.0, and 6.0. The parameters used are $\frac{\omega_Q}{2\pi} = 3.5\ MHz$ and $\frac{\omega}{2\pi} = 11.1\ kHz$.

in the general case as,

$$\frac{\Delta\omega'}{\omega} = \sum_{P=1}^{\infty} \frac{\frac{3}{4}\frac{\omega_2^2}{\omega_Q \omega}}{1 - P^2(\frac{\omega}{\omega_Q})^2} \sin^2\theta \left\{ \cos^2(\frac{\alpha}{2})[J_{P-1}(x') + J_{P+1}(x')]^2 \right.$$

$$\left. + \sin^2(\frac{\alpha}{2})[J_{P-1}(x'') + J_{P+1}(x'')]^2 \right\} \qquad (5.25)$$

where

$$\tan\alpha = 2\tan\theta \qquad (5.26)$$

and

$$x' = \frac{\omega_2}{2\omega}\left(\sqrt{\cos^2\theta + 4\sin^2\theta} - 3\cos\theta\right) \qquad (5.27)$$

$$x'' = \frac{\omega_2}{2\omega}\left(\sqrt{\cos^2\theta + 4\sin^2\theta} + 3\cos\theta\right) \qquad (5.28)$$

the angle θ is the angle between the principal EFG ζ axis and the oscillating axis of polarization of the dressing field, as in the previous section. For a single crystal of $NaClO_3$, when the oscillating field is applied along the (001) axis of the unit cell of $NaClO_3$, the angle θ is equals to 54°44′. For this particular θ value, $\cos\theta$ has the value of $1/\sqrt{3}$, Eq. 5.25 reduces to Eq. (2.12) and (2.13) of Ito's paper[31].

When polycrystalline specimen is under study, all possible orientations of the EFG ζ axis will be equally likely, so that the resulting NQR line is a powder pattern.

Let

$$Z' = \frac{\Delta\omega'}{\omega}, \qquad (5.29)$$

the shape function $g(Z')$ can be obtained through,

$$g(Z') = \left|\frac{d\mu}{dZ'}\right| \qquad (5.30)$$

To find the derivative dZ' with respect to $d\mu$, we first need convert the function of angle α into angle θ. By trigonometrical calculations using Eqs. 5.26 and 5.1, these

convertions are given as,

$$\cos^2(\frac{\alpha}{2}) = \frac{1}{2} + \frac{\mu}{2\sqrt{4-3\mu^2}} \tag{5.31}$$

$$\sin^2(\frac{\alpha}{2}) = \frac{1}{2} - \frac{\mu}{2\sqrt{4-3\mu^2}} \tag{5.32}$$

with θ and α in the range of $-\frac{\pi}{2}$ to $\frac{\pi}{2}$.

The following lists the derivatives of several block terms,

$$\frac{dx'}{d\mu} = \frac{3\omega_2}{2\omega}\left(1 - \frac{\mu}{\sqrt{4-3\mu^2}}\right) \tag{5.33}$$

$$\frac{dx''}{d\mu} = -\frac{3\omega_2}{2\omega}\left(1 + \frac{\mu}{\sqrt{4-3\mu^2}}\right) \tag{5.34}$$

$$\frac{d(\cos^2\frac{\alpha}{2})}{d\mu} = \frac{2}{(4-3\mu^2)^{3/2}} \tag{5.35}$$

$$\frac{d(\sin^2\frac{\alpha}{2})}{d\mu} = -\frac{2}{(4-3\mu^2)^{3/2}} \tag{5.36}$$

$$\frac{d(\sin^2\theta)}{d\mu} = -2\mu. \tag{5.37}$$

Deriving Eq. 5.25 by parts, using the notation of Eq. 5.16, $\frac{dZ'}{d\mu}$ can be expressed as,

$$\begin{aligned}\frac{dZ'}{d\mu} = \sum_{P=1}^{\infty} B\Big\{ & \frac{4}{3}\frac{\omega}{\omega_2} P\left\langle [J_{P-1}(x') + J_{P+1}(x')]J_P(x') - [J_{P-1}(x'') + J_{P+1}(x'')]J_P(x'')\right\rangle \\ & -\frac{2}{3}\frac{5-3\mu^2}{(4-3\mu^2)^{3/2}}\left\langle [J_{P-1}(x') + J_{P+1}(x')]^2 - [J_{P-1}(x'') + J_{P+1}(x'')]^2\right\rangle \\ & +3\frac{\omega_2}{\omega}\frac{(1-\mu^2)^2}{4-3\mu^2}\left\langle [J_{P-1}(x') + J_{P+1}(x')][J_{P-2}(x') - J_{P+2}(x')]\right. \\ & \left. -[J_{P-1}(x'') + J_{P+1}(x'')][J_{P-2}(x'') - J_{P+2}(x'')]\right\rangle\Big\}. \end{aligned} \tag{5.38}$$

Then, the shape function $g(Z')$ is given by,

$$g(Z') = \frac{1}{\left|\frac{dZ'}{d\mu}\right|} \tag{5.39}$$

Using equations 5.25, 5.38 and 5.39, lineshapes of $\frac{\omega_2}{\omega} = 1.0$ and 3.0 are plotted in Figs. 5.10 and 5.11. Fig. 5.12 depicts the lineshapes for $\frac{\omega_2}{\omega} = 1.0$, 3.0, and 6.0 on the same graph. The parameters used are chosen to match those of single crystal $NaClO_3$'s, $\frac{\omega_Q}{2\pi} = 395.5\ kHz$ and $\frac{\omega}{2\pi} = 11.8\ kHz$. The corresponding shift position for single crystal $NaClO_3$ is marked on the figures by an "X". The lineshapes of $I = \frac{3}{2}$ and 1 NQR lines under the influence of linearly polarized photon dressing are very similar, the discussions for spin 1 lineshapes are all applicable to the spin $\frac{3}{2}$ cases. The only difference in the lines between spin $\frac{3}{2}$ and spin 1 nuclei is, the $I = \frac{3}{2}$ lines shift more compared to spin 1. For example, the peak shift for spin $\frac{3}{2}$ is 264.44 Hz but spin 1 is only 26.41 Hz for the same dressing strength $\frac{\omega_2}{\omega} = 1.0$.

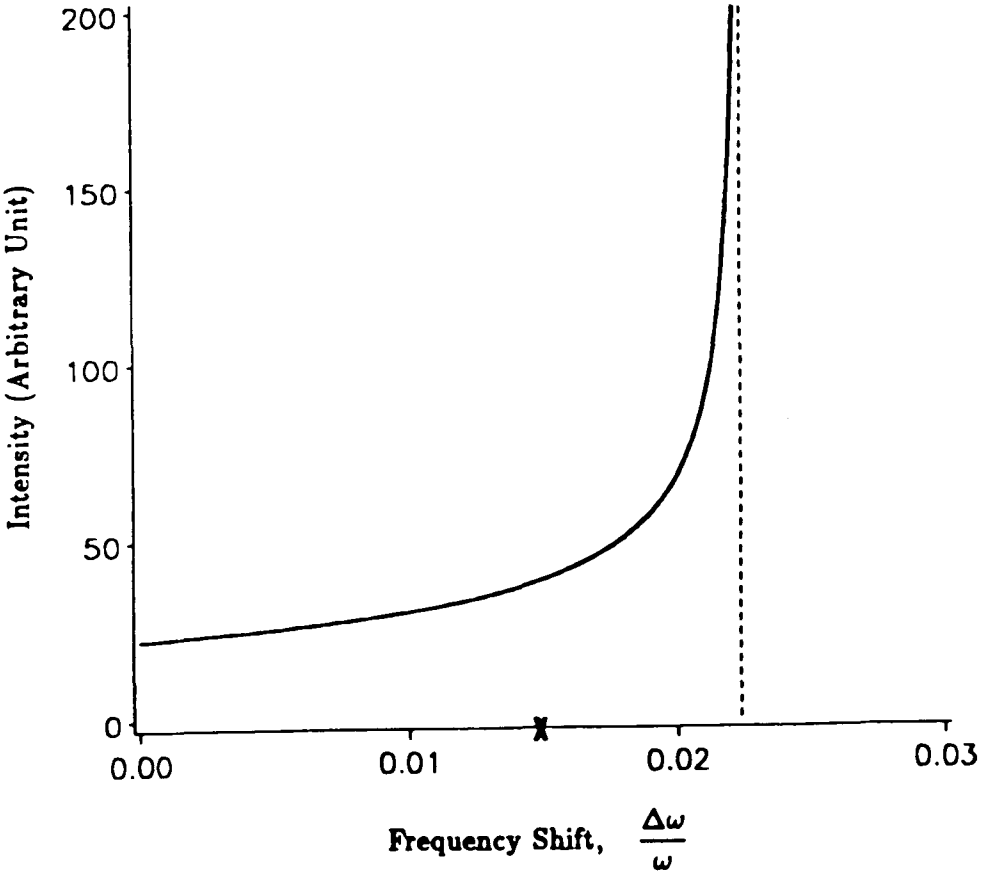

Figure 5.10: Powder pattern for a spin $I = \frac{3}{2}$ NQR line under the influence of linearly polarized photons when $\frac{\omega_2}{\omega} = 1.0$. The parameters used are $\frac{\omega_Q}{2\pi} = 395.5\ kHz$ and $\frac{\omega_E}{2\pi} = 11.8\ kHz$. "$X$" indicates frequency shift $\frac{\Delta\omega}{2\pi}$ of 176.29 Hz for single crystal at $\theta = 54°44'$. The peak shift at $\theta = 90°$ is 264.44 Hz.

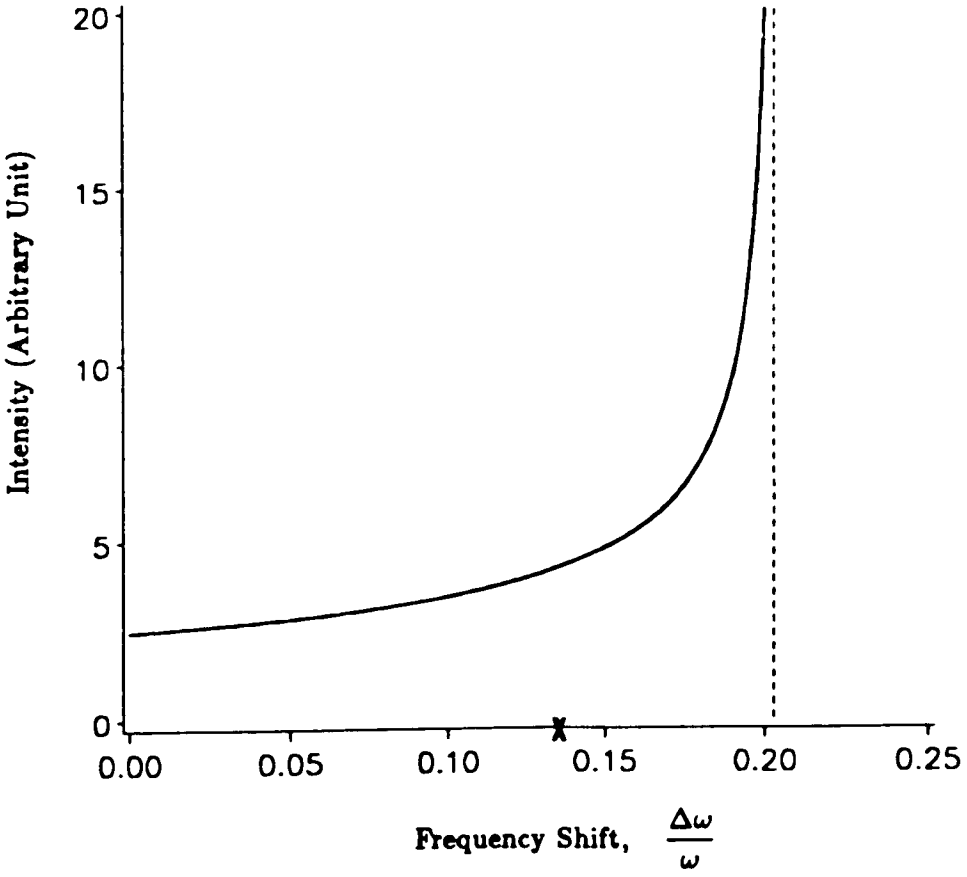

Figure 5.11: Powder pattern for a spin $I = \frac{3}{2}$ NQR line under the influence of linearly polarized photons when $\frac{\omega_2}{\omega} = 3.0$. The parameters used are $\frac{\omega_Q}{2\pi} = 395.5\ kHz$ and $\frac{\omega}{2\pi} = 11.8\ kHz$. "$X$" indicates frequency shift $\frac{\Delta\omega}{2\pi}$ of $1.595\ kHz$ for single crystal at $\theta = 54°44'$. The peak shift at $\theta = 90°$ is $2.393\ kHz$.

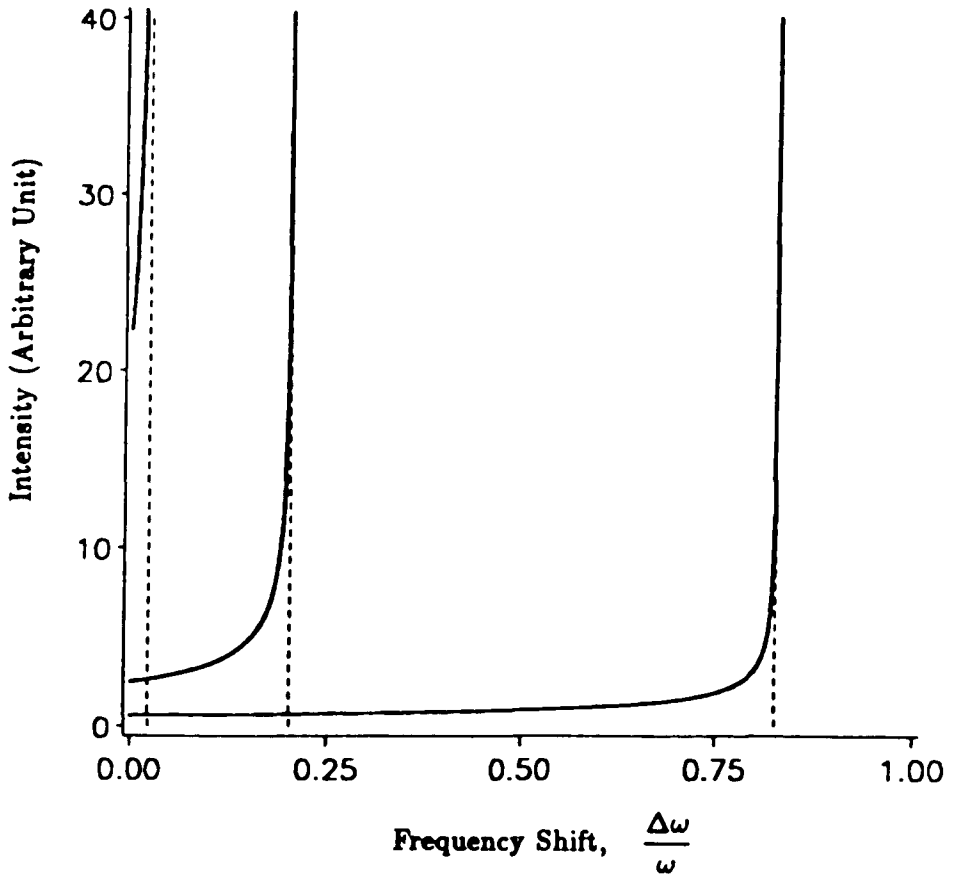

Figure 5.12: Powder pattern for a spin $I = \frac{3}{2}$ NQR line under the influence of linearly polarized photons when $\frac{\omega_2}{\omega} = 1.0$, 3.0, and 6.0. The parameters used are $\frac{\omega_Q}{2\pi} = 395.5\ kHz$ and $\frac{\omega}{2\pi} = 11.8\ kHz$.

Chapter 6

Energy Levels of Protons Dressed by Circularly Polarized Photons in Zero Static Field

6.1 Introduction

The substances that have been studied by photon dressing for this thesis are Hexamethylenetetramine (HMT), Triethylenediamine (TED), and Trimethylamine (TMA). ^{14}N FID signals are studied to see the effect of non-resonant photon dressing. In all of these three substances, ^{12}C and protons are the close neighbours of nitrogen nuclei. Since ^{12}C has zero spin, the only neighbours of interest are protons. When the dressing field is applied to the substance, all of the nuclei in the substance are "dressed" by the photons simultaneously. The effect of photon dressing on protons is very important to us not only because protons are the nearest neighbours of nitrogen, but also because protons have the largest value of the gyromagnetic ratio γ. The effect of photon dressing, as shown in the previous chapters, is a function of the dressing strength, $\omega_2 = \gamma H_2$, with H_2 the amplitude of the dressing field. So that what's important is the product of γ and H_2. In our substance, the γ_P value for the proton is $2\pi \times 4.257\ kHz/G$, and γ_N value for ^{14}N is $2\pi \times 0.307\ kHz/G$; γ_P is 13.87 times as large as γ_N. For the maximum dressing field of $24G$ reached in our experiment, $\frac{\omega_2}{\omega}$ for ^{14}N is only 0.66, but for proton is 9.2. Therefore the effect of photon dressing observed in our experiment is mainly due to the dressing on protons instead of on ^{14}N. For this reason, we treat in this chapter the effect of photon dressing on protons.

We remind the reader that the dressing frequency ω should be much much smaller than the ^{14}N NQR frequency ω_Q, but much larger than the linewidth of ^{14}N and ^{1}H,

to satisfy the perturbation condition and to achieve the effect of line narrowing.

6.2 Energy Levels of Protons Dressed by Circularly Polarized Photons in Zero Static Field

The proton does not have an observable electric quadrupole moment, so we can discuss the problem in the x, y, z, laboratory coordinate system, but the z axis should be chosen to coincide with the EFG ζ axis, since the orientation of the proton is related to the EFG of ^{14}N. Assume the rotating axis of the dressing field make an arbitrary angle θ with z axis. Since there are no restrictions on the orientation of x, y axes in the plane perpendicular to z axis, the problem of decomposing the dressing field into the x, y, z coordinate system is the same as that of discussed in the beginning of Section 4.2.1. Therefore, the interaction hamiltonian V between the proton and the dressing field, has the same form as Eq. 4.61, which includes π, σ^+, and σ^-, three different photon polarizations. The total hamiltonian of the proton and the circularly polarized dressing field is,

$$\mathcal{H} = \omega a^+ a + V^0 + V^+ + V^- \tag{6.1}$$

where

$$V^0 = \lambda \sin\theta I_z (a^+ + a) \tag{6.2}$$

$$V^+ = \frac{\lambda}{2}(\cos\theta + 1)(I_+ a + I_- a^+) \tag{6.3}$$

$$V^- = \frac{\lambda}{2}(\cos\theta - 1)(I_+ a^+ + I_- a) \tag{6.4}$$

and

$$I_\pm = I_x \pm i I_y. \tag{6.5}$$

For the moment neglecting the interaction V, the hamiltonian $\mathcal{H}_o = \omega a^+ a$ has eigenstates $|\pm, n>$ and eigenenergy $n\omega$, where "$\pm$" indicates the orientation of proton spin along or opposite to the z axis, so that the magnetic quantum number has the

value of $+\frac{1}{2}$ and $-\frac{1}{2}$, respectively. The quantum number $\pm\frac{1}{2}$ is very important because it is directly related to the z component of the local field due to the proton.

The hamiltonian $\mathcal{H}_o$ plus either one of the above three terms of V can be solved exactly, with the result that V^0 will only bring a uniform energy translation to $\mathcal{H}_o$, but either V^+ or V_- will lift the degeneracy of $\mathcal{H}_o$. In the region of θ between 0 to 50 degrees, V^+ is the dominant part of V. We will consider V^+ first, and treat the other two terms V^0 and V^- as perturbations on the eigenstates of $\mathcal{H}_o + V^+$. The eigenstates and eigenenergies of the hamiltonian $\mathcal{H}_o + V^+$, can be obtained by diagonalizing its matrix in the eigenstates of $\mathcal{H}_o$. Only the states $|+, n>$ and $|-, n+1>$ are joint by V^+, so, we need to diagonalize the following 2×2 matrix,

$$\begin{pmatrix} n\omega & \frac{\cos\theta+1}{2}\lambda\sqrt{n+1} \\ \frac{\cos\theta+1}{2}\lambda\sqrt{n+1} & (n+1)\omega \end{pmatrix} \tag{6.6}$$

The eigenenergies of matrix 6.6 can easily be obtained,

$$E(\overline{+,n}) = n\omega + \frac{1}{2}\left(\omega - \sqrt{\omega^2 + (\frac{\cos\theta+1}{2})^2\omega_2^2}\right) \tag{6.7}$$

$$E(\overline{-,n+1}) = (n+1)\omega - \frac{1}{2}\left(\omega - \sqrt{\omega^2 + (\frac{\cos\theta+1}{2})^2\omega_2^2}\right) \tag{6.8}$$

The corresponding eigenvectors are linear combination of $|+, n>$ and $|-, n+1>$; they are expressed as,

$$|\overline{+,n}> = \cos(\frac{\beta}{2})|+, n> - \sin(\frac{\beta}{2})|-, n+1> \tag{6.9}$$

$$|\overline{-,n+1}> = \cos(\frac{\beta}{2})|-, n+1> - \sin(\frac{\beta}{2})|+, n> \tag{6.10}$$

where

$$\tan\beta = \frac{\cos\theta+1}{2}\frac{\omega_2}{\omega}. \tag{6.11}$$

Recalling the discussion in section 3.3.2, we note that under the influence of V^+, the proton spin oscillates between the states $|+, n>$ and $|-, n+1>$ with frequency $[E_{\overline{|-,n+1>}} - E_{\overline{|+,n>}}]$. This oscillating frequency is of the order of ω, much larger than the linewidth of the ^{14}N and ^{1}H resonances. The local field associated with a proton oscillating at this frequency is averaged to a small value and does not effect the ^{14}N NQR echo decay rate as much as before. Under the influence of σ^+ photon itself, the ^{14}N NQR line is narrowed.

The energy levels of $\mathcal{H}_o$ and $\mathcal{H}_o + V^+$ when $\theta = 30°$ are drawn in Fig. 6.1 as dashed and solid lines respectively. The original degeneracy of states $|\pm, n>$ are lifted and the energy level diagram exhibits infinite number of crossings. The crossing point labeled as I_m is the crossing crossed by states $|\overline{+, n}>$ and $|\overline{-, n-m}>$. The position of these crossing points at the abscissa can be deduced by using the fact that at crossing I_m the states $|\overline{+, n}>$ and $|\overline{-, n-m}>$ have the same energy. These positions are expressed as,

$$\frac{\omega_2}{\omega} = \pm \frac{2}{\cos\theta + 1}\sqrt{m(m+2)}. \tag{6.12}$$

For a single crystal, the angle θ has a certain value, so level crossing happens at definite value of $\frac{\omega_2}{\omega}$. For a powdered crystal or polycrystalline sample, θ can have any possible values, so that level crossings happen at different values of $\frac{\omega_2}{\omega}$. Fig. 6.2 shows the energy level diagram of $\mathcal{H}_o + V^+$ for different θ values, where dotted, solid, long dashed, and dash-dotted curves are used for θ value of 0°, 30°, 60°, and 90° respectively. Due to the distribution of θ, the crossing I_m for same m of the energy level diagram is located at different positions, thus, all of the phenomena which relate to the position of the crossings will be "wiped" out.

Now we treat the effect of $V' = V^0 + V^-$ as perturbation on eigenstates of $\mathcal{H}_o + V^+$. By using the resolvent method discussed in Section 3.2, the perturbed energy near the level crossing I_m, can be obtained by using Eq. 3.31, where the diagonal and off-diagonal elements of the matrix $\bar{R}$ can be calculated by using Eqs. 3.26 and 3.28 respectively.

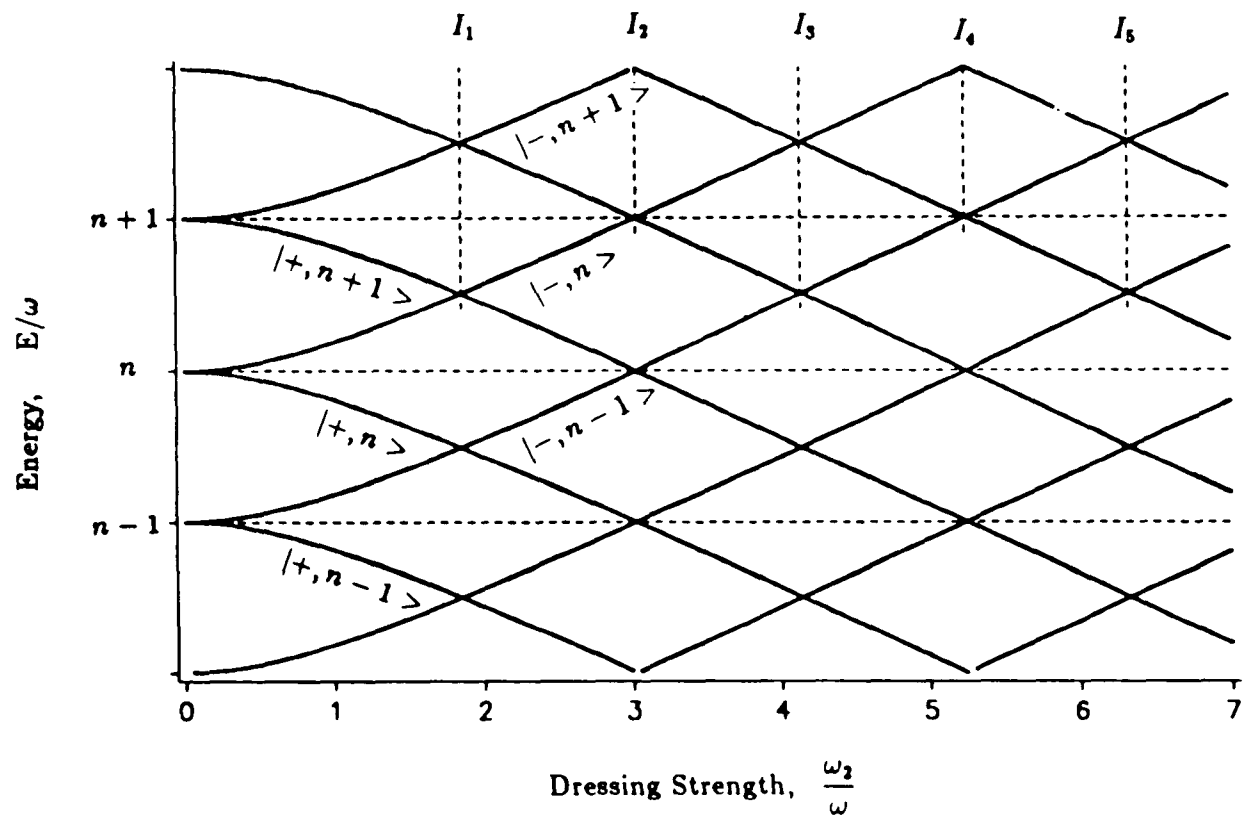

Figure 6.1: Dressed proton energy level diagrams. Dashed lines, hamiltonian $\mathcal{H}_o = \omega a^+ a$. Solid curves, hamiltonian $\mathcal{H}_o + V^+$.

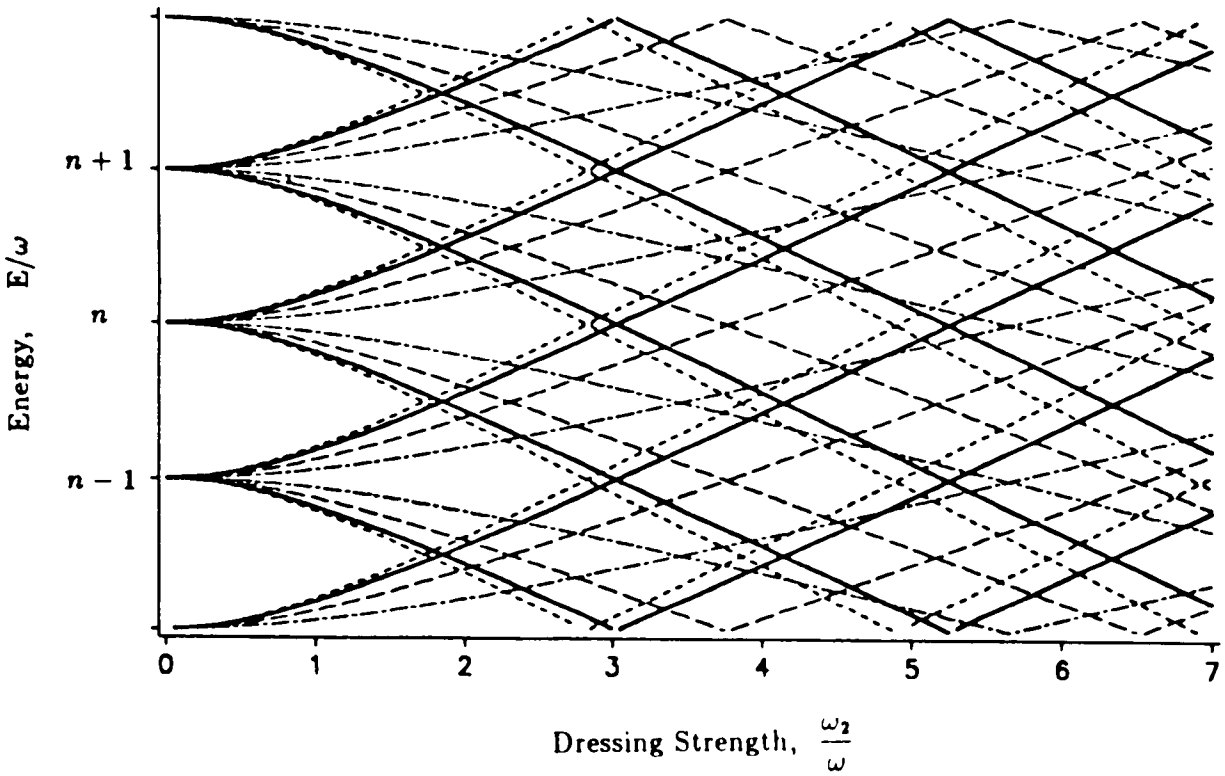

Figure 6.2: Energy level diagram of proton dressed by σ_+ photons when $\theta = 0°$ (dotted), 30° (solid), 60° (long dashed), and 90° (dash-dotted curve).

We label the states which cross as $|a_r>$ and $b_s>$, where

$$|a_r> = |\overline{+, n-r}> = \cos\frac{\beta}{2}|+, n-r> - sin\frac{\beta}{2}|-, n-r+1> \quad (6.13)$$

$$|b_s> = |\overline{-, n-s}> = \cos\frac{\beta}{2}|-, n-s> - sin\frac{\beta}{2}|+, n-s-1> \quad (6.14)$$

States $|a_r>$ and $|b_s>$ cross at I_{s-r} with s and r integers.

Now let us calculate the diagonal elements of the matrix $\bar{R}^m_{aa}$ and $\bar{R}^m_{bb}$ for crossing I_m crossed by states $|a>$ and $|b_m>$. The intermediate states $|i>$ in Eq. 3.26 for $\bar{R}^m_{aa}$ in the lowest second order, are $|b_0>$, $|b_1>$, $|b_{-2}>$, $|b_{-3}>$, $|a_{\pm 1}>$, and $|a_{\pm 2}>$. The common energy at crossing point is calculated to be,

$$\bar{E}_c = \bar{E}_{|a>} = n\omega - \frac{1}{2}m\omega \quad (6.15)$$

and the energy of states $|a_r>$ and $|b_s>$ at crossing I_m have the forms,

$$E_{|a_r>} = (n-r)\omega - \frac{1}{2}m\omega, \quad (6.16)$$

$$E_{|b_s>} = (n-s)\omega + \frac{1}{2}m\omega. \quad (6.17)$$

By adding up the contributions of the above eight intermediate states, $\bar{R}^m_{aa}$ has the form,

$$\bar{R}^m_{aa} = -\frac{1}{16}\frac{\omega_2^2}{\omega}\left\{(\cos\theta - 1)^2\left[\frac{\cos^4(\frac{\beta}{2})}{m-1} + \frac{\sin^4(\frac{\beta}{2})}{m+3}\right]\right.$$

$$\left. + \sin^2\theta\sin^2\beta\left(\frac{1}{m} + \frac{1}{m+2}\right)\right\} \quad (6.18)$$

The intermediate states for $\bar{R}^m_{bb}$ are $|b_{m\pm 1}>$, $|b_{m\pm 2}>$, $|a_m>$, $|a_{m-1}>$, $|a_{m+2}>$, and $|a_{m+3}>$. After calculation, we get that $\bar{R}^m_{bb}$ has the same form as $\bar{R}^m_{ab}$, but opposite sign,

$$\bar{R}^m_{bb} = -\bar{R}^m_{aa} \quad (6.19)$$

The diagonal elements of the matrix has the same form for all crossing I_m. The off diagonal elements of the matrix $\bar{R}^m_{ab}$ are also calculated to the lowest order, they have

a different form for different m values. When $m = 0$, i.e. crossing I_o, there is no intermediate state,

$$\bar{R}^0_{ab} = < a|V^0|b_0 > = \frac{1}{4}\omega_2 \sin\theta \sin\beta \tag{6.20}$$

For crossing I_1, we have,

$$\bar{R}^1_{ab} = < a|V^-|b_1 > + \frac{< a|V^0|b_0 >< b_0|V^0|b_1 >}{E_c - E(b_0)} + \frac{< a|V^0|a_1 >< a_1|V^0|b_1 >}{E_c - E(a_1)}$$

$$= \frac{1}{4}\omega_2(\cos\theta - 1)\cos^2(\frac{\beta}{2}) \tag{6.21}$$

The calculation is quite straight forward, except great attention needs to be taken not to loose any intermediate states. When m is odd, only σ^- photons contribute to $\bar{R}^m_{ab}$, but when m is even, both σ^- and π photons contribute. When $m \geq 4$, more than one intermediate state is needed to join the crossed states. For example, for the I_5 crossing, four possible paths can join the crossed states $|a>$ and $|b_5>$ which have intermediate states $|b_1>$ and $|b_3>$; $|a_2>$ and $|a_4>$; $|b_1>$ and $|a_4>$; $|a_2>$ and $|b_3>$ respectively. Thus, $\bar{R}^m_{ab}$ becomes smaller when m value gets bigger. The off diagonal elements of the matrix $\bar{R}^m_{ab}$ for m up to five are listed below,

$$\bar{R}^2_{ab} = \frac{1}{8}\frac{\omega_2^2}{\omega}\sin\theta(\cos\theta - 1)\left[\cos^4(\frac{\beta}{2}) - \frac{1}{2}\sin^2\beta\right] \tag{6.22}$$

$$\bar{R}^3_{ab} = -\frac{1}{32}\frac{\omega_2^2}{\omega}(\cos\theta - 1)^2\sin\beta\cos^2(\frac{\beta}{2}) \tag{6.23}$$

$$\bar{R}^4_{ab} = \frac{5}{576}\frac{\omega_2^3}{\omega^2}\sin\theta(\cos\theta - 1)^2\sin\beta\cos^2(\frac{\beta}{2})\left[\sin^2(\frac{\beta}{2}) - 2\cos\beta\right] \tag{6.24}$$

$$\bar{R}^5_{ab} = \frac{9}{4096}\frac{\omega_2^3}{\omega^2}(\cos\theta - 1)^3\sin^2\beta\cos^2(\frac{\beta}{2}). \tag{6.25}$$

Applying these elements of the matrix $\bar{R}$ to Eq. 3.31, we can obtain the energy of the total hamiltonian $\mathcal{H}$ near each crossing. Because both the diagonal and off diagonal elements of the matrix $\bar{R}$ are not zero, based on the conclusions drawn in Chapter 3,

all of the crossings of $\mathcal{H}_o + V^+$ become shifted anticrossings. However, when $\theta = 0°$, that is, when the rotating axis coincides with the ζ axis of EFG coordinates, all of the elements of the matrix $\bar{R}^m = 0$, the energy diagram of the hamiltonian $\mathcal{H}_o + V^+$ remains unchanged. Examining Eqs. 6.2 to 6.4, this result is obvious. When $\theta = 0°$, the dressing field contain only σ^+ photons, since V^- and V^0 equal to zero.

Fig. 6.3 depicts the energy level diagram when $\theta = 30°$. Solid and dashed curves are energy levels of hamiltonians $\mathcal{H}$ and $\mathcal{H}_o + V^+$ respectively. Besides the crossing at the origin, which corresponds to zero dressing, all of the crossings of the unperturbed energy should be shifted and repel each other to form anticrossings. On the figure, however, only the first crossing forms a clear anticrossing, the others seem to remain crossed. To explain this, we need go through the detail calculation of the values of these off-diagonal elements of matrix $\bar{R}$. $\bar{R}^m_{ab}$ gets smaller and smaller as m gets bigger. For $\theta = 30°$, the absolute value of $\bar{R}^{(1)}_{ab}/\omega$ equals to 0.047, then reduces to 7.69×10^{-5}, 5.85×10^{-3}, 2.2×10^{-9}, and 7.65×10^{-4} for m equals 2 to 5 respectively. Generally, $\bar{R}^m_{ab}$ is much smaller when m is even. The minimum distance of an anticrossing is equal to $2\bar{R}_{ab}$. For $m \geq 2$, $\bar{R}^m_{ab}$ is too small to be shown on the figure in the case of $\theta = 30°$. For bigger θ, $\bar{R}^m_{ab}$ gets bigger, several anticrossings may be shown in the figure.

At the position of level anticrossings, the real multiple quantum transitions caused by the perturbing σ^- and π photons, increase the proton spin reorientation rate between the spin states $|\pm\frac{1}{2}>$ even more. The z component of the local field due to proton is directly related to the spin orientations. Thus this increasing in spin reorientation rate can average the local field fluctuation to an even smaller value, and the contribution of the proton local field fluctuation to its neighbour spin-echo relaxation time is decreased even further. Away from the anticrossing position, the fluctuation of proton local field goes back to a bigger value. So, if one studies the nuclear spin-echo relaxation time T_2 with protons as nearest neighbours, one should observe T_2 increase and oscillate with maximum values coinciding with the proton's anticrossing positions. Ito and Hashi [29] found that the ^{35}Cl spin echo time increase in single crystal P-dichlorobenzene can be explained very well by energy level diagrams of protons dressed by σ_+ and σ_- photons.

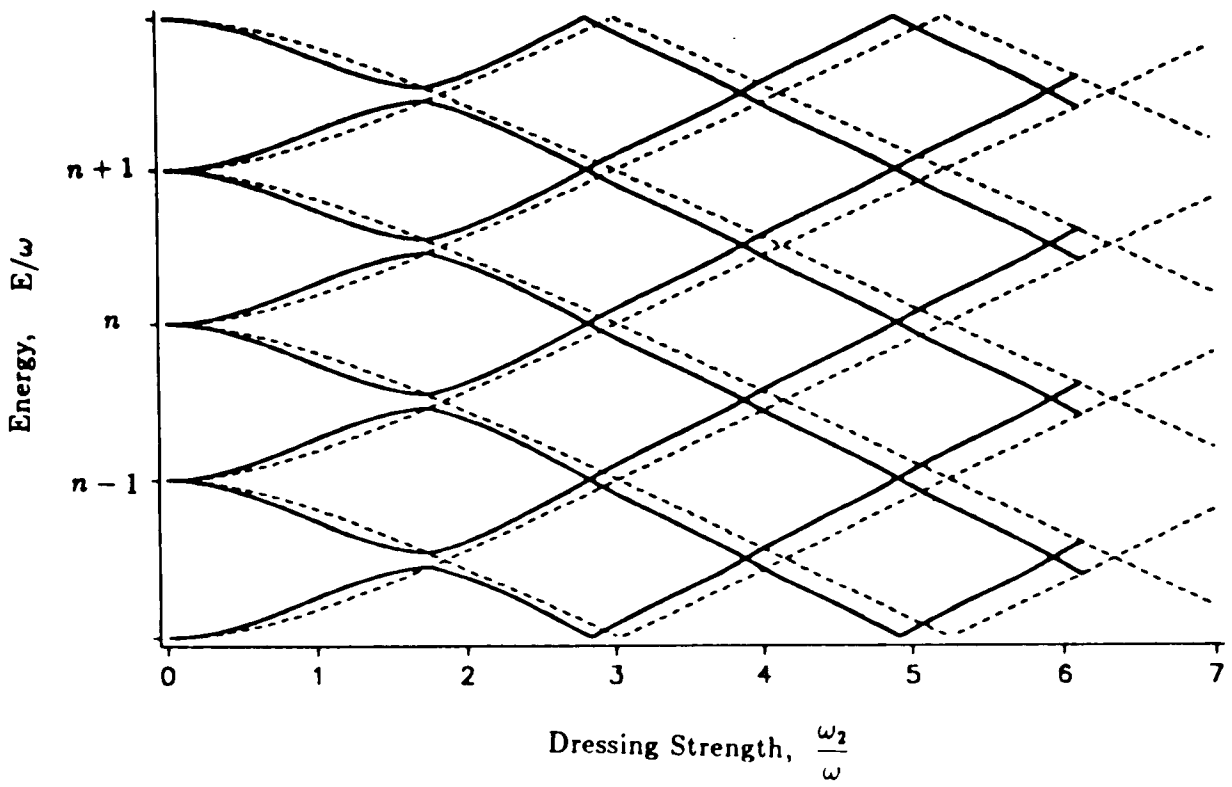

Figure 6.3: Energy level diagram of proton dressed by circularly polarized photons when $\theta = 30°$. Solid and dashed curves are energy levels of hamiltonian $\mathcal{H}$ and $\mathcal{H}_o + V$ respectively.

However, when powder or polycrystalline specimens are under study, the anticrossings in proton energy diagrams will happen at different places due to the distribution of angles, θ. One can only observe a monotonic increase of T_2, but no oscillations. As will be discussed in the next chapter, we performed field dressing experiments in TED and TMA. In both samples protons are the only nearest neighbours of the ^{14}N nuclei. We observed that under the influence of circularly polarized photon dressing, ^{14}N linewidth monotonically decreased without oscillating. This is in agreement with the theory.

So far, we only discussed the region where θ falls between 0° and 50°. When θ is in the region of 130° to 180°, V^- becomes dominant, and $V^0 + V^+$ may be treated as a perturbation and yield the same features as discussed above. In the region of θ between 50° and 130°, V^0 is comparable to or larger than V^+ (or V^-). Although compared to the base energy $n\omega$, all of the three terms of V can be considered as small quantities, it is safe not to use perturbation theory. However, examining the nature of V^+ and V^-, both of them can couple the states with quantum number $+\frac{1}{2}$ and $-\frac{1}{2}$, so that under their influence, protons will reorient between $\pm\frac{1}{2}$ states rapidly, and decrease their local magnetic field fluctuation seen by nitrogen. In summary, the effect of circularly polarized photon dressing on protons is to cause them to reorient between $\pm\frac{1}{2}$ states thus decoupling the spin-spin interaction between protons and nitrogen nuclei.

Chapter 7

Line Narrowing in ^{14}N NQR by Non-Resonant Irradiation

7.1 Introduction

Line broadening is not nearly as serious a problem in NQR spectroscopy as it is in NMR of solids, principally because there is no laboratory frame DC magnetic field imposed on normally polycrystalline samples [38]. Still, line-narrowing schemes are desirable not only because they might reveal previously unresolved structure, but also because they can lead to considerable improvement in detection sensitivity.

In 1977 and 1981 two new multiple pulse NQR techniques were reported [50, 51] which can allow orders of magnitude sensitivity enhancement for ^{14}N NQR. The pulse sequences involved have close analogies with previously well known NMR sequences, but a proper understanding of the evolution of the NQR hamiltonian during the sequences continues to be the subject of study[52, 53, 54]. A common requirement for these sequences to be effective from the point of view of signal-to-noise enhancement is that the pulse spacing be made smaller than T_2, the spin echo decay time. It is not surprising then that the most spectacular enhancements occur only in the special case when the combination of integer spin and a highly asymmetric electric field gradient provides for effective quenching of both homonuclear and heteronuclear spin-spin coupling [55]. Unfortunately, in the majority of NQR cases the spin is half-integer or the asymmetry is not small, so that T_2's are short. Then, the inevitable dead times after each pulse make it difficult to shorten the sequence pulse spacings enough to achieve the benefits of multiple pulse irradiation. A very promising way out of this difficulty is offered by cw

non-resonant irradiation of the spin system during the multiple pulse experiment. This "dressing" of the spin system with non-resonant photons may provide a very general method of drastically reducing unwanted spin-spin coupling.

The theory of non-resonant photon dressing has been discussed in Chapters 3 to 6 in this thesis.

In this chapter, we will report experimental observations of the effect of non-resonant irradiation on the linewidth of ^{14}N NQR for the case of symmetric electric field gradient. By limiting ourselves to axial symmetry, we are assured that spin-spin coupling is not already quenched [55].

7.2 Experimental Details

A Matec pulsed spectrometer was used to detect the NQR induction signals. A block diagram of the spectrometer is provided in Fig. 7.1. The frequency synthesizer, pulse generator and gated amplifier together are usually referred as the transmitter. The frequency synthesizer produces a continuous wave (cw) signal of near one volt r.m.s. at the nuclear resonance frequency. This sine-wave signal is fed into the gated amplifier and also into the receiver for phase sensitive detection. The gated amplifier has pulse power of one kilowatt and 50 Ω output impedance, it amplifies the cw signal with desired pulse sequence to about a few hundred volts. The impedance matching network steps up the voltage from the gated amplifier to a few thousand volts to the sample coil and isolates the sample and receiver from the amplifier during the time NQR signals are being detected. A single coil is used for both exciting and picking up signals from the nuclei. The excited nuclei induce a voltage of a few microvolts in the sample coil which is amplified by the receiver to the level of about one volt thus can easily be detected. The signal averager coherently adds up NQR signals and increases the signal-to-noise ratio by the square root of the number of coadditions. The recorded signal can be stored on disk for detailed computer analysis. The Matec pulsed spectrometer is capable to work in the frequency range of $\frac{1}{2}\ MHz$ to 100 MHz, in two transmitter stages.

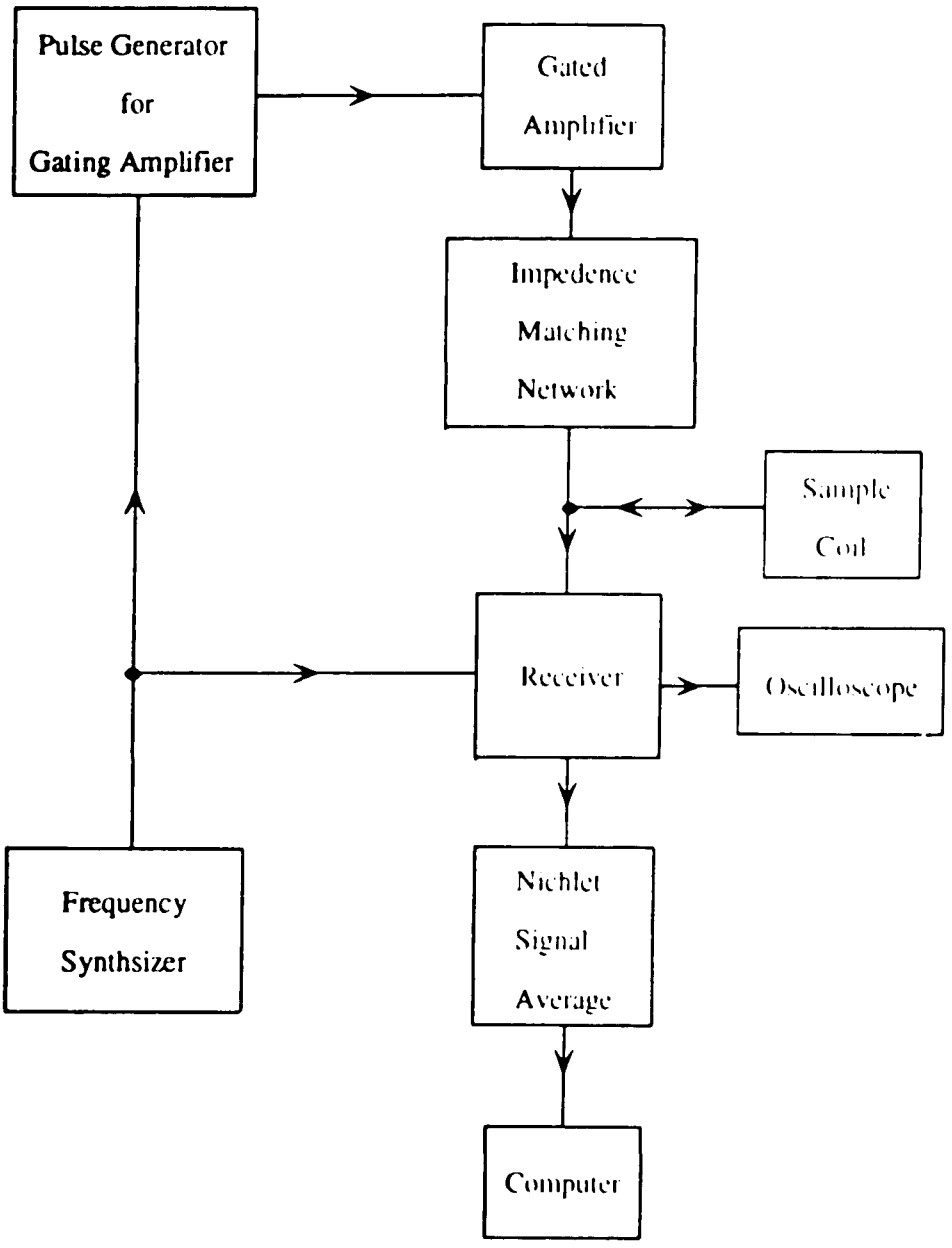

Figure 7.1: Block diagram of the Matec pulsed spectrometer.

The non-resonant irradiation is provided by home built equipment. An audio frequency sine wave generated by an oscillator is fed into a phase shifter and separated into two cw signals which are 90° out of phase to each other. These two signals are then amplified and send to two pairs of Helmholtz coils which are mutually perpendicular to each other in the $x - y$ plane. The magnetic field generated by these Helmholtz coils is circularly or linearly polarized in the $x - y$ plane depend on whether both or only one pair of helmhertz coils are energyzed.

The Helmholtz coils were wired up by No. 24 AGW enameled copper wire and were designed to have 8 Ω resistance to match the output of the amplifiers. The magnitude of the magnetic field in the center of the Helmholtz coils was calculated by the formular [56],

$$\frac{B}{i} = \frac{\mu_o R^2}{2(R^2 + z^2)^{\frac{3}{2}}} + \frac{\mu_o R^2}{2[R^2 + (L - z)^2]^{\frac{3}{2}}} \tag{7.1}$$

where B is the strength of magnetic field, i is the peak current, R is mean radius of the Helmholtz coils, L is distance between the pair of coils, and z is the distance measured along the symmetry axis of the coils. For the center of the pair of coils, $z = \frac{L}{2}$.

The magnitude of the field produced between the Helmholtz coils was also calibrated by means of Faraday's law of induction. A search coil of known area and turns is placed in the center of the Helmholtz coil and the induced voltage in the coil is monitored by an oscilloscope. Thus, the relation between the current through the Helmholtz coils and the field produced by the coils can be obtained experimentally. The tested value of B/i matches quite well with the value calculated using Eq. 7.1. During the experiment, the magnitude of the dressing field is controlled by the current through the coils.

The photon dressed NQR experiments were performed at a temperature of 77 K provided by a glass dewar positioned in the middle of the Helmholtz coils and holding liquid nitrogen. The liquid nitrogen bath prevented the sample from heating up by Joule's effect. The Helmholtz coils, the dewar and the sample are shielded by a metal

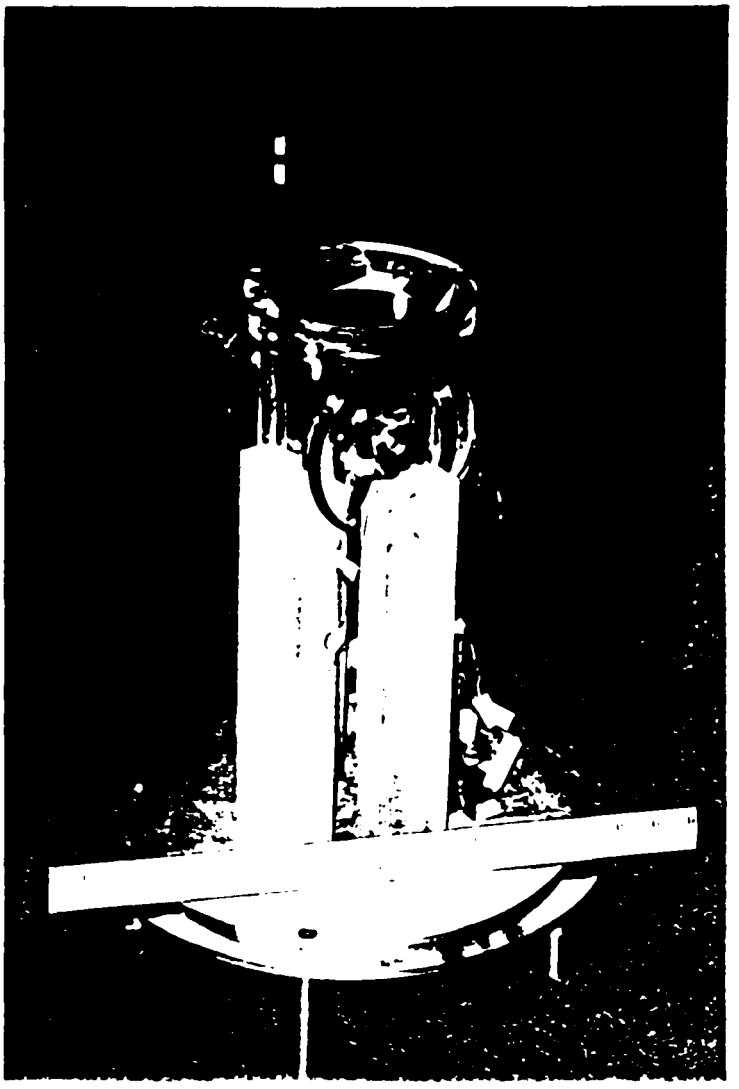

Figure 7.2: (a) Photographs of the dressing apparatus, the pairs of Helmholtz coils, the search coil, the plastic pillar, and the metal base holder.

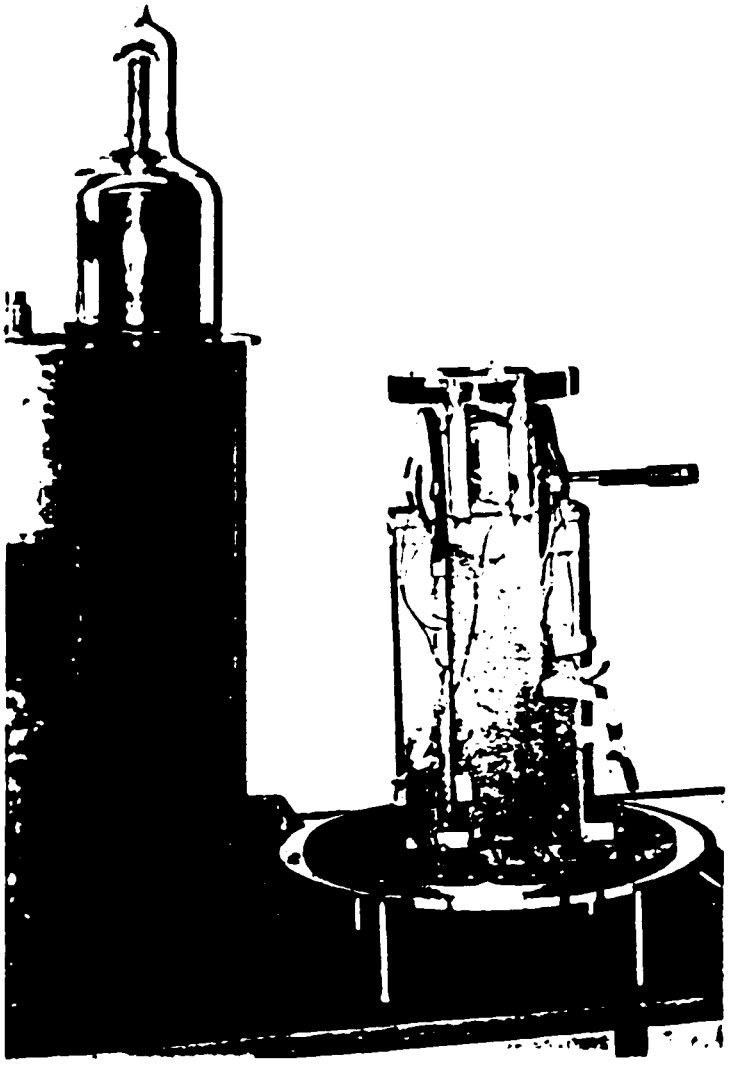

Figure 7.2: (b) Photographs of the dressing apparatus, left, the metal cylinder and the glass dewar sitting on the top, right, the Helmholtz coils. In front of the plastic pillar, you can see the capacitances and resistances. During the experiment, the glass dewar is placed on the plastic ring holder and the neck of the dewar is positioned in the center of the coils. The sample coil hangs vertically in the neck of the dewar. The whole apparatus is converted by the metallic cylindrical shield.

cylinder as shown in the photograph, Fig. 7.2, to avoid interference with the transmitter's frequency. The actual circuit of the Helmholtz coils includes a resistance R and a capacitor C in series resonance. The capacitors were selected technically to have both pair of coils resonant at exactly the same frequency. The current through the coils was measured by monitoring the voltage across a precision resistance. The sample coil is placed vertically in the neck of the dewar. Due to the limitation of the power of the amplifiers (200 W), the maximum field that can be produced is only 25 G without arching.

7.3 Experimental Results and Discussion

Circularly polarized non-resonant irradiation of frequency $\frac{\omega}{2\pi} = 11.1\ kHz$ and peak magnitude H_2 up to 24 G was applied to NQR samples, using the geometrical arrangement mentioned in the previous section. Three substances, all with zero asymmetry parameter and in the powdered crystal form, were studied at 77 K: Hexamethylenetetramine (HMT), Triethylenediamine (TED), and Trimethylamine (TMA). The molecular structure of these three substances are shown schematically in Fig. 7.3. In all of these three samples nitrogen nuclei have protons as their near neighbours. The relevant NQR parameters are collected in Table 7.1. In all cases the lineshapes were homogeneously broadened, evidenced by our inability to obtain spin echoes.

The effect of non-resonant irradiation on TMA is shown in Fig. 7.4. Fig. 7.4(a) is the free induction decay (FID) obtained without non-resonant irradiation. The radio-frequency transmitter was offset by 3.045 kHz above exact resonance, resulting in a characteristic FID pattern. The FID is not symmetric about the time-axis since the receiver was set for a mixture of phase sensitive and amplitude detection. Numerical simulations reveal that the FID is exponential with a characteristic time $T_2^* = 0.90$ $msec$. Fig. 7.4(b) and 7.4(c) show the FID obtained under identical circumstances but with a circularly polarized 11.1 kHz dressing field of peak amplitude $H_2 = 12.8$ and 24.0 G, respectively. The FID is visibly lengthened, indicating line narrowing.

Substances	ν_Q [kHz]	e^2qQ/h [kHz]	η
Trimethylamine (TMA) [64]	3895.4	5193.9	0
Triethylenediamine (TED) [65]	3693.5	4924.7	0
Hexamethylenediamine (HMT) [66]	3407.6	4543.4	0
HMT·3 phenol [58] (η = 0 site only)	3499.3	4665.7	0

Table 7.1: NQR parameters at 77 K for materials discussed in the text. ν_Q is the NQR resonance frequency, e^2qQ/h is the quadrupole coupling constant, and η is the asymmetry parameter of the electric field gradient tensor.

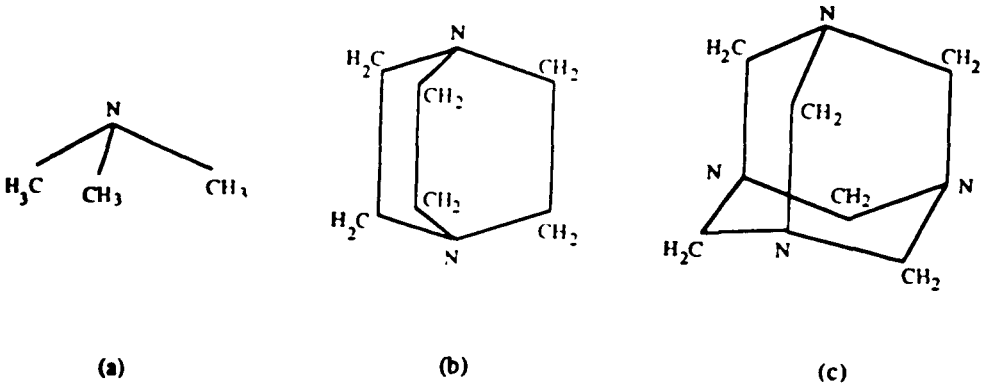

Figure 7.3: Molecular structure of (a) Trimethylamine (TMA); (b) Triethylenediamine (TED); (c) Hexamethylenetetramine (HMT).

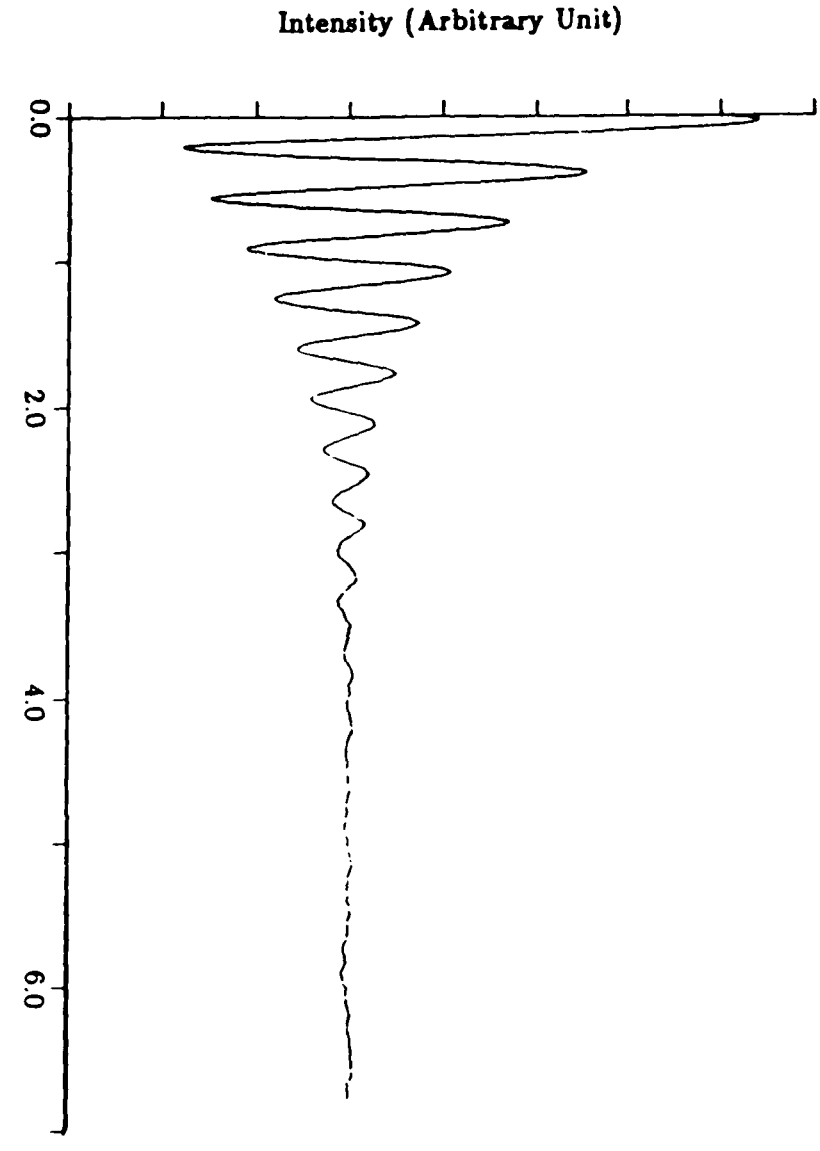

Figure 7.4: (a) FID signal of ^{14}N NQR in TMA when the dressing field $H_2 = 0$.

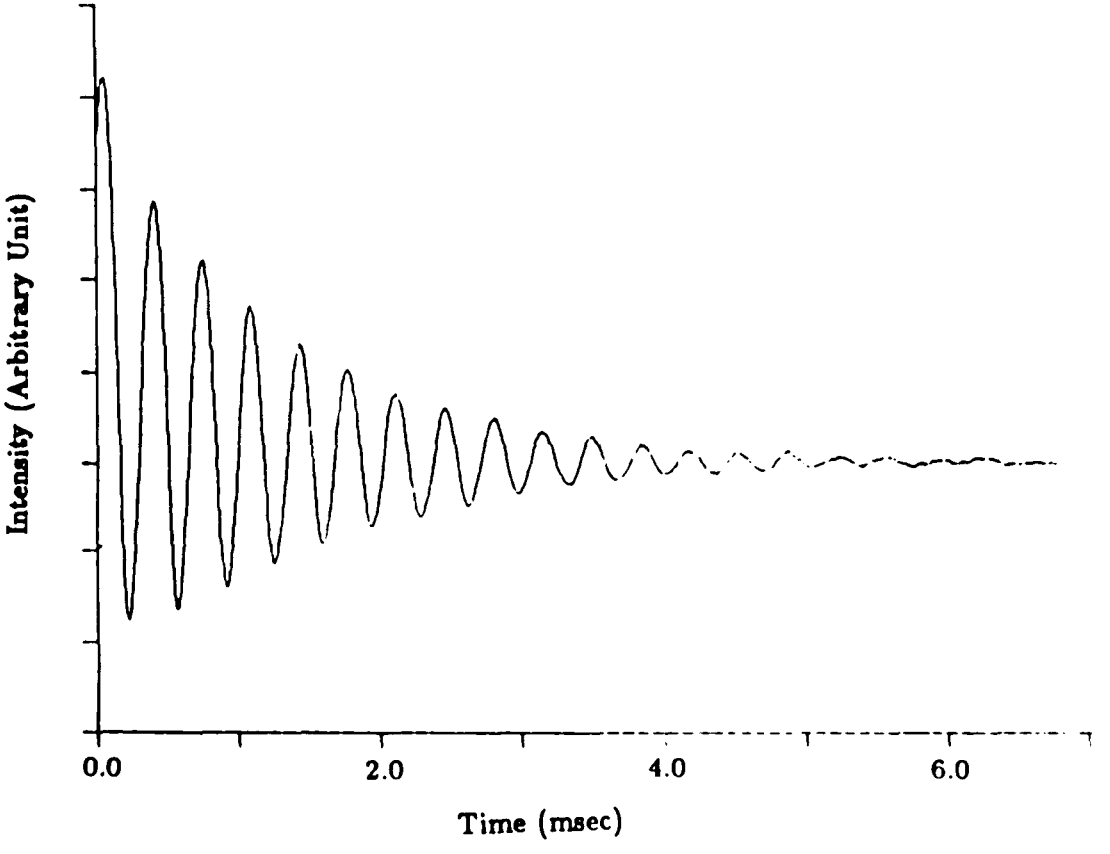

Figure 7.4: (b) FID signal of ^{14}N NQR in TMA when the dressing field $H_2 = 12.8\ G$.

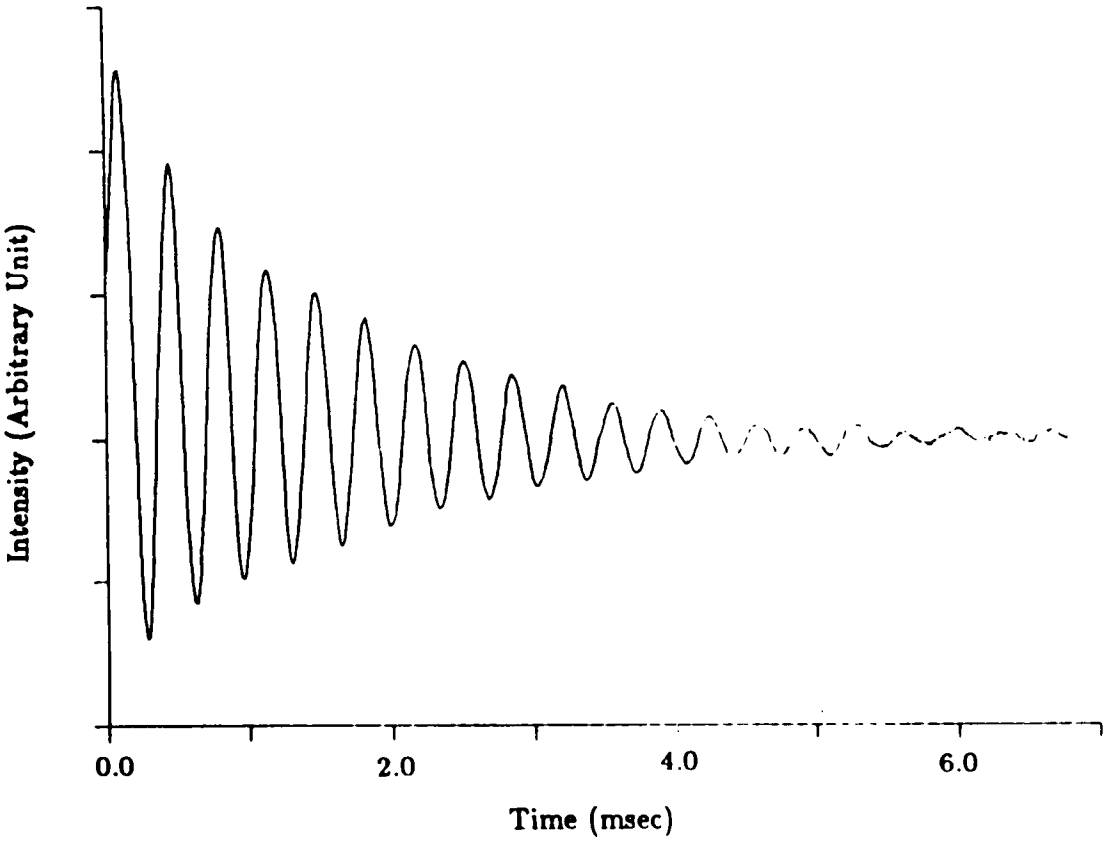

Figure 7.4: (c) FID signal of ^{14}N NQR in TMA when the dressing field $H_2 = 24.0\ G$.

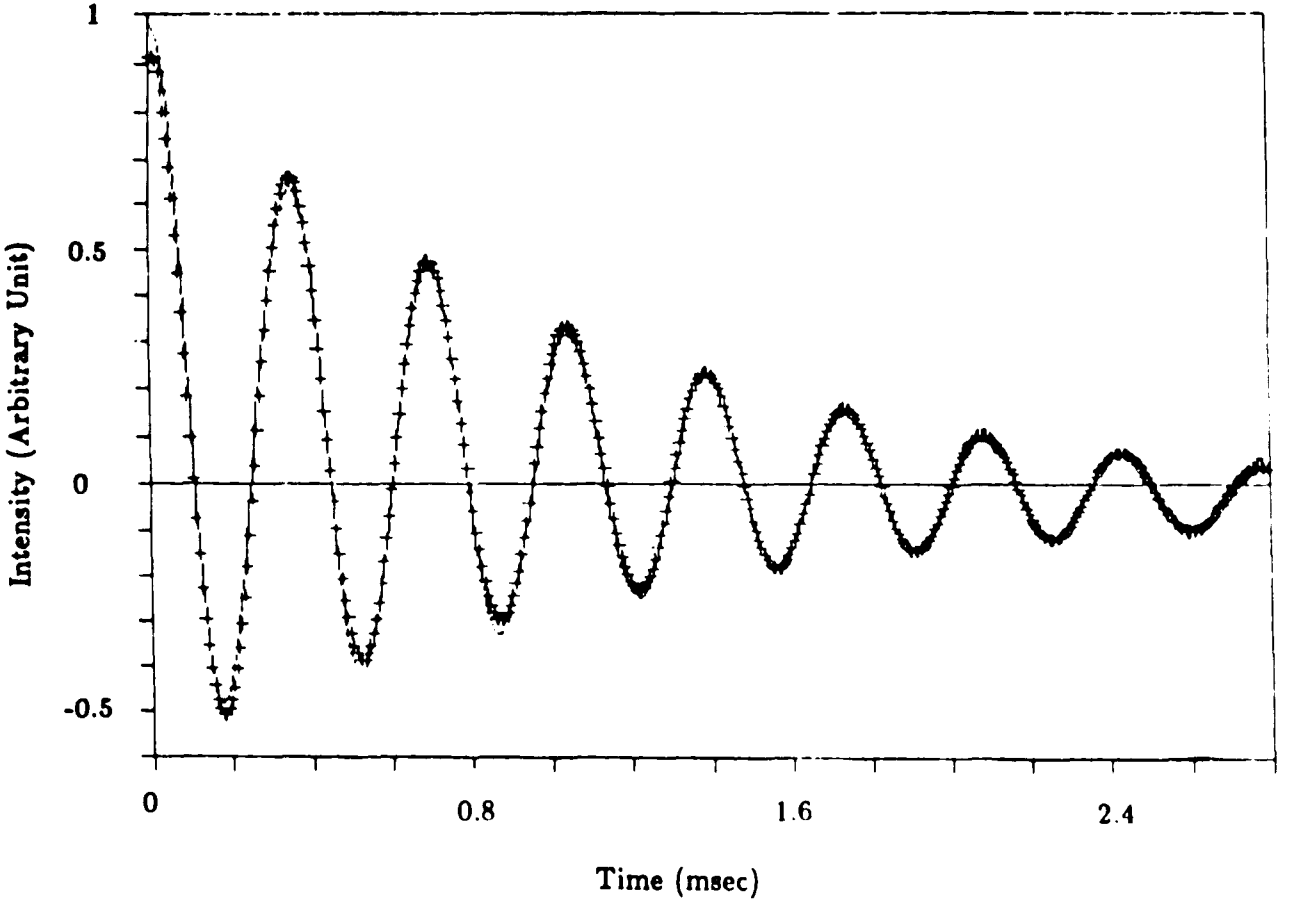

Figure 7.5: TMA FID signal when the dressing field H_2 = 6.4 G (dashed curve) and its numerical fit (cross dots).

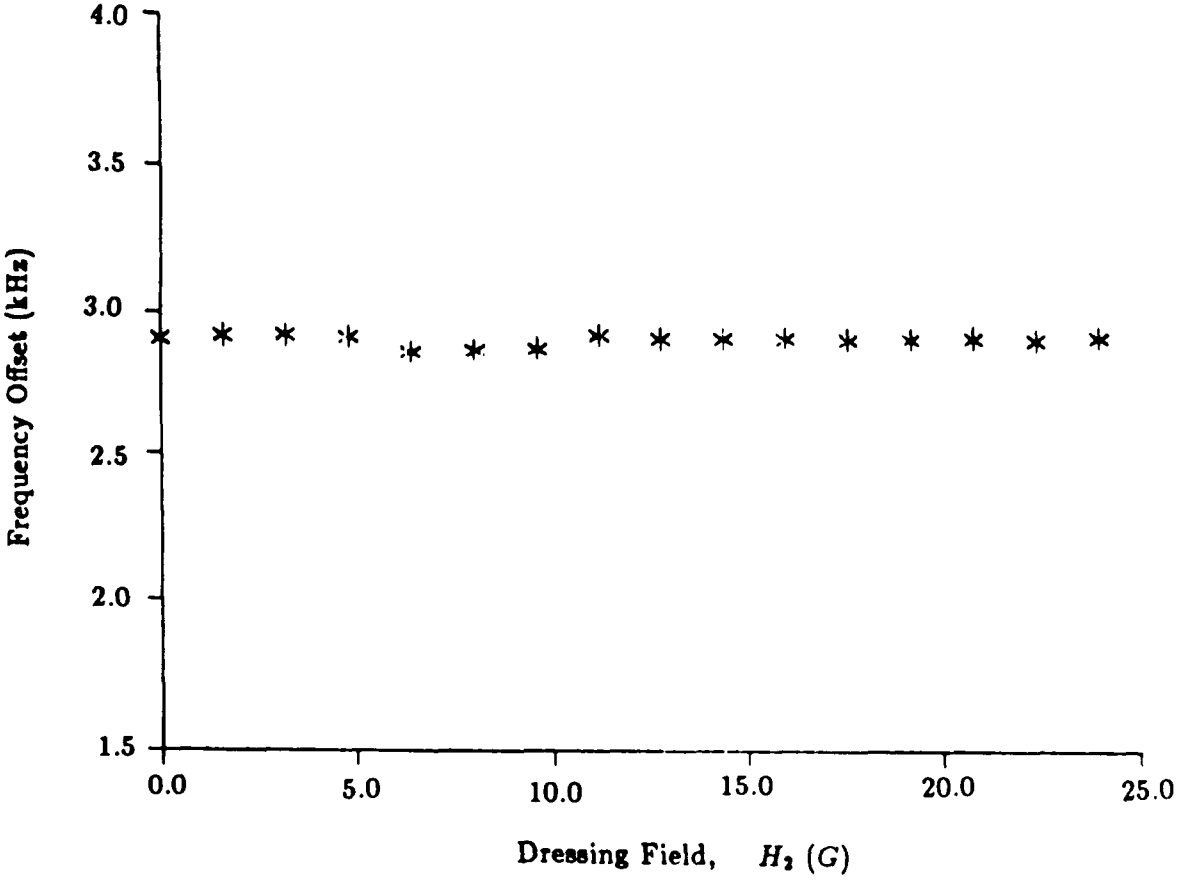

Figure 7.6: Frequency offset of ^{14}N NQR FID signal in TMA versus dressing field peak amplitude H_2. No frequency shift is observed.

Data were collected with a Nicolet signal averager for sixteen values of H_2 between zero and 24 G, i.e., $\gamma H_2/2\pi$ up to 100 kHz for protons. In each case, numerical fits showed excellent agreement with a Lorenzian lineshape. Fig. 7.5 shows how well an exponentially decaying function fits the FID signal of TMA when $H_2 = 6.4\ G$. In Fig. 7.6 the ^{14}N NQR frequency obtained by numerical fitting the FID data is plotted for increasing value of H_2. Within experimental error, the NQR lines are not shifted at all by fields of up to 24 G. Recalling the results of the theory of dressed NQR, section 5.3, a dressing field of 24 G corresponds to $\frac{\omega_2}{\omega} = 0.66$ for nitrogen, which can cause NQR frequency shift of 11.5 Hz. Such a small amount of shift is not observable in our experiment. Thus, experiment and theory are consistent.

Finally, the characteristic FID decay time T_2^*, obtained from numerical fitting of the FID data, is plotted in Fig. 7.7. A monotonic increase is observed, with no discernible features at the crossings or anticrossings of the dressed proton energy diagram. This is consistent with the theory developed in Chapter 6.

The increase of the FID decay time T_2^* can be explained in the following way. Suppose the line broadening is due to the dipolar interaction between nitrogen and protons. The local field due to a proton (spin I) on nitrogen (spin s) is expressed by Eq. 2.17. As described in Chapter 6, the effect of photon dressing causes protons to oscillate between $|+\frac{1}{2}>$ and $|-\frac{1}{2}>$ states, so that $\vec{\mu}_I$ and $\vec{H}_{loc}$ changes sign as it oscillates. The proton reorientation rate is bigger than the dressing frequency ω, much larger than the linewidth of ^{14}N and ^1H. So that the local field due to proton is averaged to a small value, and the line is narrowed.

For TED and HMT, however, the results are different. As first reported by Colligiani and Ambrosetti [57] both TED and HMT have structure to their NQR lineshape: each of which appears to be a partially resolved asymmetric doublet. The structure, presumably dipolar in origin, is revealed for the case of TED at 77 K by the characteristic beat pattern of the FID shown in Fig. 7.8(a). Figs. 7.8(b) and (c) show the NQR FID obtained when an 11.1 kHz dressing field of peak magnitude H_2 is applied to TED, with $H_2 = 12.8\ G$ and 25.6 G, respectively. Single channel Fourier transform performed

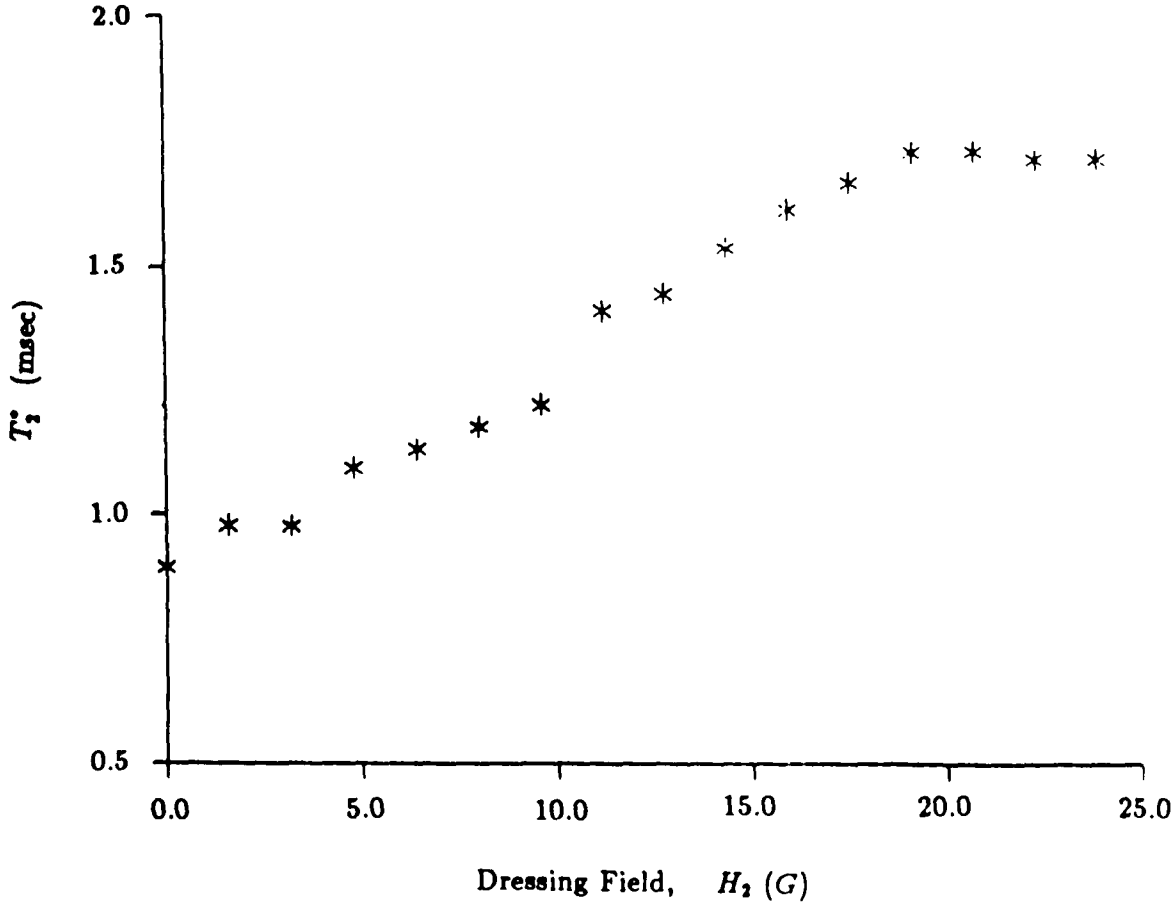

Figure 7.7: The inverse linewidth parameter T_2^* obtained by numerical fit of NQR FID data such as shown in Fig. 7.4 versus dressing field peak amplitude H_2

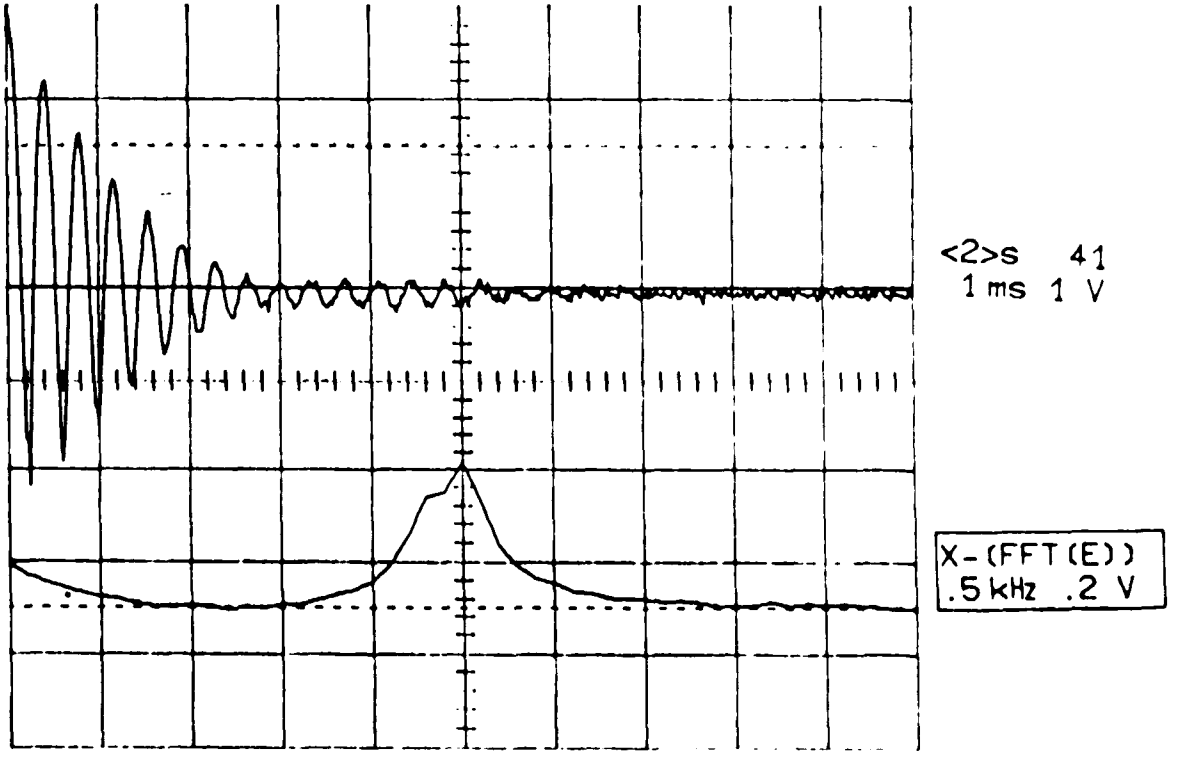

Figure 7.8: FID and its FT of ^{14}N NQR in TED at 77 K. (a) No dressing field.

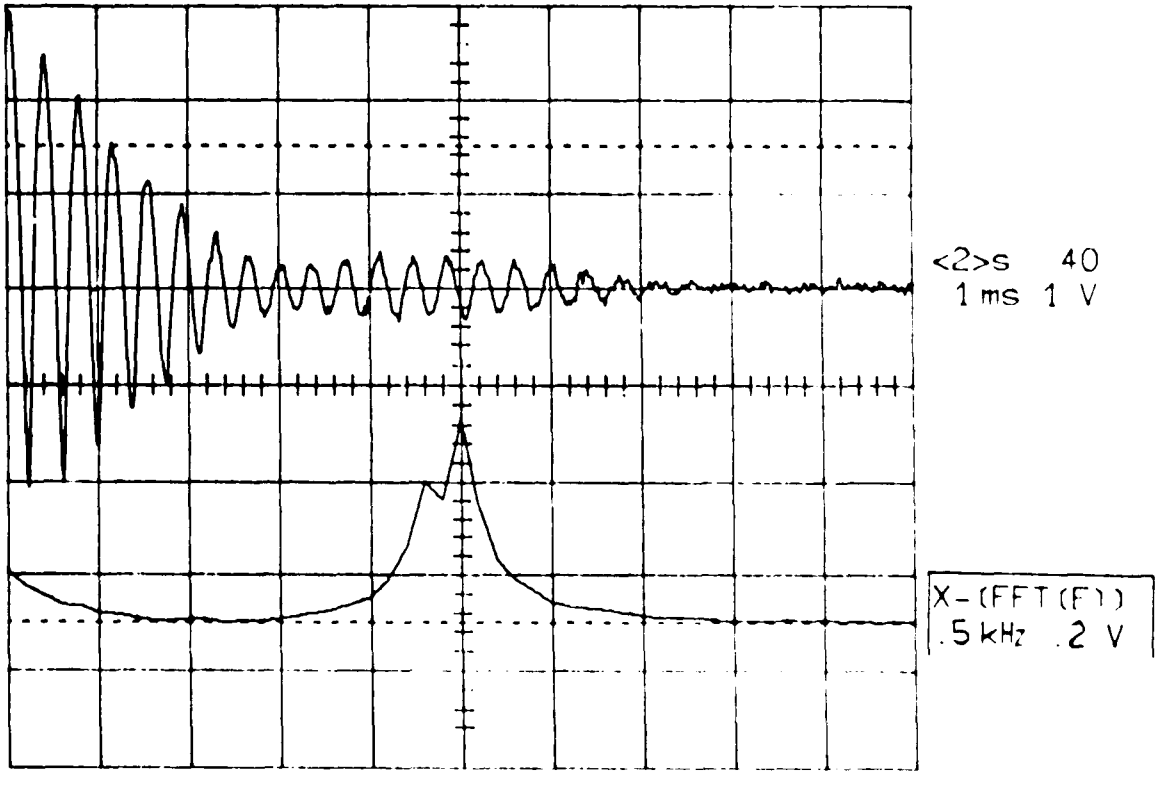

Figure 7.8: FID and its FT of ^{14}N NQR in TED at 77 K. (b) Dressing field of 11.1 kHz and peak magnitude $H_2 = 12.8\ G$.

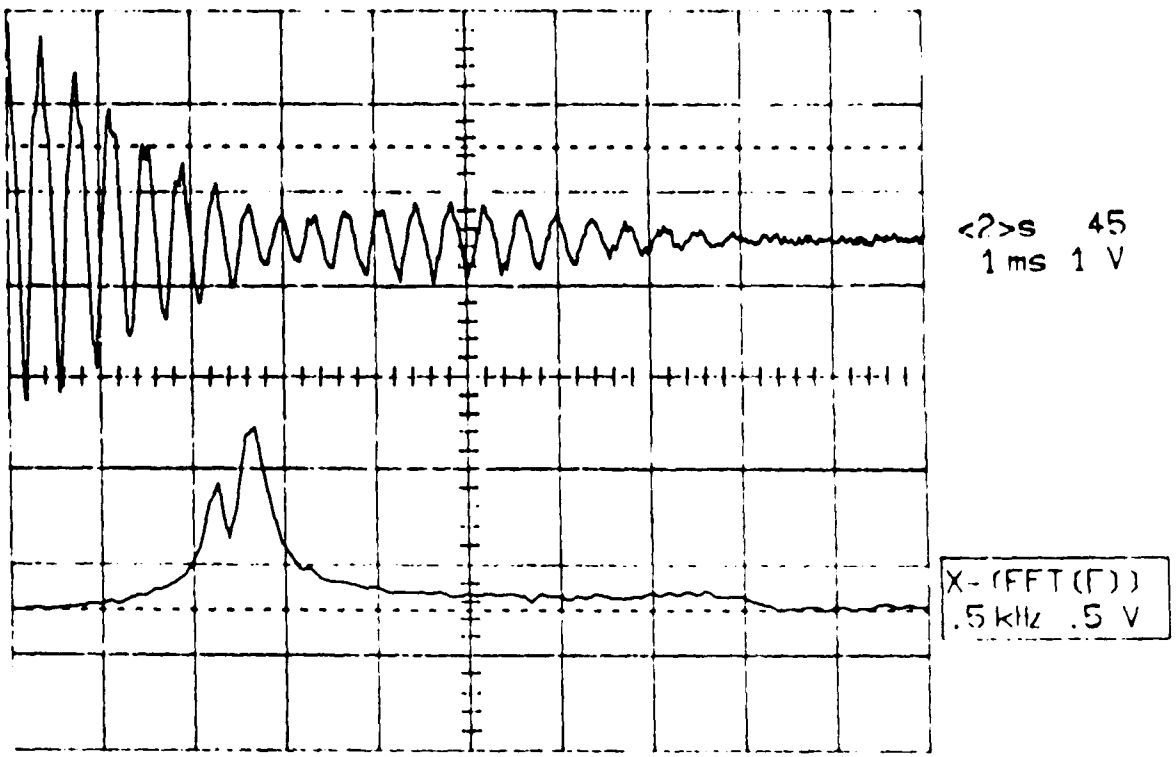

Figure 7.8: FID and its FT of ^{14}N NQR in TED at 77 K. (c) Dressing field of 11.1 kHz and peak magnitude $H_2 = 25.6\ G$.

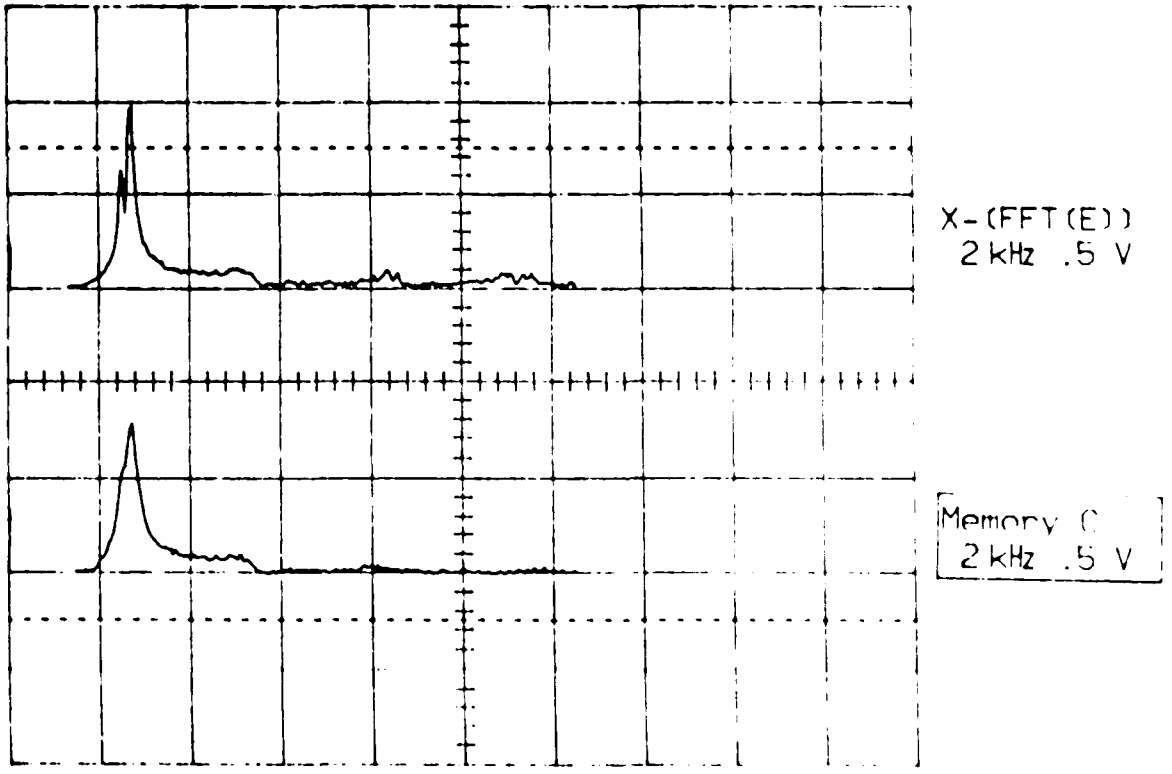

Figure 7.9: Lineshapes of TED when dressing field $H_2 = 0$ (bottom curve) and $H_2 = 25.6\ G$ (top curve).

by a LeCroy signal averager of the FID are shown on the bottom of these Figures. As H_2 is increased from zero to 25.6 G, the unresolved line broadening decreases, which is in agreement with observations in TMA reported above. Fig. 7.9 is the Fourier transforms of the FID when $H_2 = 0$ and 25.6 G, the linenarrowing can be seen clearly. However, the amount of the linewidth decrease in TED is not as much as that in TMA, indicating that the degree of dipolar broadening in TED is smaller. On the other hand, the separation of the resolved splitting does not appear to change at all. The splitting was measured to be about 200 Hz regardless the strength of the dressing field, within experimental error, so that the result of the non-resonant irradiation is to reveal in progressively sharper resolution the underlying asymmetric doublet structure.

Analogous measurements were performed on polycrystalline HMT at 77 K and in the $\eta = 0$ site [58] of the hydrogen-bonded complex, HMT·3phenol. These two crystals gave indistinguishably similar lineshapes for the ^{14}N NQR, an asymmetric doublet similar to the one observed in TED. This observation strengthens the assumption for dipolar origin of the line structure, since HMT and TED share the same number and arrangement of nearest neighbor protons. This time, however, no effect whatever was observed as H_2 was increased from zero to 25 G peak. Neither the unresolved broadening nor the resolved asymmetric doublet was affected, within our experimental precision.

The fact that the non- resonant irradiation did not affect the doublet of both TED and HMT, lead us to rethink whether the assumption of dipolar origin could be correct. Recently, the order of splitting in HMT due to dipolar interaction was theoretically calculated by Galbiati [59]. The result shows that the order of splitting due to dipolar is only 30 Hz, much smaller than the actually observed splitting of 200 Hz. This brings matters back into consistency with our results, which clearly show that the resolved asymmetric doublet structure is not dipolar in origin. Das and Hahn [38] discussed the possible line splitting in solid NQR due to the indirect spin-spin interaction which originates from the chemical bond between them and which may not be affected by photon dressing. The J interaction can lead to an appreciable fine splitting of the quadrupole spectra, if its short-range effect is sufficiently strong to overcome the direct

dipole-dipole interaction. Some examples of splitting of pure quadrupole spectra due to J interaction are given in the literature [60, 61]. However, little study of J interaction has been done here, and the above speculation is merely a tentative assumption at this time.

The selective efficacy of non-resonant irradiation in reducing lineshape broadening leads us to consider thermal effects. Certainly, line broadening due to hindered reorientations about the molecular trigonal axis, known to occur in both HMT [62] and TED [63], should not be directly affected by proton decoupling. For HMT, however, the correlation time for these motions was reliably [62] measured to be longer than one second at 77 K; so it would appear that thermal motions can not account for the observed linewidth. A satisfactory explanation for the observed difference in TED and HMT is still missing.

In all of the samples we studied by photon dressing side band lines did appear. Figs. 7.10 and 7.11 show the FIDs and their Fourier transforms for TMA and TED at a dressing frequency 6.38 kHz respectively. In both cases, the transmitter frequency was offset at 6.38 kHz exactly to avoid the folding problem in single channel FT. In both figures, the second small peak located at 6.38 kHz to the right side of the big peak is sideband transition of $\Delta n = 1$.

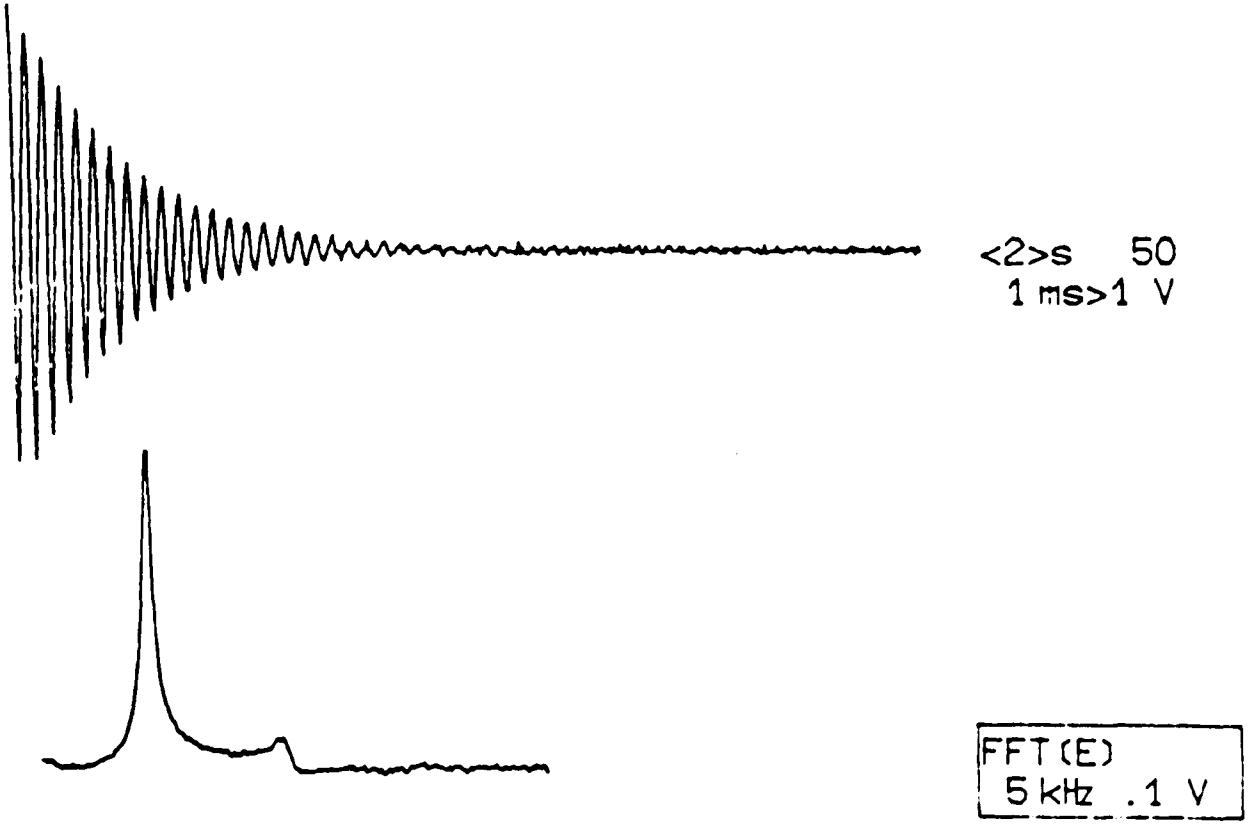

Figure 7.10: FID and its FT of ^{14}N NQR in TMA at 77 K when dressing field of 6.38 kHz and peak magnitude H_2 = 9.6 G. The second peak is the sideband transition of $\Delta n = 1$. The frequency difference between the $1st$ and $2nd$ peak is 6.38 kHz.

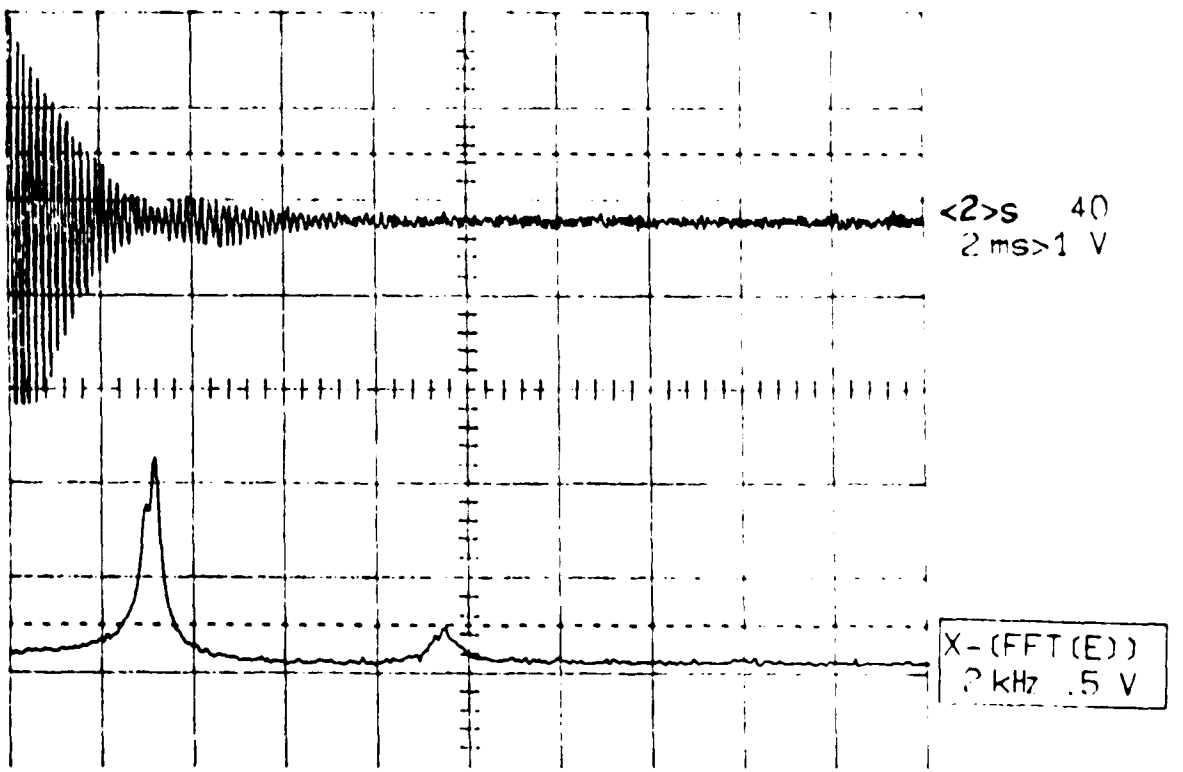

Figure 7.11: FID and its FT of ^{14}N NQR in TED at 77 K when dressing field of 6.38 kHz and peak magnitude H_2 = 14.4 G. The second peak located at 6.38 kHz right to the first peak is the sideband transition of $\Delta n = 1$.

Chapter 8

Effects of Annealing and Hydrogenation on Short-Range Order in Amorphous III-V Compounds

8.1 Introduction

The relationship between intrinsic structural disorder and material properties is the central subject in the study of amorphous tetragonally bonded semiconductors. Besides dangling bonds and wrong bonds which are analogous to vacancies and anti-site defects in crystals, amorphous III-V semiconductors are expected to have configurational disorder which refers to departure from tetrahedral arrangement of the diamond cubic structure. X-ray and electron diffraction radial distribution function (RDF) measurements on $\alpha - Ge$ and $\alpha - Si$ show that the short range tetrahedral coordination is preserved, with bond length differing from that of crystals by at most a few percent and bond angle distorted by about $\pm 10^{\circ}$ off the tetrahedral angle of 109.5° [67]. The overall similarity of amorphous III-V compounds' X-ray RDF measurements [68] to those of $\alpha - Ge$ suggest that they retain the same tetrahedral short range order. Nuclear Magnetic Resonance (NMR) studies on $\alpha - GaAs$, give evidence that the Ga and As nuclei are still fourfold coordinated [69], and estimate a bond-angle disorder of $\pm 9^{\circ}$ based on experimentally determined nuclear quadrupole coupling constants [70], which are consistent with those obtained by X-ray RDF measurements. However, the degree of local structural distortions from perfect tetrahedral coordination, therefore the optical and electronic properties of the material are found to be influenced by sample deposition technique and deposition conditions [71, 72, 73].

Amorphous III-V semiconductors prepared by same rf-sputtering but different substrates have been studied by NMR techniques. The effects of isochronal annealing on NMR linewidth have been studied in an attempt to observe possible structural rearrangements which may occur prior to crystallization. Additional interest in annealing behavior of amorphous III-V compounds is generated by its relevance to modern device technology which involved doping of crystalline III-V layers by ion implantation and then annealing the amorphisized layers to crystallization. The results suggest that sample preparation techniques, including choice of substrate play a major role in the resulting microstructure.

8.2 Experimental Detail

The samples which have been studied are $\alpha - GaP$, $\alpha - GaAs$, and $\alpha - GaAs:H$. Two $\alpha - GaAs$ samples have been studied. One prepared on Si/SiO_2 substrate labeled as $\alpha - GaAs(I)$ and the other by alkali-halide substrate, labeled as $\alpha - GaAs(II)$. All of these samples were deposited by rf-sputtering in Ar plasma and were measured to be 40μ thick films. Where $\alpha - GaP$ and $\alpha - GaAs(I)$ were grown on Si/SiO_2 wafer substrate, with substrate temperature of $50^\circ\ C$. While $\alpha - GaAs(II)$ and $\alpha - GaAs:H$, were grown on alkali-halide substrate, with substrate temperature of $20^\circ\ C$.

The NMR measurements were performed with a Novex pulsed spectrometer and a Cryomagnet System superconducting magnet with field strength 7.2 Tesla. ^{69}Ga and ^{71}Ga NMR were studied in samples prepared on Si/SiO_2 and alkali-halide subtrates respectively. The natural abundance and NMR frequency at 7.2 Tesla of these two nuclei are collected in table 8.1. To avoid dead time problem, solid spin echoes [34] following a $90^\circ - \tau - 90^\circ$ and $270^\circ - \tau - 270^\circ$ pulse sequence were utilized to obtain the lineshapes of ^{69}Ga and ^{71}Ga respectively. For ^{69}Ga nuclei, the spectrum were obtained by Fourier transforming the quadrature detected spin echo signal. While for ^{71}Ga, since the lines were too broad to be irradiated completely, a point-by-point echo intensity versus transmitter's off-resonance frequency method was used to obtain the

Nuclear	Spin I ($\hbar$)	Natural abundance (%)	ν_o at 7.2 Tesla (MHz)	Quadrupole moment [76] ($e \times 10^{-24}\ cm^2$)	Magnetic moment μ [77] (Bohr magneton)
^{69}Ga	3/2	60.2	73.9512	0.2318	2.0108
^{71}Ga	3/2	39.8	93.4848	0.1461	2.5549

Table 8.1: NMR parameters of ^{69}Ga and ^{71}Ga.

lineshape. Isochronal annealing was performed with a conventional oven for 12 minutes for $\alpha - GaP$ and 10 minutes for $\alpha - GaAs(II)$ and $\alpha - GaAs{:}H$ at each temperature.

8.3 Experimental Results and Discussion

Nuclear Magnetic Resonance can be used as a sensitive tool to probe short-range structure because the NMR lineshape is sensitive to short-range dipolar and quadrupolar interactions. For perfect crystalline III-V semiconductors, their structural units have perfect tetrahedral symmetry, thus, the electric field gradient (efg) at the nuclear site is always zero, no quadrupole interaction should be present, so the lines are relatively narrow [32], being dominated by dipole-dipole interactions. ^{69}Ga and ^{71}Ga nuclei both have large quadrupole moments. Small changes from perfect tetrahedral symmetry due to charged defects or/and bond length or bond angle distortions can cause the microscopic electric field gradient at the nuclear site no longer to be zero. Thus, a non-zero quadrupole interaction will be present, and the lines are broadened. It has been shown that the NMR linewidths in crystalline III-V compounds is 1st-order quadrupole broadened, and are arise from charged defects [74, 75]. Whereas for amorphous III-V semiconductors, like $\alpha - GaAs$, the lines are even broader, only the central $\frac{1}{2} \rightarrow -\frac{1}{2}$ transition is observed, and the quadrupole interaction is of second order arising from configurational distortions from tetrahedral symmetry [69].

Thus, we can say that the broader the NMR linewidth, the more disordered is the sample microstructure.

The linewidths of all the samples which have been studied are much broader than those of the corresponding crystalline compounds, which are about 4-5 kHz. For all of the amorphous samples, only one featureless echo was obtained which was $2nd$ order quadrupole broadened. As pointed by Abragam [32], for $2nd$ order quadrupole interaction, the 90° pulse width of the central transition is reduced by a factor of $(I+\frac{1}{2})$. Both ^{69}Ga and ^{71}Ga are spin $\frac{3}{2}$ nuclei. The 90° pulse widths in these samples were checked to be half of those of crystal samples, thus simply verifying the $2nd$ order quadrupole broadening.

For samples prepared on Si/SiO_2 substrate, the ^{69}Ga full linewidth at half maximum (FWHM) at room temperature in $\alpha - GaAs(I)$ is typically a factor of three as large as that in $\alpha - GaP$, 24 kHz, thus indicating a substantially greater degree of bond-angle disorder in the former. For $\alpha - GaAs(II)$ prepared on alkli-halide substrate, ^{71}Ga FWHM at room temperature (the only exception of ^{71}Ga which is also obtained from the FT method) is 109 kHz. Recalling the NMR theory [37, 75] discussed in Section 2.7, the linewidth of second order quadrupole broadened central transition powder pattern is proportional to $\frac{\nu_Q^2}{\nu_o}$, where $\nu_o = \frac{\gamma H_o}{2\pi}$ is the unperturbed NMR frequency, and $\nu_Q = \frac{3e^2qQ}{2I(2I-1)h}$ is the NQR frequency. Assume the electrical field gradient eq on ^{69}Ga and ^{71}Ga is the same, then the linewidth is proportional to $\frac{Q^2}{\gamma}$. The magnetic and quadrupole moments for ^{69}Ga and ^{71}Ga are listed in Table 8.1. It is clear that if ^{69}Ga NMR were studied in $\alpha - GaAs(II)$, the corresponding linewidth would be $109 \cdot \frac{Q_{69}^2 \cdot \gamma_{71}}{Q_{71}^2 \cdot \gamma_{69}}$ kHz, which equals to 3.4 times 109 kHz. This means that the NMR linewidth of $\alpha - GaAs(II)$ is actually much much broader than that of $\alpha - GaAs(I)$, which indicates the influence of the sample preparation condition on the degree of distortion.

The presence of hydrogen does not seem to affect the degree of disorder, on the other hand. Fig. 8.1 is the lineshape of the ^{71}Ga NMR absorption signals in $\alpha - GaAs(II)$ and $\alpha - GaAs:H$ prepared on alkli-halide substrates at room temperature, obtained by echo height versus transmitter frequency. It is interesting to note that these two

lineshapes are identical, the presence of 10 % hydrogen does not influence the lineshape at all.

Isochronal annealing experiments were performed on $\alpha - GaP$, $\alpha - GaAs(II)$, and $\alpha - GaAs:H$. Fig. 8.2 shows ^{69}Ga NMR FWHM in $\alpha - GaP$ as a function of annealing temperature (12 minutes annealing). The lines gradually narrow starting at about 200° C and crystallize completely at about 600° C. By contrast, $\alpha - GaAs(II)$ and $\alpha - GaAs:H$ prepared on alkli-halide substrates exhibit a different annealing behavior. Fig. 8.3 shows ^{71}Ga NMR FWHM in $\alpha - GaAs(II)$ as a function of annealing temperature (10 minutes annealing). The linewidth shows an initial narrowing, (this indicates an initial ordering) at relatively low temperature of about 100° C, followed by almost no further activity until crystallization at much lower temperature of about 400° C. Fig. 8.4 shows the same feature for ^{71}Ga in $\alpha - GaAs:H$. The similarity of Figs. 8.3 and 8.4 indicates that the presence of hydrogen does not effect the annealing behavior either.

Optical measurements on hydrogenated $\alpha - Ge$ showed that hydrogen can affect the optical edge by decreasing network disorder [78]. Transport measurements indicate that the incorporation of hydrogen passivates defects in $\alpha - GaAs$ [72, 73]. Susanne M. Lee et al. reported that $\alpha - Si:H$ films prepared by glow-discharge deposition with or without the addition of hydrogen or deuterium to the source gas, SiH_4, contained different amount of hydrogen, presented no differences between their optical and electronic properties but a number of structural differences. Moreover, their optoelectronic properties revealed differences upon anneal to elevated temperatures [79]. However, our results here is somewhat different from these reports.

Fig. 8.5 shows the lineshapes of ^{71}Ga in $\alpha - GaAs(II)$ at annealing temperatures 375° C and 400° C. The sudden sharpness at 400° C indicates clearly that the sample crystallization is completed at temperatures between 375° C and 400° C. Shortening the annealing temperature step could have located the crystallization temperature more precisely.

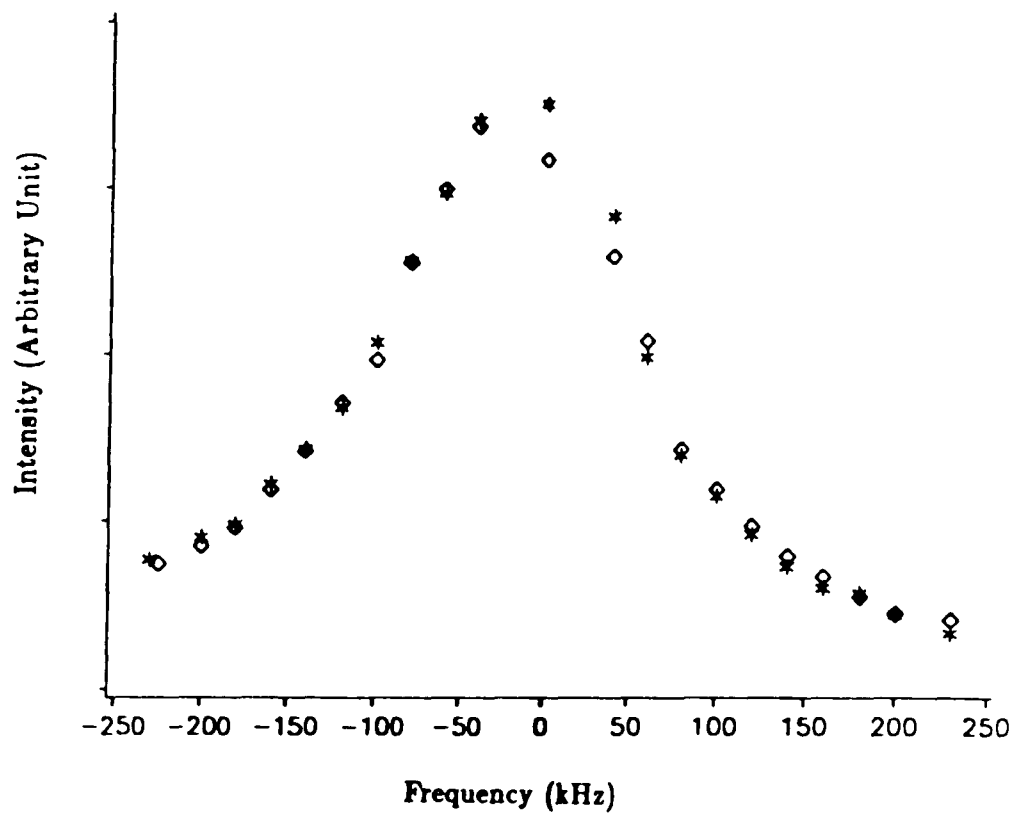

Figure 8.1: Lineshapes of ^{71}Ga at room temperature in samples prepared on alkli-halide substrate. "*" is for $\alpha - GaAs:H$ and "□" for $\alpha - GaAs$.

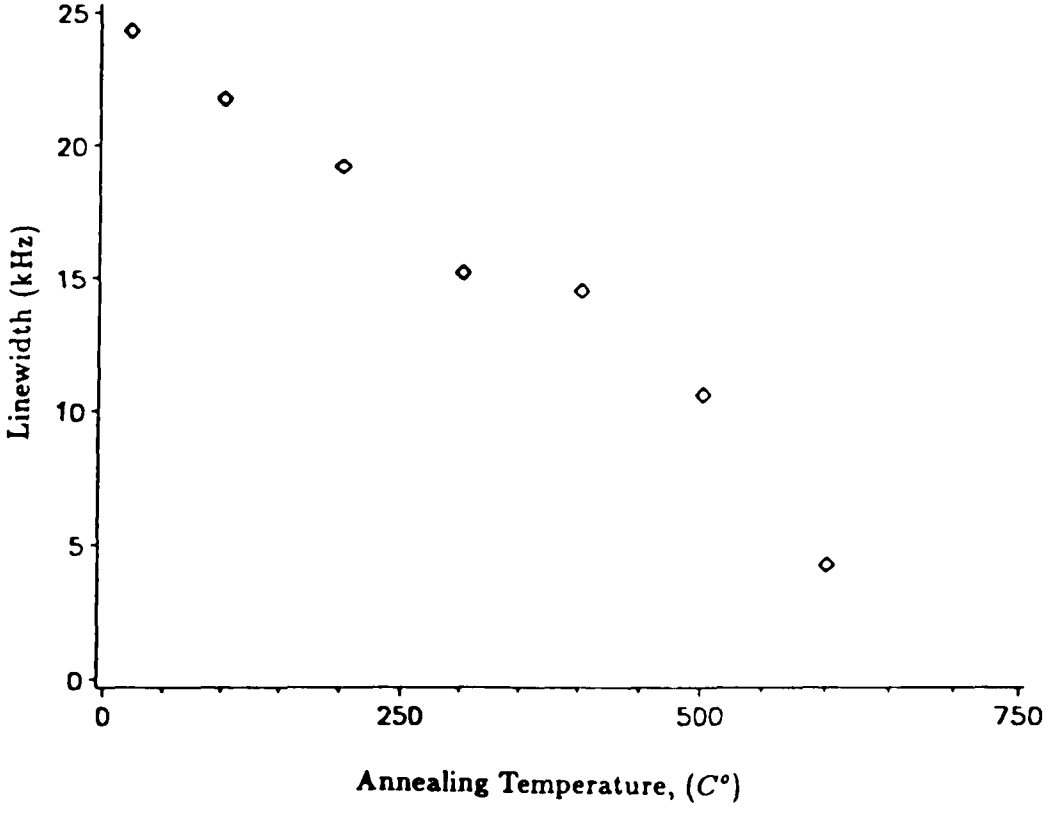

Figure 8.2: ^{69}Ga NMR FWHM in $\alpha - GaP$ prepared on Si/SiO_2 substrate as function of annealing temperature.

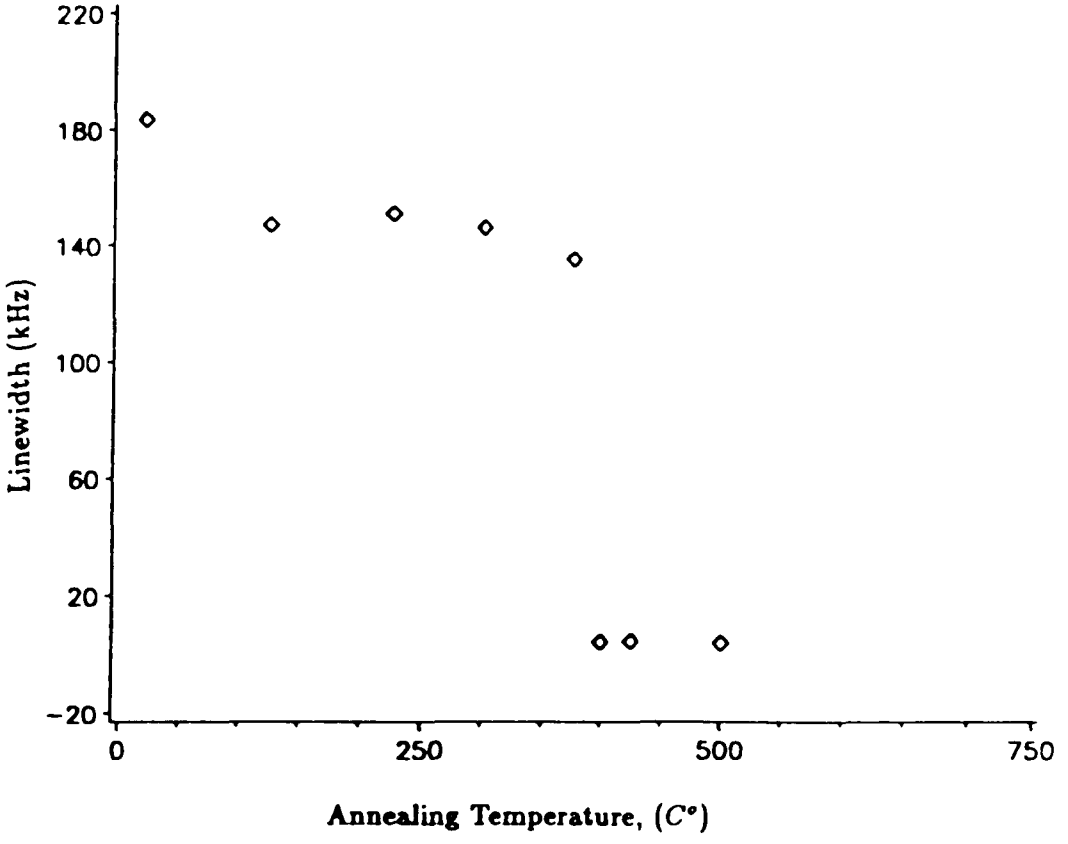

Figure 8.3: ^{71}Ga NMR FWHM in $\alpha - GaAs$ prepared on alkli-halide substrate as function of annealing temperature.

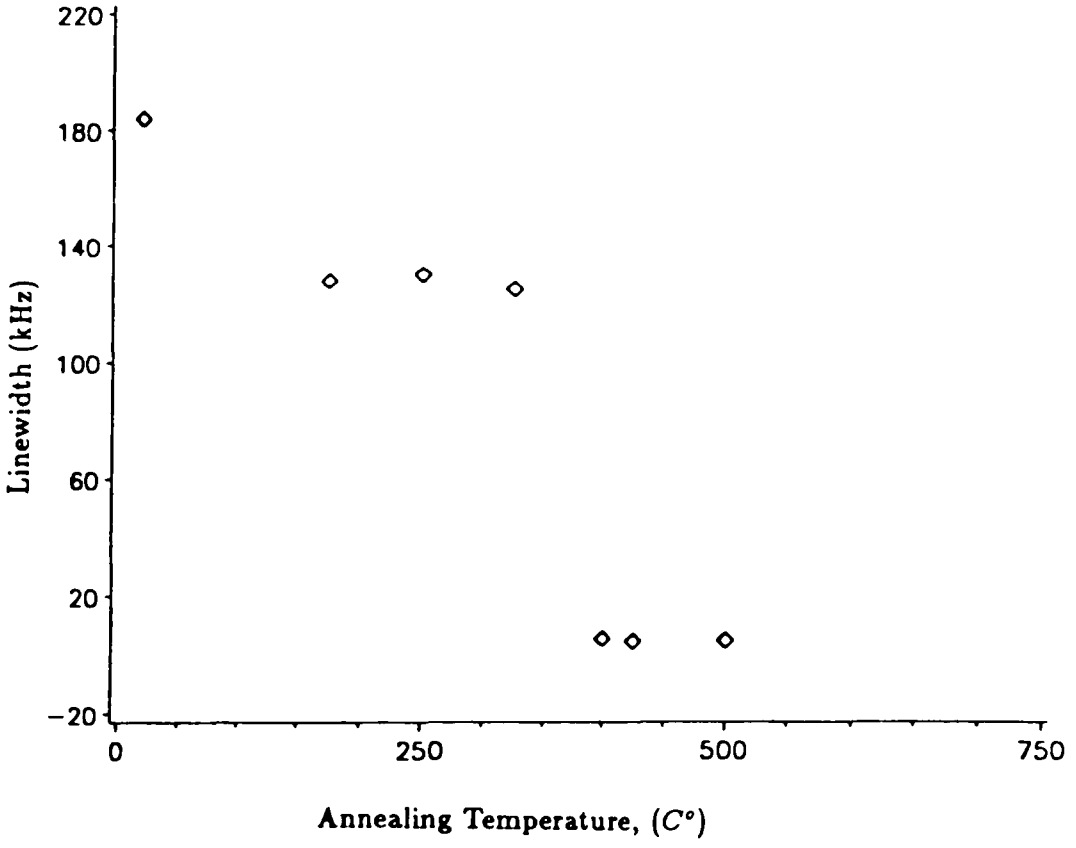

Figure 8.4: ^{71}Ga NMR FWHM in $\alpha - GaAs:H$ prepared on alkli-halide substrate as function of annealing temperature.

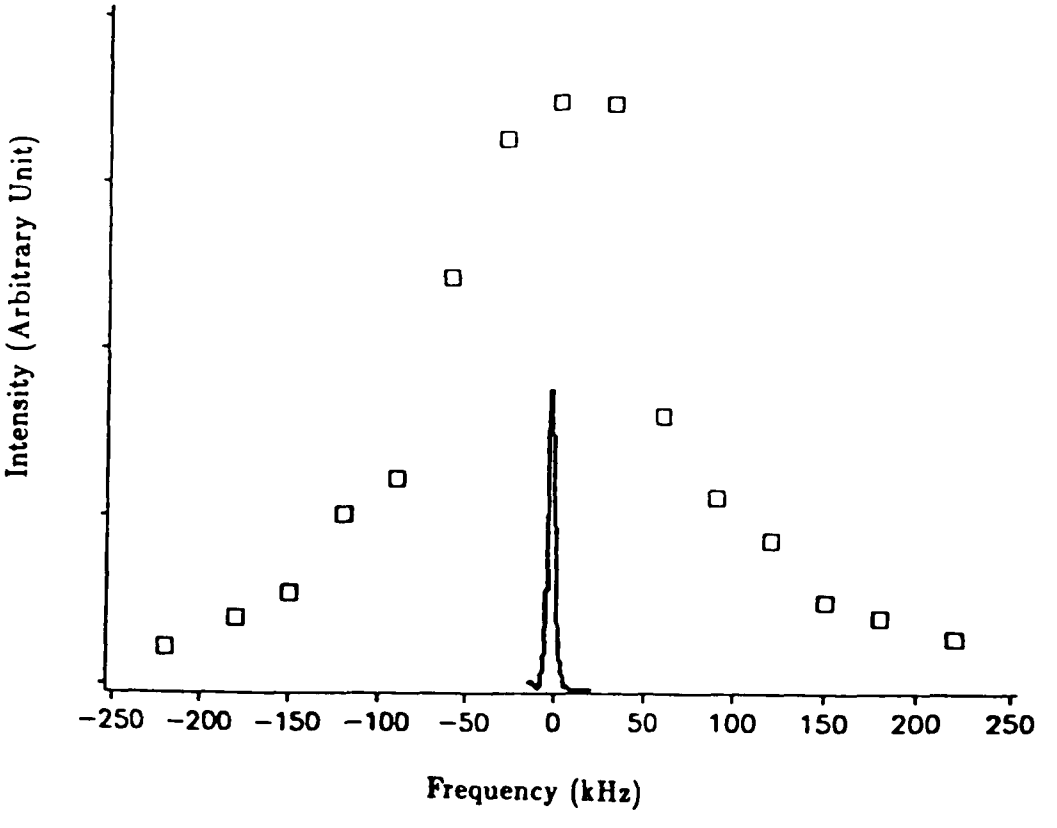

Figure 8.5: Lineshapes of ^{71}Ga in $\alpha - GaAs$ at annealing temperatures 375° C and 400° C. The narrow line is after 400° C annealing which indicates sample crystallization is completed.

All of the above mentioned results, the different linewidth at room temperature before annealing and the different annealing behavior for samples prepared at different substrates, suggest that the sample microstructure is directly influenced by the preparation techniques and conditions.

Two methods have been employed to obtain the lineshapes: Fourier transforming time domain spin-echo signal and point-by-point echo intensity versus transmitter off resonance frequency. The second method could introduce an artificial line broadening. The pulse width used was $t_P = 24\ \mu s$, which is corresponding to $\Delta\nu = \frac{2}{3}\frac{1}{t_P} = 27.8\ kHz$ in frequency domain and the points are taken at about every 20 kHz. The resulting measured linewidth is about 180 kHz. Thus, about 28 kHz artificial broadening could be introduced to the linewidth. To exclude this problem, comparison between linewidthes are made by using the same method, while the tendency of line narrowing due to annealing should be the same by either method.

References

[1] C. Cohen-Tannondji, *Cargese Lectures in Physics*, Gordon and Breach, New York, 1967.

[2] C. Cohen-Tannondji and S. Haroche, J. Phys. (France) **30**, 125, 1969.

[3] C. Cohen-Tannondji and S. Haroche, J. Phys. (France) **30**, 153, 1969.

[4] S. Haroche, Ann de Phys. (France) **6**, 189, 1971.

[5] J. Brossel, B. Cagnac, and A. Kastler, J. Phys. Rad. **15**, 6, 1954.

[6] J. M. Winter, Comptes Rendus **241**, 375, 1955.

[7] J. M. Winter, Ann. de Phys. **4**, 745, 1959.

[8] J. Margerie et. J. Brossel, Comptes Rendus **241**, 373, 1955.

[9] C. Cohen-Tannondji et. S. Haroche, Comptes Rendus **261**, 5400, 1965.

[10] C. J. Favre et. E. Geneux, Phys. Lett. **8**, No. 3, 190, 1964.

[11] E. B. Aleksandrov, O. B. Constantinov, B. I. Pereli et. B. A. Khodovoy, J. Exp. Theor. Phys. USSR **45**, 503, 1963.

[12] N. Polonsky, C. Cohen-Tannondji, Comptes Rendus **260**, 5231, 1965.

[13] S. H. Autler et. C. H. Townes, Phys. Rev. **100**, 703, 1955.

[14] W. Hanle, Z. Physik **30**, 93, 1924.

[15] C. Cohen-Tannoudji, S. Haroche,, Comptes Rendus **262**, 268, 1966.

[16] D. T. Pegg and G. W. Series, J. Phys. **B3**, L33, 1970.

[17] T. Yabuzaki, N. Tsukada, and T. Ogawa, J. Phys. Soc. Japan **32**, 1069, 1972.

[18] N. Tsukada, T. Koyama, and T. Ogawa, Phys. Lett. **40a**, 501, 1973.

[19] T. Yabuzaki, S. Nakayama, Y. murakami, and T. Ogawa, Phys. Rev. **A10**, 1955, 1974.

[20] M. L. Dourneuf, C. Cohen-Tannoudji, J. Dupont-Roc, and S. Haroche, C. R. Acad. Sci. **272**, 1048, 1971.

[21] S. Haroche, C. Cohen-Tannoudji, C. Audoin, and J. P. Schermann, Phys. Rev. Lett. **24**, 861, 1970.

[22] S. Haroche and C. Cohen-Tannoudji, Phys. Rev. Lett. **24**, 974, 1970.

[23] T. Yabuzaki, N. Tsukada, and T. Ogawa, Jpn. J. Appl. Phys. **11**, 1071, 1972.

[24] Y. Takagi, T. Ito, and T. Hashi, J. Phys. Soc. Jpn. **35**, 938, 1973.

[25] M. Kunitomo and T. Hashi, Phys. Lett. **40A**, 75, 1972.

[26] M. Kunitomo and T. Hashi, Phys. Lett. **41A**, 231, 1972.

[27] M. Kunitomo, H. Hatanaka, and T. Hashi, Phys. Lett. **49A**, 135, 1974.

[28] T. Ito and T. Hashi, J. Phys. Soc. Jpn. **44**, 1037, 1978.

[29] T. Ito and T. Hashi, J. Mol. Struct. **58**, 389, 1980.

[30] T. Ito and T. Hashi, Phys. Lett. **88A**, 29, 1982.

[31] T. Ito, J. Phys. Soc. Jpn. **51**, 3623, 1982.

[32] A. Abragam, *Principles of Nuclear Magnetism*, Oxford University Press, New York, 1961.

[33] C. P. Slichter, *Principles of Magnetic Resonance*, Second Revised and Expanded Edition, Springer-Verlag, New York, 1980.

[34] E. Fukushima and S. B. W. Roeder, *Experimental Pulse NMR, A Nuts and Bolts Approach*, Addison-Wesley Publishing Company, London, 1981.

[35] H. Y. Carr and E. M. Purcell, Phys. Rev. **94**, 630, 1954.

[36] F. A. Bovey, *Nuclear Magnetic Resonance Spectroscopy*, 2nd Ed., Academic Press, Inc., New York, 1988.

[37] M. H. Cohen and F. Reif, Solid State Phys. **5**, 322, 1957.

[38] T. P. Das and E. L. Hahn, *Nuclear Quadrupole Resonance Spectroscopy*, Academic Press, New York·London, 1958.

[39] E. I. Fedin and A. I. Kitaigorodskii, Soviet Phys. Cryst. (English Translation) **6**, 322, 1961.

[40] F. Reif, Phys. Rev. **131**, No. 6, 2766, 1963.

[41] N. Bloembergen, Rept. Conf., on Defects in Crystalline Solids, Bristol, 1954, p. 1. The Physical Society, Londen, 1955.

[42] R. J. Glauber, Phys. Rev. **100**, 1597, 1955.

[43] G. Breit, Rev. Mod. Phys. **5**, 91, 1933.

[44] I. I. Rabi, Phys. Rev. **51**, 652, 1937.

[45] N. Polonsky et C. Cohen-Tannondji, J. Physique **26**, 409, 1965.

[46] G. N. Watson, *A Treatise on the Theory of Bessel Functions*, Second Edition, P477-522, Cambridge at Univ. Press, New York, 1962.

[47] R. Zurmühl, *Numerical Analysis for Engineers and Physicists*, translated by R. Subramanian, Spring-Verlag, Berlin and Heidelberg, New York, 1976.

[48] F. D. Colegrove, P. A. Franken, R. R. Lewis, and R. H. Sandsn, Phys. Rev. Lett. **3**, 420, 1959.

[49] T. G. Eak, L. L. Foldy, and H. Wieder, Phys. Rev. Lett. **10**, 239, 1963.

[50] R. A. Marino and J. M. Klainer, J. Chem. Phys. **67**, 3388, 1977.

[51] T. Hirschfeld, S. M. Klainer, and R. A. Marino, *Fourier Transform NQR, in: Fourier, Hadamard, and Hilbert Transform in Chemistry* (A. G. Mashal, ed.), Plenum Press, New York, 1982.

[52] R. S. Cantor and J. S. Waugh, J. Chem. Phys. **73**, 1054, 1980.

[53] D. Ya. Osokin, Phys. Stat. Sol. (b) **102**, 681, 1980.

[54] M. Matti Maricq, Phys. Rev. **B 67**, 4501, 1986.

[55] G. W. Leppelmeier and E. L. Hahn, Phys. Rev. **141**, 724, 1966.

[56] C. D. Hodgman, *Handbook of Chemistry and Physics*, 44th Edition, Chemical Rubber Company, Cleveland, 1962.

[57] A. Colligiani and R. Ambrosetti, J. Chem. Phys. **60**, 1871, 1974.

[58] R. A. Marino, J. Chem. Phys. **57**, 4560, 1972.

[59] P. Galbiati, *The Problem of NQR Linewidth, Applications to Hexamethylenetetramine Crystals*, Tesidi Laura in Fisica, Univ. Degli Studidi Pisa, July 1974.

[60] S. Kojima and K. Tsukada, J. Phys. Soc. Japan **10**, 591, 1955.

[61] G. D. Watkins and R. M. Walker, Bull. Am. Phys. Soc. [2] **1**, 11, 1956.

[62] S. Alexander and A. Tzalmona, Phys. Rev. **138**, A845, 1965.

[63] A. Zussman and S. Alexander, J. Chem. Phys. **48**, 3534, 1968.

[64] C. O'Konski and R. Flautte, J. Chem. Phys. **14**, 815, 1957.

[65] P. J. Haigh and L. Guibé, C. R. Acad. Sci. Paris **261**, 2328, 1865J.

[66] G. Watkins and R. V. Pound, Phys. Rev. **85**, 1062, 1952.

[67] N. F. Mott and E. A. Davis, *Electronic Processes in Non-Crystalline Materials*, Second Edition, Ch. 7, Oxford University Press, England, 1979.

[68] N. J. Shevchik and W. Paul, J. Non-Crystalline Solids **13**, 1, 1973/74.

[69] S. G. Greenbaum, D. J. Treacy, B. V. Shanabrook, J. Comas, and S. G. Bishop, J. Non-Crystalline Solids **66**, 133, 1984.

[70] S. G Greenbaum, R. A. Marino, K. J. Adamic, and C. Case, J. Non-Crystalline Solids **77 & 78**, 1285, 1985.

[71] C. Paparoditis, A. Rideau, G. Monnom, and Ph. Gaucherel, *Optical Properties of Polycrstalline Thin Firms of GaAs Obtained by MBD*, in CNRS International Conference on *Polycrystalline Semiconductors*, Perpignan, 2-4, September, 1982.

[72] D. K. Paul, J. Blake, S. Oguz, and W. Paul, J. Non-Crystalline Solids **35 & 36**, 501, 1980.

[73] M. Hargreaves, M. J. Thompson, and D. Turner, J. Non-Crystalline Solids **35 & 36**, 403, 1980.

[74] R. K. Sundfors, Phys. Rev. **185**, 458, 1969.

[75] R. K. Hester, A. Sher, J. F. Soest, and G. Wersz, Phys. Rev. **B10**, 4262, 1974.

[76] D. Gill and N. Bloembergen, Phys. Rev. **B10**, 4262, 1974.

[77] A. DeVille, J. Phys. Cond., **1**, 9369, 1989.

[78] P. D. Persans, A. F. Ruppert, S. S. Chen, and G. D. Cody, Solid State Communications, **51**, No. 4, 203, 1984.

[79] Susanne M. Lee, Scott J. Jones, Yuan-Min Li, Warren A. Turner, and William Paul, Philosophical Magazine B, **60**, No. 4, 547, 1989.